

High Angular Resolution Imaging of Sun

A thesis
submitted for the degree of
DOCTOR OF PHILOSOPHY

In
The Faculty of Science
Bangalore University
Bangalore

By
V.KRISHNAKUMAR



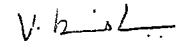
Indian Institute of Astrophysics
Bangalore - 560034
India

August 1998

*To mother nature for her beauty and secrecy
which keeps us busy in life*

Declaration

I hereby declare that this thesis is the result of the investigations carried out by me at the Indian Institute of Astrophysics, Bangalore under the supervision of Prof. P. Venkatakrisnan and Prof. R. Cowsik. This thesis has not been submitted for the award of any degree, diploma, associateship, fellowship, etc. of any university or institute.



V. Krishnakumar
(Candidate)

Bangalore 560034
1998

Certificate

This is to certify that the thesis entitled 'High Angular Resolution Imaging of Sun' submitted to the Bangalore University by Mr. V. Krishnakumar for the award of the degree of Doctor of Philosophy in the faculty of Science, is based on the results of the investigations carried out by him under our supervision and guidance, at the Indian Institute of Astrophysics. This thesis has not been submitted for the award of any degree, diploma, associateship, fellowship, etc. of any university or institute.



Prof. P. Venkatakrishnan
(Supervisor)



Prof. R. Cowsik
(Supervisor)

Bangalore 560034
1998

Acknowledgements

I thank my supervisors Prof. P.Venkatakrishnan and Prof. R. Cowsik for suggesting me this topic and for their help throughout my thesis. I thank my supervisors for the encouragement and useful discussions I have had with them.

I would like to thank the chairman of Physics department, Bangalore University, Prof. Radhakrishna and the faculty and staff of the Bangalore University for their help during registration and thereafter.

I thank Late Prof.S.K.Jain and Late Dr. R. S. Narayanan for all their help. I thank Prof. Ram Sagar for all his help during the course work days and thereafter. I would like to thank the Board of Graduate Studies for recommending my trip to USA to attend the conference. I would like to thank Dr. Aad Van Ballegooijen, Prof. Peter Nisenson and Prof. R. W. Noyes for supporting my stay at Center for Astrophysics, Cambridge. I thank Prof.C.R.Subramanya of GMRT, TIFR for his valuable suggestions.

I thank Prof. Jagdev singh, Prof.C. Sivaram, Prof. Rajmohan, Dr. Satyanarayanan, Dr. Pati for the discussions I have had with them, Dr. Vasundhara and Mr. Pavan, for the image of comet, Mr. Sagayanathan and Mr. Selvaraj mechanical workshop, Mr. Mahesh and Mr.D. Subramanian in the mechanical engineering section, Dr. S. S. Gupta, Dr. Sundaraman, Mr. Aleem, Mr. P. Devendran, Mr. Hari, Mr. Kumaravel and all the staff at Kodaikanal Observatory, I thank all the staff at the Kavalur observatory, Dr.A.K.Saxena Mr.J.P.Lancelot, Mr.J.P.Samson and Mr. Ismail in the Optics division, Mr.A.V.Ananth, Mr.J.S.Nathan, Mr.Narayan Kutty in the IIA computer center, Mr. K.T. Rajan, Ms. Pramila, Mr. Ramesh and Mr. Khan in the director's office, Mr. Rajasekaran in the dean's office, the library staff Dr. A.Vagiswari, Ms. Christina Louis, Mr. Venkatesh, Mr. Yerrappa and the trainees in the library Ms.Ramadevi and Mr.Ashok for their help and cooperation, I thank Mr. Prabhakara, Mr. Pranesh and all the others in the IGC office, Mr. Mohankumar, Mr. Nagaraj, Ms. Malini Rajan in the administrative section, Mr. Kanakaraj, Mr. Bose and Mr. Thyagarajan in the binding section, the IIA volleyball team, Sankar and Ms. Jain in the telephone exchange, Murali for all his help in the computer center, the IIA security and all the canteen staff.

Dilip, Srik, Geetha, Raji, Sankar, Antony, Preeti, Geetanjali, Rajguru, Suresh, Charu, Nirmalya - thanks to all of you for boosting up my spirit during those occasional gray moments. Moz, Joy and Sivarani - right from those days inside the Washburn gate until

now it has been great to have you as my friends, a special note of thanks to Moz for the great help during my final stages. I thank Janani for being such a great friend. I would like to thank Pratap, Murthy, Balu, Meenakshi, Partha, Venkat and Ramabadran at IISc.

I thank Ramesh and Ebe who has helped me throughout my stay here. I thank Arun, Pandey, Sridhar, Swara, Nayak, Sonjoy, Ravindra, Manoj, Jana, Pavan, Mangala, Ramachandra, Manoj Samal and Panda. I would like to thank Partho Joarder for the inspiring discussions. I thank all my seniors especially Annapurni, Reddy, Prabhu, Sengupta and Gangadhara.

Prof. Venkats home was a home away from home. The excellent dinners and the coffee is something which would be in my taste buds for years to come. I thank Mrs. Venkatakrisnan and Prof. Venkat's mother for all their hospitality and kindness.

I am grateful to all my teachers inside the Washburn gate at The American college, Madurai who gave me all encouragement and motivated me to do research. My special thanks are due to Prof. R. P. Reisz, Prof. J. Sethuraman, Prof. V. Srinivasan, Dr.K. Gnanasekar and all the faculty of The American College.

My father, mother, Ravi and Subha for all the support and providing me with an atmosphere most conducive for research. Thank you for helping me in all aspects which has helped in shaping my career. My thanks are due to all my uncles especially those who took keen interest in my research career. I am indebted to my grandfather who was always proud of me. I owe it all to you.

It would be undermining the concern and care of Nalini and Veena to express my thanks formally. I thank my friends Adhi, Simpson and Rajasekar for always encouraging me to do research. I would like to thank Sudha, Kamal and Shivapriya for all their help and for making my visit to US a memorable experience.

I am sure I have missed out quite a number of people. Please pardon me if I have left you out. I thank you all for making my stay at IIA a wonderful experience.

List of symbols:
Chapter 2 & Chapter 3

$o(x,y)$	True object intensity distribution
$o_g(x,y)$	Guess $o(x,y)$
$O(u,v)$	Fourier transform of $o(x,y)$
$O_g(u,v)$	Fourier transform of $o_g(x,y)$
$h(x,y)$	Intensity point spread function
$h_g(x,y)$	Guess $h(x,y)$
$H(u,v)$	Fourier transform of $h(x,y)$
$H_g(u,v)$	Fourier transform of $h_g(x,y)$
$i(x,y)$	Degraded image intensity distribution
$I(u,v)$	Fourier transform of $i(x,y)$
$i_g(x,y)$	Guess estimate of $i(x,y)$
r_o	Fried's parameter
r_t	True Fried's parameter
r_g	Guess Fried's parameter
α	Power index
x,y	Coordinates in physical space
u,v	Spatial frequency vectors
λ	Wavelength of observation
N	Number of negative pixels
$\langle \rangle$	Time averaging operation
$\frac{S}{N}$	Signal to noise ratio
OTF	Optical transfer function

Chapter 4

MTF	Modulation Transfer Function
f	$\sqrt{u^2 + v^2}$
$i_o(x, y)$	Blurred image
$i(x, y)$	Blurred noisy image
$i_{bgd}(x, y)$	Intensity of the background radiation
$i_{dark}(x, y)$	Contribution of thermo electrons
$i_{bias}(x, y)$	DC component in a CCD image
$i_p(x, y)$	gaussian distributed read out noise
$\hat{o}(x, y)$	Object estimate
$\hat{O}(u, v)$	Fourier transform of $\hat{o}(x, y)$
$\phi(f)$	Filter function
$\phi_o(f)$	Power spectrum of object intensity distribution
$\phi_n(f)$	Power spectrum of noise in the image
β	Frieden parameter
ϕ_o^l	Low frequency part of object power spectrum
ϕ_n^l	Low frequency part of noise power spectrum
σ_o^L	Width of the low ϕ_o^l
σ_n^L	Width of the low ϕ_n^l
$\rho(f)$	Power spectral density of the psf
L_o	Outer scale of turbulence
ϕ	Phase
D	Diameter of the telescope
f_c^{teles}	Spatial frequency cut off of the telescope
f_c^{atm}	Spatial frequency cut off of the atmosphere

Chapter 5

P	Gas pressure
B	Magnetic field
$p(r)$	point spread function in radial coordiantes
$c(r)$	Coherent transfer function
$C(f)$	Fourier transform of $c(r)$
$\theta(f)$	Phase across the abberated wavefront
$A(f)$	Amplitude of the $C(f)$
$m_k(f)$	Coefficients of the polynomial respresenting wavefront
$z_1(r)$	Observed image
$z_2(r)$	Observed image + Defocussed observed image
I_{4305}	Image observed at 4305\AA
I_{4686}	Continuum image observed with central wavelength at 4686\AA
$v_{x,k,n}$	Velocity of bright points
$C_{x,k,n}$	Autocorrelation of velocity
n,k	time index and frame index

Chapter 6

$s(t)$	Displacement of the bright point
$v(t)$	Velocity
σ	Standard deviation in the estimated velocities and intensities
$v_n(t)$	Normalized velocity profile of a bright point
I_{nb}	Measured intensity of a bright point in I_{4305}
I_{bb}	Measured intensity of a bright point in I_{4686}
$I_n(t)$	Normalized intensity of a bright point as a function of time

The material presented in this thesis are based on the following publications:

1) Krishnakumar, V., Venkatakrishnan, P., " Determination of atmospheric point spread function using a Parameter search " ,1997, *Astron. Astrophys*,126, 177-181.

2) Van Ballegooijen, A.,Nisenson, P.,Noyes, R.W., Stein, R.F., Nordlund, A., Krishnakumar, V., " Dynamics of magnetic flux elements in the solar photosphere " ,1998, *Astrophys.Journal* (in press)

3) Krishnakumar, V., Venkatakrishnan, P., " Transverse motions and wave heating of the solar atmosphere " , 1998, *Sol. Phys* (submitted)

4) Krishnakumar, V., Venkatakrishnan, P. 1998, " High resolution imaging of sun and other extended sources", in *ASP. Conf. Ser. 154, The Tenth Cambridge Workshop on Cool Stars, Stellar Systems, and the Sun*, eds R. A. Donahue & J. A. Bookbinder (SanFrancisco : ASP).

5) Krishnakumar, V., Venkatakrishnan, P., 1998, " Estimation of Fried's parameter and a U filter for restoration of extended sources degraded by atmospheric turbulence ", in *ASP. Conf. Ser, High Resolution Atmospheric Dynamics Workshop*, eds J. A. Bookbinder, Edward F. Deluca & Leon Golub (SanFrancisco : ASP).

SCOPE OF THE THESIS

Introduction

High resolution imaging is necessary for understanding important physical processes in the sun. For example, the problem of the non-radiative heating of the sun's atmosphere can be understood only by studying the small scale dynamics of the lower atmosphere. Most of the magnetic flux in the sun is stored at smaller scales in the form of tiny elements at the boundaries of granules and supergranules. These tiny elements manifest themselves as bright points called the magnetic bright points which are seen in the intergranular regions. To study the dynamics of these highly intense bright points we need high resolution images.

Image degradation

The information we get from astronomical objects is through their radiation in different wavelengths of the electromagnetic spectrum. Here we concern ourselves with radiation in the optical wavelengths. The radiation intercepted by ground based telescopes is degraded largely because of the random phase delays introduced by the earth's atmosphere.

The two problems that impede the achievement of high resolution are the ignorance of the atmospheric point spread function and ignorance of the noise spectrum.

This thesis consists of 2 parts. One is the study of the problems which impede high resolution observations and the second part concerns some new information on solar atmospheric dynamics, made possible by observations at very high resolution.

The long exposure atmospheric point spread function has an important property of being real both in the physical space and in the Fourier space. The long exposure point spread function is characterised by the Fried's parameter r_0 , which characterises the length scale in the atmosphere over which the atmospheric turbulence is stable. We need to estimate the Fried's parameter r_0 . The details seen in the image

obtained using a ground based telescope depends on this length scale r_o . A larger value of r_o implies better image quality.

Associated with any image recording instrument is the inherent noise in the detector. Noise is a random function of position and difficult to model. Most noise handling algorithms focus on reducing the effect of noise. Noise filtering is the generic solution to the problem.

Estimation of Fried's parameter

To get a handle on the Fried's parameter, we developed a technique which we call as the parameter search method. This technique is only to get a handle on the Fried's parameter and not for restoration. The technique makes use of the fact that the image we record is intensity and hence all the elements in the image have to be greater than or equal to 0. Simple inverse filtering is performed in the Fourier domain using psf's generated with various values of r_o and the resulting image is inverse Fourier transformed. In the case of long exposure images simple inverse filtering will not have singularities since the long exposure transfer function does not fall off to zero even at higher spatial frequencies. However division by the optical transfer function (OTF) will result in large values at higher spatial frequencies since the value of the long exposure OTF is small at large frequencies. The resulting image will have negative intensities. The number of negative elements in the image array is counted. Finally, we plot the number of negative values versus the Fried's parameter r_o . The value of r_o for which the number of negative elements in the array is minimum gives the true r_o . This method for finding the r_o was tested on various simulations and also on real images.

Validation of Parameter Search Technique

We validated this method using an independent method for estimating the Fried's parameter and the values of r_o obtained were compared with the r_o obtained using the parameter search method. The image of Globular cluster NGC1904 was used

for this purpose. This is a good image to test the technique since globular cluster is an extended source made of point sources. The value of r_o obtained using the parameter search method and the conventional method of fitting a gaussian intensity profile are in good agreement.

Noise Filtering and Image Enhancement

Once we get an handle on the Fried's parameter we go onto image restoration. Simple inverse filtering will not restore the image in the presence of noise. Spurious features are generated if inverse filtering is performed on these images. To overcome this, filters are designed. One such filter is the Wiener filter.

The Wiener filter is derived based on the minimising the least square error between the original object intensity distribution and the estimated object intensity distribution. To implement this filter we need to estimate the Wiener parameter. It is not possible to get the signal power and noise power independently. Hence the value of Wiener parameter chosen is only an approximate value. This Wiener parameter is taken to be a constant. This is true only in the case of a white noise. The restored images are highly dependent on this parameter. In a realistic case the noise introduced in an image is not white noise but has a typical power spectrum which has higher power at low frequencies than at higher frequencies.

We discuss the various kinds of noise which enter into our observations. We attempt to reduce the noise in the image by assuming a model for the noise. We test this on real images and show that the restorations we obtain are close to the true object intensity distribution.

This filter was tested on simulations and later on real images. The images restored shows high spatial frequency information even in the presence of noise.

Application to Solar Images

Solar images have small features riding on high background. This makes the extraction of information even more difficult. The evolution of the small scale features

generally occur on their dynamical time scales. Conventional speckle techniques require the statistical treatment of a large number of images. The time required to record the required number of images is often greater than the dynamical time scales. Thus, the extraction of information from a well exposed picture seems a better alternative. We discuss another recent technique called the Phase Diverse Speckle Restoration technique. This technique has been extensively applied in the speckle images. Images of very high spatial resolution has been produced using this technique. We address this problem in 2 parts.

The magnetic flux elements are the key to understand many solar features like network, spicules, sunspots etc.,. These features when observed at high resolution show small scale features which have origin in the solar interior. These small scale features determine the global properties of the sun. Interaction between magnetic fields, convection and radiation can be studied by studying the dynamics of the small scale structures on the sun. We discuss the average properties of the bright points on the sun. It has been established that these bright points are tracers of magnetic flux tubes. We follow these magnetic flux tubes using an object tracking technique. It has been found by earlier workers in this field that there are a few bright points which can move exceptionally fast and are capable of generating sufficient mechanical energy to heat the upper atmosphere. Hence we studied the dynamics of few isolated bright points in these high resolution images. We measure the velocity and intensity power spectrum of the isolated bright points and look for relationship between these quantities and its influence in heating of the solar atmosphere.

Contents

1	Introduction	4
2	Determination Of The Atmospheric Point Spread Function By Parameter Search	9
2.1	Introduction	9
2.2	Technique for recovering the point spread function (psf)	10
2.3	Simulations	12
2.3.1	Object Intensity Distribution	12
2.3.2	Search for minima in N - in the absence of noise	12
2.3.3	Parametric search in the presence of noise	13
2.4	Conclusions	16
3	Search for Fried's Parameter in Globular Cluster image	30
3.1	Introduction	30
3.2	Parametric Search Method	30
3.3	Parametric Search on Globular Cluster NGC1904	32
3.4	Discussions and Conclusions	33
4	A Filter for Restoration of Images Degraded by Atmospheric Turbulence	36
4.1	Introduction	36

4.2	Long exposure and short exposure point spread function	37
4.3	Image restoration	38
4.4	Kinds of noise	39
4.5	Filter for image restoration	42
4.6	Object sharpness as a criterion for image restoration	43
4.7	Deconvolution in the presence of noise	44
4.8	Simulation of objects and restoration using different filters:	49
4.9	Application of Filters on real images	52
4.9.1	Images of Globular cluster	52
4.9.2	Comet images	52
4.9.3	Results	53
4.10	Discussions and Conclusion	53
5	Application of High Resolution Imaging : Dynamics of G band	
	Bright Points I	62
5.1	Introduction	62
5.2	Observation of Photospheric Bright Points	65
5.3	Theoretical Modelling of Flux Tubes : A Brief Summary	66
5.4	Observational details	67
5.5	Phase Diverse Speckle Observations	68
5.6	Tracking of Bright Points	70
5.7	Average Velocity of the Bright Points	72
5.8	Motion of Bright Points and Heating of the Solar Atmosphere	73
6	Application of High Resolution Imaging : Dynamics of G band	
	Bright Points - II	75
6.1	Introduction	75

6.2	Methodology	76
6.3	Lifetime of the bright points	77
6.4	The Velocity and Intensity Distributions	78
6.5	Transverse Motions and Bright Point Intensities	80
6.6	Discussion and Conclusion	85
7	Summary & Conclusions	93
	References	96

Chapter 1

Introduction

The sun is the only star which provides data at high spatial and temporal resolution to study the underlying physical mechanism responsible for the activities happening in and on the sun. We now have data on the sun to understand the physics at the core of the sun through techniques like Helioseismology, direct observations in optical wavelengths for studying the photosphere which is the visible surface of the sun, observations in infrared to study the cooler layers in the solar atmosphere, radio observations and observations in X-ray to study the solar corona. In this thesis we will confine ourselves to observations in optical radiations.

Energy mechanisms responsible for the heating of the chromosphere are still not clearly known. Physical models of the solar atmosphere can be made only if we can first identify the major energy mechanisms and explain the process of energy transport from the lower to upper atmospheres. Features in the sun as small as a hundred kilometers in diameter are believed to act as conduits to transport energy from the lower to the upper atmosphere. Observational evidence has started to accumulate in support of this idea. The major limitation imposed on studying these very small features using ground based telescopes is the intervening earth's atmosphere.

Turbulence in the earth's atmosphere degrades the true object intensity distribution of astronomical sources. The thermal gradients in the air produce random phase delays in the wavefront that cause blurring of images. Limitations in image quality

is because of these inhomogeneities in refractive index caused by the random thermal gradients present in the atmosphere. The effect of the atmosphere can be succinctly described by its transfer function. This transfer function reduces the spatial frequency content depending on the exposure time used for recording the images.

In the case of long exposure imaging, the atmospheric transfer function reduces the spatial frequency response at high frequencies. This attenuation at high frequencies is high and at times can reduce the effective resolution to very small values than what one would have obtained if the same object had been imaged in the absence of the atmosphere. Short exposure imaging is found to have more high spatial frequency information. (Roddir 1980, Fried 1966, Goodman 1985). But in principle the transfer function of the atmosphere at long exposure does not go to zero because the functional form of the long exposure atmospheric psf has a finite value even at higher spatial frequencies.

Usually all images which are exposed for several time scales of the atmospheric turbulence are classified as long-exposure images. As a general rule of thumb, the exposure times in excess of a few hundredth of a second are considered as long exposure images. In long-exposure images the high spatial frequency information is attenuated because the recorded image is the source convolved with the time average of the point spread function (psf).

The long exposure atmospheric transfer function is real in the Fourier domain, i.e., its Fourier transform has no imaginary part. Hence the object's Fourier phase is preserved and we need to worry only about the true contrast of the feature during reconstruction.

A straightforward method to measure the atmospheric psf is to measure the size of the intensity profile of an unresolved source close to the object under study. Here we assume that the medium through which the imaging is done behaves in the same way for both the object under study and the point source. If one has to get the true psf then the point source and the object under study should be within an isoplanatic patch.

For the sun, we do not have access to a point source for comparison. Furthermore, for extended sources like the sun, the atmospheric psf will not be the same on all parts of the image. We have a problem in the case of images of extended sources in which each part of the object has been convolved with different psf's. Hence a single psf will not be a correct characterisation of the psf for an extended object.

Another technique (Collados 1987) for solar image reconstruction uses the limb of the moon in the photographs taken during partial solar eclipse. In the absence of earth's atmosphere the moon's limb would be seen as a sharp edge against the bright Sun's surface. When imaged using a ground based telescope, the moon's limb is blurred because of the atmospheric psf. The gradient of the blurred limb profile of the moon gives the psf of the telescope and atmosphere. The psf thus found is used for deconvolving the psf from the entire image. This psf can be used to remove blurring only near the limb of the moon and within the isoplanatic patch which encompasses the moon's limb. Use of this psf for deconvolution elsewhere in the image will not give true reconstruction.

Night time observers can have single stars for deconvolution. To get a reconstruction which is close to the true object intensity distribution, the star used for determining the psf of the atmosphere and the object under study have to be within the same isoplanatic patch. In the case of photometry of extended objects like clusters of stars, algorithms like Daophot are used (Stetson 1987) where nonisoplanaticity effects are not considered.

The conventional method is to make a gaussian fit to these observed profile and the full width at half maximum of the fitted gaussian is used to characterise the psf. This creates spurious features if the true psf is not a gaussian. In fact, there is theoretical and experimental evidence for the non gaussian nature of the atmospheric psf (Roddier 1980).

One of the main motivations of this thesis is to find the exact long exposure atmospheric psf and use this for reconstruction of images of extended objects. In case of stellar imaging we can hope to have a bright field star close to our object of obser-

vation and therefore correct for the object under study by observing the field star. In objects like the sun, one can never have a point source based on which one could correct for the other unknown features. Hence we need to have an independent way of evaluating the atmospheric psf when we image extended sources.

Once we get the Fried's parameter we need to remove the atmospheric transfer function from the degraded image. The biggest challenge in any restoration scheme is suppression of noise and removal of blurring functions, (in our case the atmospheric psf), without losing high spatial frequency information of the object.

Various novel techniques exist for image restoration. Most of these image restoration techniques target restoration of short exposure image.

The long exposure atmospheric transfer function is real in the Fourier domain and in the case of short exposure imaging the atmospheric transfer function is complex (Fried 1966). Hence the object's Fourier phase does not get contaminated by the long exposure atmospheric transfer function. The only source of contamination is the Fourier phase of the noise.

Chapter 2 discusses the technique of parametric search for determining the atmospheric point spread function.

In chapter 3, the parameter search method is used on real images and the Fried's parameter obtained. The Fried's parameter r_0 so obtained is compared to the Fried's parameter obtained using another independent method which requires point sources for r_0 determination.

In chapter 4, we discuss a filter for image restoration. Restoration is performed on simulated images and then on real images. The Wiener parameter in the Wiener filter is estimated assuming a simple model for the noise in the image. A comparison is made between the noise modeled Wiener filter and the standard Wiener filter. The comparison is made in terms of mean square error between the restored image and the filtered images. Some extended sources are restored using the above techniques and results presented.

In chapter 5 and 6 we present the results obtained using high resolution images of

magnetic bright points. To highlight the usefulness of high resolution images we present some results obtained using the data obtained at the Swedish Vacuum Solar Telescope. The data was obtained by a group elsewhere. A new technique called Phase diverse speckle restoration has been applied to the images to produce high resolution images. Small feature like the magnetic element bright point is thought to be one of the efficient ways in which energy is transported from the lower atmosphere to the upper atmosphere. They are difficult to observe because of their size scales. Typically a magnetic element bright point is about 300 km in diameter, which implies an angular size of approximately $0.''4$. For understanding the processes in the solar atmosphere such as field concentration, process of energy transfer from lower to upper atmosphere, mechanisms of energy storage and release, signature of pre flare processes and other such activities, we need to study the dynamics of small scale features.

In chapter 5 we look at the average properties of the magnetic elements and look for periodicities in their motion. The bright points are tracked using an object tracking technique and the velocities of the bright points determined. We then estimate the autocorrelation of the velocities. This gives an average behavior of the bright point irrespective of the location of the bright point. The bright points are found isolated as well as in clusters.

In chapter 6, to track the bright points without any ambiguity we selected bright points which are well isolated and estimated their velocities and relative intensities. We measure the velocities and lifetimes of these magnetic element bright points and try to look for a possible relationship between their dynamics and the chromospheric heating processes. Here, we attempt to highlight the usefulness of high resolution observations and the physics we can extract from these high resolution images.

Nonlinear Deconvolution Algorithms:

Deconvolution Methods:

Increasing availability of computing power has fuelled the interest in iterative algorithms to reconstruct an unknown object distribution $o(x,y)$ blurred by a linear system's point spread function $p(x,y)$. The measured image distribution $i(x,y)$ is then,

$$i(x, y) = o(x, y) * p(x, y) \quad (1)$$

There are linear and non-linear deconvolution methods to obtain the object distribution $o(x,y)$. Linear deconvolution methods are those which are incapable of extrapolating or interpolating those spatial frequencies which were not observed. For example in the case of maps obtained using synthesis imaging the linear deconvolution methods like Weiner filtering and inverse filtering are not capable of obtaining those spatial frequencies which were not observed because of the incomplete sampling of the spatial frequency plane.

We will discuss briefly about few of the most extensively used non-linear deconvolution methods.

Maximum Entropy Method (MEM):^{1,2,3}

Rooted in information theory the MEM seeks to extract as much information as is justified by the data's signal to noise ratio. This has been successfully used in a variety of fields, including radio astronomy, NMR etc., The difficulty in the techniques comes from the sampling of the data which is limited in terms of spatial frequency and is noisy. This makes many images consistent with the measured data, giving the same value of the goodness of fit statistic, chi square. MEM selects one image from this feasible set of images that describe the data quality well.

MEM chooses the image which assumes the least about information we do not have. It does not introduce structure in the image without evidence in the data. Let us illustrate this with an example. Let us consider a random light pulse generator and in front of this is a CCD array. The random generator shoots off pulses randomly onto the pixels in the CCD. The entropy S , of the given image is defined as the natural logarithm of the number of ways the random generator could generate the random light pulses. For identical pixels, the image with maximum entropy is uniform. To incorporate features in the image i.e., to favour some pixels over the other the definition of entropy S is generalised in terms of a default image F .

Now, maximising the entropy S imposes no correlation on the image for which we have no evidence in the available data. This maximally non committal image may not be correct in the sense that we would need more observations to look for additional correlations in the image. In absence of such additional information MEM would choose an image that is minimally structured. Therefore MEM choice is the most conservative image that describes the data at a given value of the chi square. As the data becomes less noisy, the image becomes more structured.

MEM is based on Bayes theorem. To discuss more on this we introduce the concept of conditional probability. If A and B are two events and we want to estimate the probability of A and B occurring simultaneously, then the probability of A occurring when B occurs $P(A,B)$ is the probability $P(A)$ of A occurring multiplied by the conditional probability that B occurs when A occurs ($P(A|B)$).

$$P(A, B) = P(A)P(A|B) \quad (2)$$

If H represents a hypothesis, S is the state of knowledge before the observations are made, x is the set of observations, then the set of observations contribute to the joint probability that the hypothesis H is true for the measured x is as follows,

$$P(H, x|s) = P(H|S) \times P(x|H, S) = P(x|S) \times P(H|x, S) \quad (3)$$

Here $P(H|S)$ represents our prior knowledge of H , based on prior information S . This in case of an image could be that all pixels must be positive since we record intensity and so can form a basis for rejecting a measurement as unreasonable. The prior knowledge conditions the estimate of the probability $P(H,x|S)$, representing the probability that we will observe the set of observations x under the assumptions that our hypothesis H is true. The factor $P(x|H,S)$ is the probability of obtaining the observations x under the assumption that our hypothesis is true and therefore represents the probability of the maximum likelihood solution. However the factor we want to determine from evaluation of the experimental data is $P(H|x,S)$, the probability that the hypothesis is true, given the set of observations and prior information S . Therefore,

$$P(H|x, S) = P(H|S) \frac{P(x|H, S)}{P(x|S)} \quad (4)$$

is the maximum likelihood solution, which is Bayes' theorem. Here we have maximized $P(x|H,S)$ and identified the maximum likelihood solution. In the mathematical statement of Bayes' theorem one can see that there exists an explicit dependence of the answer on the prior dependence. This dependence is a defect in the Bayesian approach but Maximum Entropy method introduces a degree of standardisation into this choice by forming a particular basis for the introduction of prior information.

Introducing apriori the lack of knowledge in the Bayes' theorem is useful in obtaining a solution with minimum bias. For example, let us consider tossing of a coin. A set of observations of coin tosses in which all results in head is highly improbable compared to results in which both heads and tails are probable. This is because there are a number of ways to get equal number of heads and tails in a series of tosses but only one way to get all heads. Therefore a weighting according to the probability would assign a result where the number of events in the two classes mentioned above is nearly equal a higher probability than the one in which we expect all the events to be same. In statistical mechanics, the entropy S is related to a number of microscopic states W that lead to the macroscopic state through the relationship,

$$S = k \ln W \text{ (or) } W = \exp(S/k) \quad (5)$$

where k is the Boltzmann's constant. Shannon (1948) showed that the above formula obtained from thermodynamics could be incorporated in information theory (apart from the constant k). The natural tendency of a thermodynamic system to increase in entropy is thus associated with a tendency to move toward disordered states having high multiplicity or stated differently has more microscopic states corresponding to the macroscopic variables. The negative sign expressed in logarithms to base 2, gives the number of binary operations providing the same information. This gives the number of such results existing to specify the result with complete certainty.

CLEAN:4,5,6,7,8

The basic CLEAN algorithm was developed by Hogbom in 1974. It is extensively in radio astronomy and hence we will stick to the notations used in radio astronomy. It was originally designed for point sources, but is found to work well for extended sources given reasonable starting model. If b' is the dirty beam, I' is the dirty map and $*$ denotes convolution,

$$I' = b' * I \quad (6)$$

If I_0 is the initial guess, at the n th iteration, it then searches for the largest value in the residual map,

$$I_n = I' - b' * I_{n-1} \quad (7)$$

A delta function is created at the location of the largest residual flux and is given an amplitude (called 'Loop gain') times the value. An antenna's response to the delta function, the dirty beam is then subtracted from I_{n-1} to yield I_n . The iteration is continued until a specified iteration limit N is reached or until the root mean square residual reduces to a specified level. The position of each delta function is saved. At the point when the component subtraction is stopped it is assumed that the residual brightness distribution

consists mainly of noise. To prevent high spatial frequency features which might be spuriously extrapolated from the measured data, each CLEAN component is convolved with CLEAN beam.

Richardson-Lucy algorithm (RL):^{9,10,11,12}

RL algorithm is based on statistical methods and has a very strong mathematical and physical basis. But the basic requirement is one has to know the psf. RL is used for estimating the object intensity distribution in the presence of photon noise which is inherent in any observation. Let $i'(x)$ is the number of counts that would be measured at x if we were to average a large number of independent observations. The observed data $i(x)$ is distributed with a mean $i'(x)$ with a Poisson distribution, so the probability of getting $i(x)$ counts in a pixel when the mean is $i'(x)$ is,

$$P(i/i') = \frac{e^{-i'} (i')^i}{i!} \quad (8)$$

Likelihood of an entire data set of values is the product of the probabilities of each value and so the log likelihood is written as,

$$\ln L = \int \ln e^{-i'} + \ln (i')^i - \ln i! \quad (9)$$

The goal is to recover the image $o(x)$ from the noisy data $i(x)$ given the equations of image formation and the log likelihood estimate. The maximum likelihood solution maximises $\ln L$.

This technique plays a very important role when we are trying to recover data from a noisy data. This technique works well as long as we are dealing with Poisson distributed noise. In the case of CCD images, noise like read out noise are Gaussian distributed and hence some pixel values turn out to be negative. RL fails in such cases. A simple solution suggested is to add a floor value to the image. But this is reported to bias the results.

As said before, techniques like RL work well when the PSF is known to a great accuracy. Our aim is to look for a method to estimate the PSF. Once the atmospheric PSF is known one can use linear or nonlinear techniques to restore the image. In case of HST images the deconvolutions have been carried out using observed PSF's since theoretically computed PSF's have been found not to match with the observations. The noise in the observed PSF is found to pose problem in recovery of images using RL.

However, a linear method like Wiener filtering is severely limited in capability relative to modern constrained nonlinear methods. Many researchers in the field of

image restoration have pointed out the difficulties in linear deconvolution methods such as the Wiener filter. The primary objections have been that these methods amplify noise and introduce artifacts at high spatial frequencies. The advantages of using a linear restoration scheme is that the relative brightness is preserved and computationally the linear restoration schemes are efficient. However in high fidelity image restoration several kinds of artifacts can be produced by linear restoration schemes¹³. Sometimes the researcher does not have information apriori or the information may not be applicable. Linear methods are best suited in situations where computational speeds are of great importance. Filters like Wiener type filter might be a good choice because it explicitly deals with noise and tries to reach a solution that is in the least sense, optimum. Although nonlinear methods are useful for image restoration especially to retrieve spatial frequencies which were not measured, they are not used in this thesis since we deal with optical images which have spatial frequencies upto the diffraction limit without any gaps in the measurement and our aim is to try and retrieve information upto the diffraction limit of the telescope and not beyond it.

References:

- 1) Cornwell, T.J., and Evans, K.F., 1985, *Astron. Astrophys.* 143, 77-83.
- 2) Narayan, R., and Nityananda, R. 1986, *Ann. Rev. of Astron. Astrophys.* 24, 127.
- 3) Sault, R.J. 1990, *Astron. J.* 354, L61.
- 4) Hogbom, J.A. 1974, *Astron. Astrophys. Suppl. Ser.* 15, 417.
- 5) Schwarz, U.J. 1978, *Astron. Astrophys.* 65, 345.
- 6) Clark, B.G. 1980, *Astron. Astrophys.* 89, 377.
- 7) Cornwell, T.J. 1983, *Astron. Astrophys.* 121, 281.
- 8) Schwab, F.R. 1984, *Astron. Astrophys.* 89, 1076.
- 9) Lucy, L.B., 1992, *Astron. J.*, 104, 1260.
- 10) Krist, J., "Astronomical Data Analysis and Software", (R.A. Shaw, H.E. Haynes and J.J.E. Hayes, eds.,) *ASP. Conf. Ser. Astron. Soc. Pacific.* 77, 349.
- 11) Richardson, W.H. 1972, *J. Opt. Soc. Am.*, 62, 55.
- 12) Bi, H., and Borner, G. 1994, *Astron. Astrophys. Suppl. Ser.* 108, 409.
- 13) Robert J. Hanisch, "Restoration of HST images and spectra", (R.A. White, R.J. Allen eds.,) *Proceedings of a Workshop held at the Space Telescope Science Institute, Baltimore, Maryland.* 1990.

Chapter 2

Determination Of The Atmospheric Point Spread Function By Parameter Search †

2.1 Introduction

The result of blind deconvolution is a reconstructed image that has non positive intensities. The number of these non positive pixels has been used as an estimator for the departure from a perfect reconstruction. Simulations of reconstruction of objects convolved with a kernel having one or two parameters are shown to demonstrate the efficiency of the estimator. We thus present a technique of determining the unknown parameters of the point spread function by searching for the point in parameter space with the lowest number of non positive pixels. It is also shown that the parameters of the convolving kernel can be obtained even in the presence of noise.

In the first section we discuss the technique for obtaining the Fried's parameter. In the second chapter and the subsections we discuss the simulations carried out

† Krishnakumar V., Venkatakrishnan P., *Astron. Astrophys. Suppl. Ser.*126, 177-181 (1997)

to estimate the Fried's parameter. The simulations were carried out both in the presence and absence of noise. The results are discussed.

2.2 Technique for recovering the point spread function (psf)

The true object spectrum is convolved with the point spread function of the medium,

$$\langle i(x, y) \rangle = o(x, y) * \langle h(x, y) \rangle \quad (2.1)$$

where $\langle i(x, y) \rangle$ is the time averaged intensity distribution, $o(x, y)$ is the true object intensity distribution, $h(x, y)$ is the instantaneous atmospheric psf, $\langle h(x, y) \rangle$ is the time averaged psf and " * " denotes convolution. Performing Fourier transform on either side of equation (1), we get

$$\langle I(u, v) \rangle = O(u, v) \langle H(u, v) \rangle \quad (2.2)$$

where $\langle I(u, v) \rangle$, $O(u, v)$, $\langle H(u, v) \rangle$ are the Fourier transforms of $\langle i(x, y) \rangle$, $o(x, y)$, $\langle h(x, y) \rangle$ respectively, and u, v are the spatial frequency vectors. To recover the true object spectrum $o(x, y)$, we perform inverse filtering on the degraded image. Therefore the true object intensity distribution will be

$$O(u, v) = \frac{\langle I(u, v) \rangle}{\langle H(u, v) \rangle} \quad (2.3)$$

Inverse transforming $O(u, v)$ we get $o(x, y)$. In our case $h(x, y)$ is not known. Guess psf is constructed and inverse filtering is done. Let $h_g(x, y)$ be the guess psf. The Fourier transform of the guess psf is $H_g(u, v)$. Using this psf we get,

$$O_g(u, v) = \frac{I(u, v)}{H_g(u, v)}. \quad (2.4)$$

The reconstructed image spectrum $o_g(x, y)$ will be the inverse Fourier transform of $O_g(u, v)$.

The point spread function of the atmosphere which blurs the object intensity distribution is (Tatarski 1961, Fried 1966)

$$H(u, v) = \exp\left[-3.44\left(\frac{\lambda(u^2 + v^2)^{1/2}}{r_o}\right)^\alpha\right] \quad (2.5)$$

where u and v are the spatial frequency vectors, λ is the mean wavelength of observation, r_o is the Fried's parameter (seeing parameter) and α the power index which was derived to have a value of 5/3 in the case of astronomical observations. In practice there could be deviations in the value of α . The behavior of the point spread function in the tail of the profile depends on α , and r_o is a measure of the core of the point spread function profile. In our proposed technique we use the Fried's coherence function in its functional form but both α and r_o are left as free parameters.

The degraded image is deconvolved using a series of point spread functions with different r_o and α . The number of elements N , where the intensity is equal to and less than zero is found in each reconstruction. In this two parameter space we search for the minimum of number of zeros and negative values. The corresponding r_o and α at which the minimum occurs are the true point spread function parameters.

In the presence of noise, equation (1) is written as

$$\langle i(x, y) \rangle = o(x, y) * \langle h(x, y) \rangle + n(x, y) \quad (2.6)$$

where $n(x, y)$ is the noise in the image plane which gets added to the blurred object intensity distribution. Since noise is additive, it is not convolved with the atmospheric psf, but is effectively convolved with a delta function, which in turn, can be considered as a psf with very large Fried's parameter, say r_n , where $r_n \gg r_o$

$$\langle i(x, y) \rangle = o(x, y) * \langle h(x, y) \rangle + n(x, y) * h_n(x, y) \quad (2.7)$$

and $h_n(x, y)$ approaching a delta function. For obtaining the parameters of the psf the above equation is Fourier transformed and inverse filtering is performed.

$$\langle I(u, v) \rangle = O(u, v) \langle H(u, v) \rangle + N(u, v) H_n(u, v) \quad (2.8)$$

Inverse filtering,

$$\frac{\langle I(u, v) \rangle}{H_g(u, v)} = \frac{O(u, v) \langle H(u, v) \rangle}{H_g(u, v)} + \frac{N(u, v) H_n(u, v)}{H_g(u, v)} \quad (2.9)$$

This equation is inverse transformed and the number of non positive pixels are found. Similarly, for other r_o values $H_g(u, v)$ is constructed and the number of non positive

pixels found. Since r_n is always greater than r_o , the number of non positive pixels N contributed by the second term is not expected to go through a minimum. Therefore even in the presence of noise the minima in N is expected to occur when the guess psf parameters matches with the true r_o and α values. Hence r_o and α can be found by looking for the deepest minima in N in the parameter space of α and r_o .

This makes the proposed technique more general and could be used when the functional form of the psf of the intervening medium is of the Fried's coherence function type.

2.3 Simulations

2.3.1 Object Intensity Distribution

Simulations were carried out on single sources as well as on multiple sources. The technique has been tested on objects with intensity distribution with smooth edges as well as on objects with sharp edges. Here we discuss the case of an object with multiple sources and sharp edges.

2.3.2 Search for minima in N - in the absence of noise

The true object consists of two sources with unequal intensities. The object plane has a plate scale of $\approx 0.''6$ per pixel. The angular size of source A and B is $0.''4$ and $0.''5$ respectively. The two sources are separated by a angular distance of around $1''$. Fig (2.1) shows the true object intensity distribution and Fig (2.2) is the atmospheric psf. The convolution of the object intensity distribution with the atmospheric psf yields the degraded image. Fig (2.3) is the convolved image. Fried derived the expression for the coherence function $H(u, v)$ and obtained a value of $5/3$ for α . No departures are seen in the value of $\alpha = 5/3$ under the conditions of astronomical observations. Assuming α is known, for each value of r_o the degraded image is deconvolved and N is obtained. The plot of N for various r_o is given in Fig (2.4). We see that

when the deconvolving psf's r_o is equal to the true r_o , N is a minimum. However experimental evidence for departures from 5/3 power law has been reported in the case of horizontal propagation near the ground (Bouricius & Clifford 1970; Clifford et al. 1971; Buser 1971).

Therefore, assuming that α is unknown, we do the following. For different values of α , the reconstruction is done for a range of r_o . Fig (2.5) is a plot of N versus α at a given r_o . Here again we see that when the deconvolving psf's α becomes equal to the true psf's α , N goes to a minimum. Now assuming both α and r_o are unknown, N is found at each value of α and r_o . Fig (2.6) is the surface plot of N as a function of r_o and α .

Wrong estimation of one of the parameters, α or r_o leads to inaccurate photometric values and also generates spurious features in the reconstructed image. Fig (2.7) is an example of an image degraded by a psf with $\alpha = 1.67$, but reconstructed using $\alpha = 1.7$, $r_o = 5.0$ cm and Fig (2.8) is reconstruction done with correct value of α but with a $r_o = 5.5$ cm instead of the true $r_o = 5.0$ cm. We can clearly see spurious features in both the reconstructions.

2.3.3 Parametric search in the presence of noise

The above simulations were repeated with different kinds of noise added to the blurred image. Fig (2.9) is the image degraded by the atmospheric psf with $r_o = 5.0$ cm and $\alpha = 1.67$. Noise with uniform distribution is added to the degraded image. The signal to noise ratio in all the noisy images is around 5.0. Fig (2.10) is the plot of the number of non positive pixels N for various values of Fried's parameter r_o in the presence of additive noise and Fig (2.11) is the plot of the number of non positive pixels N in each reconstructed image for different values of α . In both the plots we see that the minima in N occurs at the true α and r_o . Fig (2.12) is the surface plot of N as a function of α and r_o . A search for the minima in N gives the values of r_o and α of the true psf.

Fig (2.13) is the convolved image to which zero mean gaussian white noise has

been added. Fig (2.14) is the plot of the number of non positive pixels N in each reconstructed image for different values of Fried's parameter r_o . Fig (2.15) and Fig (2.16) are the plots of N against r_o for reduced grid size of r_o , 0.5 cm and 0.1 cm respectively. It is seen that the minima in N occurs at a r_o close to the true r_o .

Fig (2.17) is the image intensity distribution with additive Poisson noise. Fig (2.18), Fig (2.19) and Fig (2.20) are the plots of the number of non positive pixels N against the Fried's parameter r_o with grid size in r_o equal to 1.0 cm, 0.5 cm and 0.1 cm respectively. We can see that for a grid size in r_o equal to 1.0 cm the minima in N occurs at 2.0 cm. When the grid size is reduced to 0.5 cm the minima in N shifts to 5.5 cm and the minima in N stays at 5.5 cm when the grid size is reduced to 0.1 cm. Hence in the presence of noise, reduction of grid size helps to identify the parameters r_o and α more accurately. and α . The minima in N occurs at the true r_o and α .

A way to improve the estimation of the Fried's parameter using this method is to smoothen the noisy image before we deconvolve with the Fried's coherence function. This helps in isolating the minima in the plot of number of non positive pixels versus the Fried's parameter.

The search for r_o using the number of non positive pixels N as an estimator is what we have discussed. If we look at the plot of the N versus r_o the intriguing fact is the local minimas and maximas seen on either side of the dip at true r_o . We find that when the signal to noise level is around 20 or more then the minima is unique and the variations in the non positive pixels on either side of the true minima is low. As the signal to noise deteriorates this minima slowly gets merged with the variations alongside. Hence this method can be used quite comfortably in those images which have a reasonably high signal to noise ratio.

At low signal to noise ratios, ie., $\frac{S}{N} < 100$ the value of r_o at which the minima in the plot of non positive pixels occur is not deep. This might lead to erroneous estimation of the Fried's parameter. To improve on the estimation of Fried's parameter at these low signal to noise ratios we do the following. The blurred noisy signal is convolved with a smoothening function. In this case we smoothen the degraded image with a

gaussian. The width of the gaussian is chosen in such a way that it suppresses the noise and not the object information.

Fig (2.21) is obtained without smoothening the noisy image. The signal to noise ratio in this image is 30. Fig (2.22) is obtained by smoothening the blurred noisy object with a gaussian of width 0.6. We see that the depth of the minima has increased. The width of the gaussian has to be higher than the value of Fried's parameter. This is to ensure that the information of the object is maximally retained and noise at high frequency is filtered. Fig (2.23) is obtained by smoothening the blurred noisy object with a gaussian of width 0.7.

To prove that the estimation of the Fried's parameter is independent of the grid size we estimate the number of non positive pixels for r_o at various grid sizes and plot N versus r_o . Fig (2.24) is the plot of non positive pixels versus the Fried's parameter for a grid size in r_o equal to 0.01. Fig (2.22) and Fig (2.23) were obtained with a grid size equal to 0.005 smoothened with gaussian of different widths. We see that the change in grid size does not alter the value of r_o at which the minima in non positive pixels occur. The asymmetry in the plot of N versus r_o is because of the following reason. Let r_g be the guess Fried's parameter and r_t the true Fried's parameter. The ratio of the true psf to the guess psf is,

$$\frac{H_t(f)}{H_g(f)} = \exp\left[-3.44(\lambda f)^{5/3}\left(\frac{1}{(r_t)^{5/3}} - \frac{1}{(r_g)^{5/3}}\right)\right] \quad (2.10)$$

when r_g is $< r_t$ the exponent is positive and hence enhances the higher spatial frequencies and attenuates the lower spatial frequencies. This leads to generation of negative values in the physical space. When r_g is $> r_t$ then the higher frequencies are attenuated and lower frequencies enhanced. This leads to generation of lesser number of negative values compared to the earlier case. However, any deconvolution performed on these images will not give the correct reconstruction unless the noise is filtered.

2.4 Conclusions

The technique we have proposed in this chapter is very general and is applicable for images of arbitrary shape. It can also provide a decent reconstruction for features that are several hundred times more intense than noise. However, the problem of image reconstruction remains for restoration of low contrast features in the presence of noise. We believe that the knowledge of the actual point spread function, as gained by the parametric search described in this chapter, will provide tight constraints on iterative deconvolution schemes for very noisy images which can start with a guess for the noise distribution and converge to the true distribution of noise. This belief is yet to be verified. On the other hand, there are a number of applications where the determination of the psf itself would be of vital importance. One example is the determination of daytime "seeing" at a new astronomical site. All that would be required is a sequence of long exposure pictures of the sun taken through a filter of reasonable bandwidth like 5 nm or 10 nm. Another example is the need to determine the broadening mechanisms of spectral lines. We hope that this technique would be able to detect small departures from a gaussian profile, which has great implications for the detection of non-thermal or supra-thermal distributions. The quality of spectra that are expected from SOHO, for example, would perhaps be good enough for such investigations.

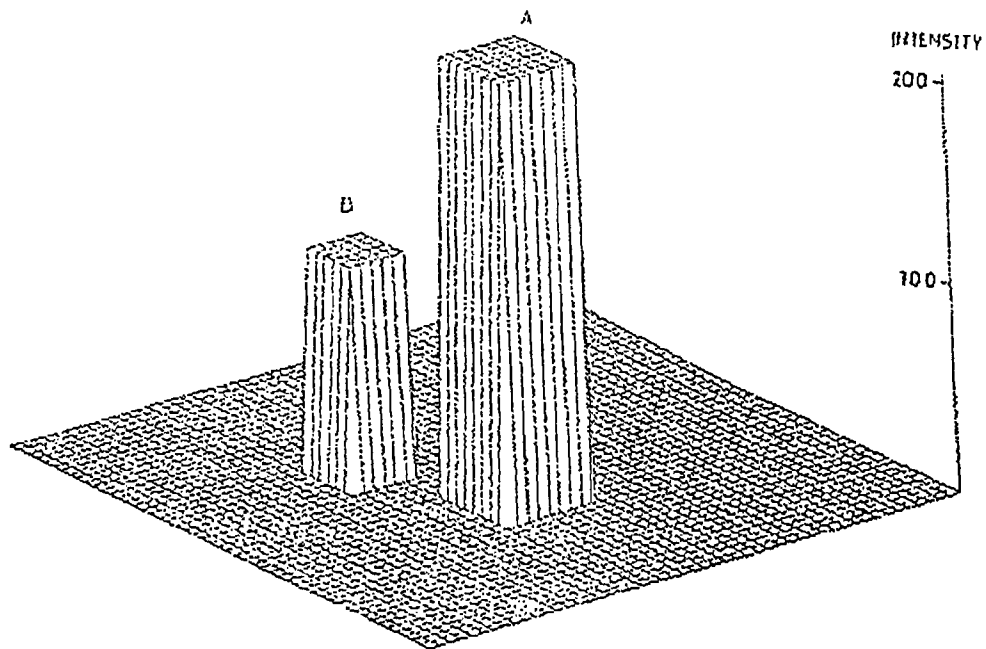


Figure 2.1: True object intensity distribution. Two sources with unequal intensities. Plate scale in the image plane is $\approx 0.06''$ per pixel. Angular separation between the two sources is $\approx 1''$. Angular size of stronger source is $\approx 0.4''$ and the angular size of the weaker source is $\approx 0.3''$.

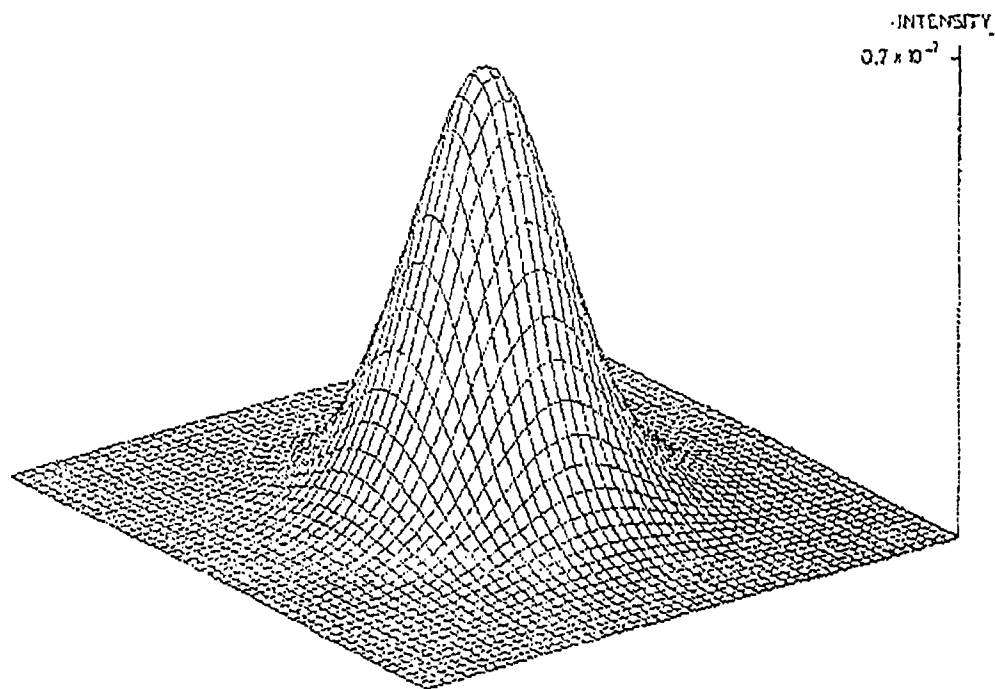


Figure 2.2: The atmospheric point spread function (psf) with $r_o = 5.0\text{cm}$ corresponds to $2.5''$, $\alpha=1.67$.

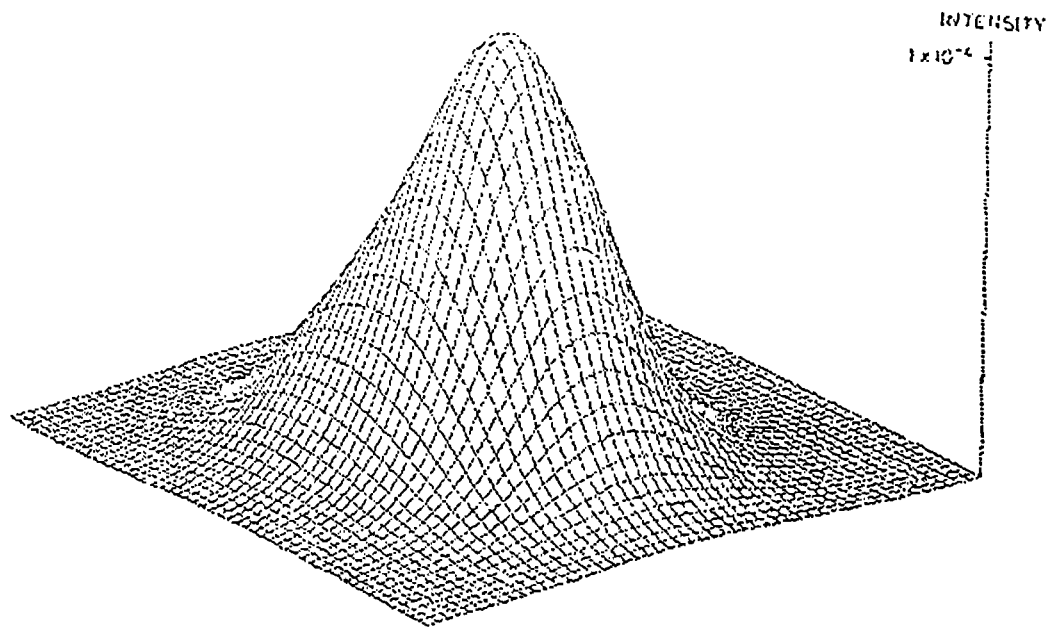


Figure 2.3: The true object intensity distribution (Fig 2.1) convolved with the atmospheric psf (Fig 2.2) and produces this degraded image. Since the atmospheric psf is wider the angular separation between the two sources the blurred image is seen as a broadened single source.

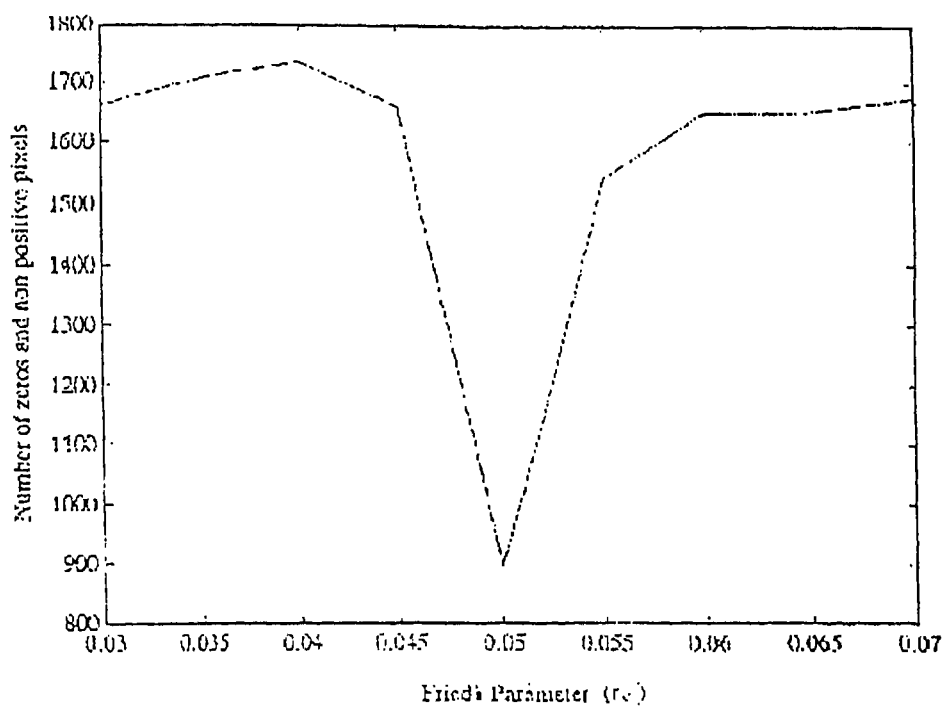


Figure 2.4: Plot of number of non positive pixels N (including zeros in the image plane) with varying Fried's parameter r_0 . α is fixed at 1.67 which is the true α . True r_0 is 5.0cm. Minima in N occurs at $r_0 = 5.0$ cm.

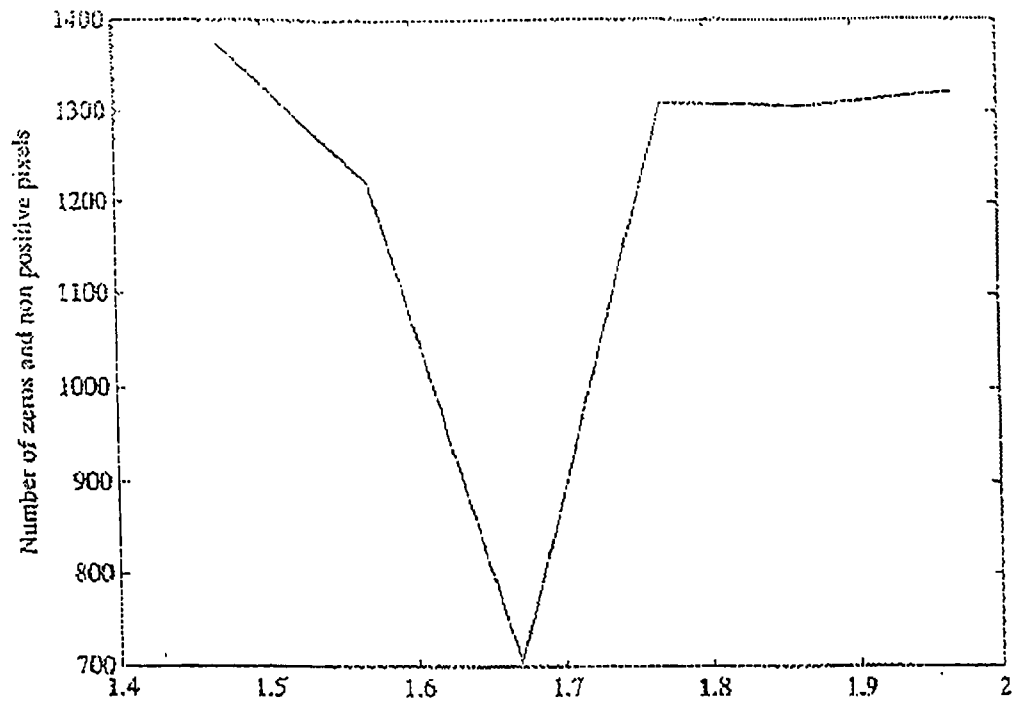


Figure 2.5: Plot of number of non positive pixels N (including zeros in the image plane) for different values of the power index α . The Fried's parameter $r_0 = 5.0\text{cm}$. True $\alpha = 1.67$. Minima in N at $\alpha = 1.67$.

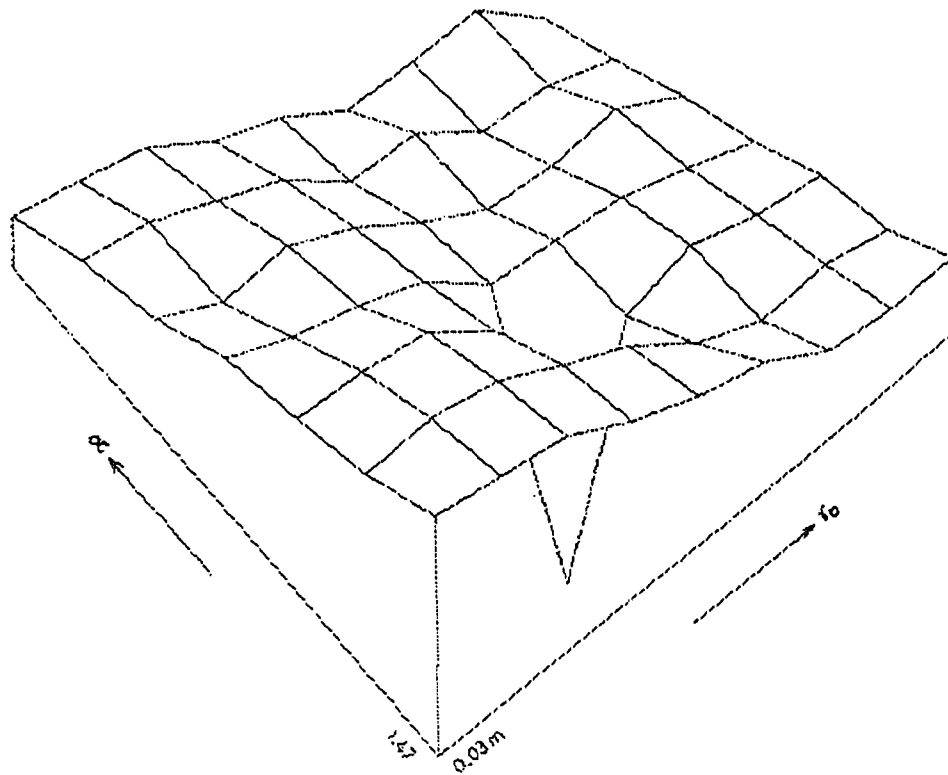


Figure 2.6: Surface plot of N for different values of the power index α and the Fried's parameter r_0 . The α and r_0 corresponding to the minimum of N gives the true α and r_0 values.

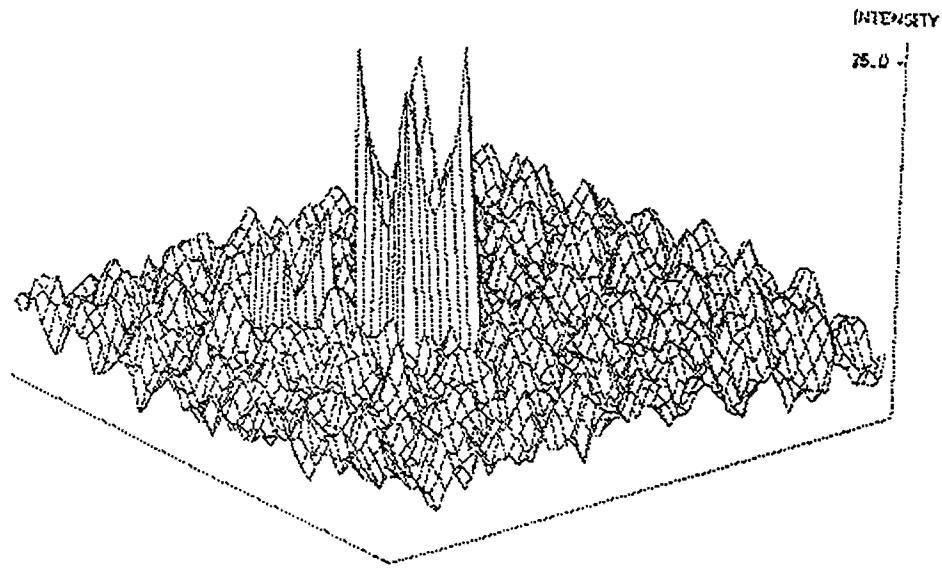


Figure 2.7: Image intensity distribution reconstructed using a Fried parameter r_0 of 5.0cm but instead of $\alpha = 1.67$, $\alpha = 1.7$ has been used. Spurious features can be seen in the reconstruction.

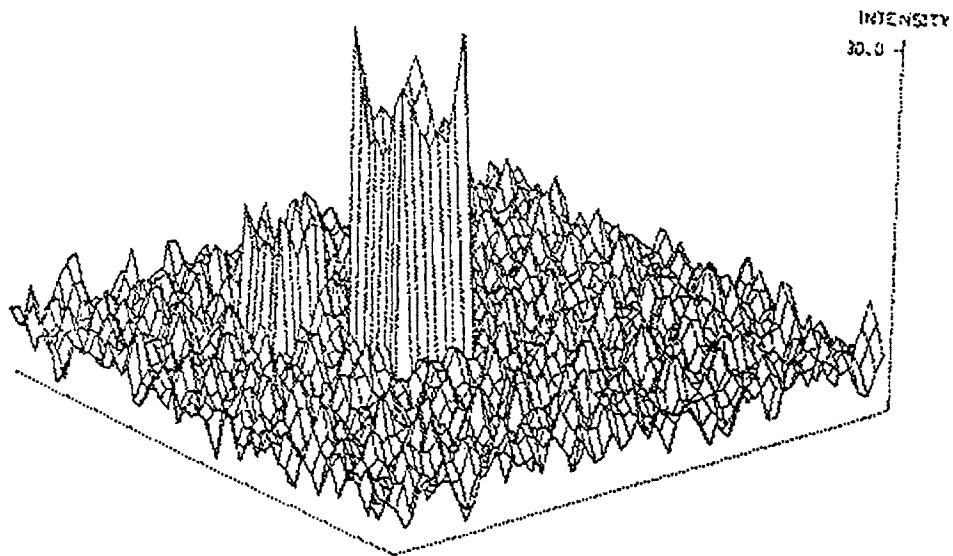


Figure 2.8: Image reconstructed using α of 1.67. The r_0 value used in this reconstruction is $r_0 = 5.5$ cm instead of 5.0cm which is the true r_0 . Spurious features can be seen in the reconstructed image.

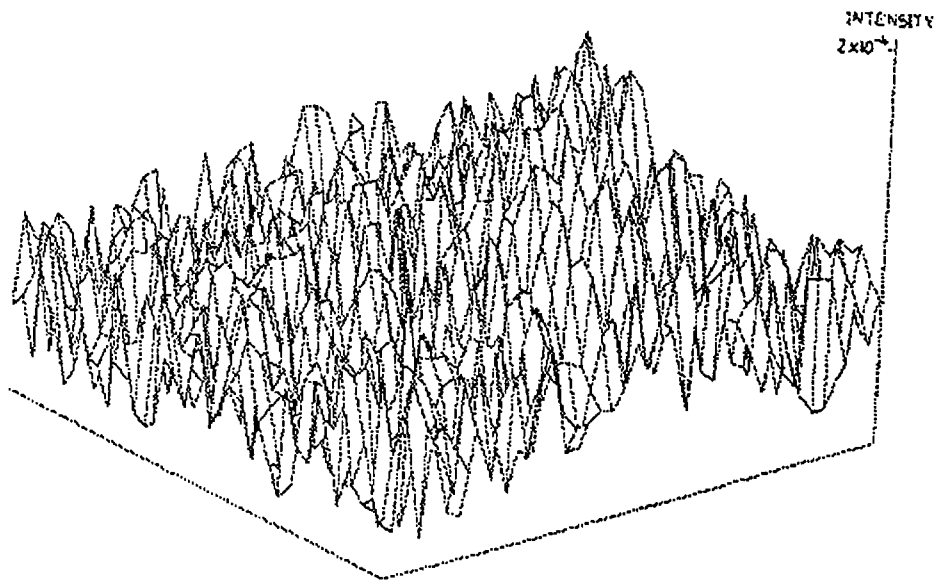


Figure 2.9: Object intensity distribution degraded by the atmospheric psf. An uniform noise is added to the blurred image. The signal to noise in the image is 5.0.

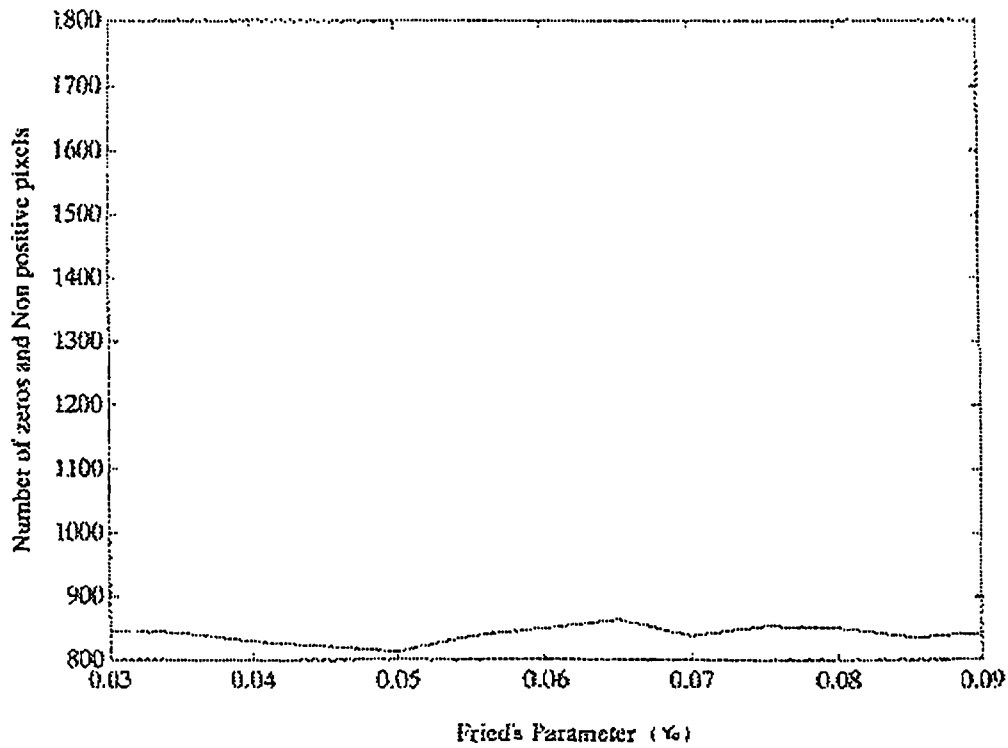


Figure 2.10: Plot of number of non positive pixels N (including zeros in the image plane) in a blurred image with additive uniform distribution noise against varying Fried's parameter r_0 . α is fixed at 1.67 which is the true α . True $r_0 = 5.0\text{cm}$. Minima in N at $r_0 = 5.0\text{cm}$.

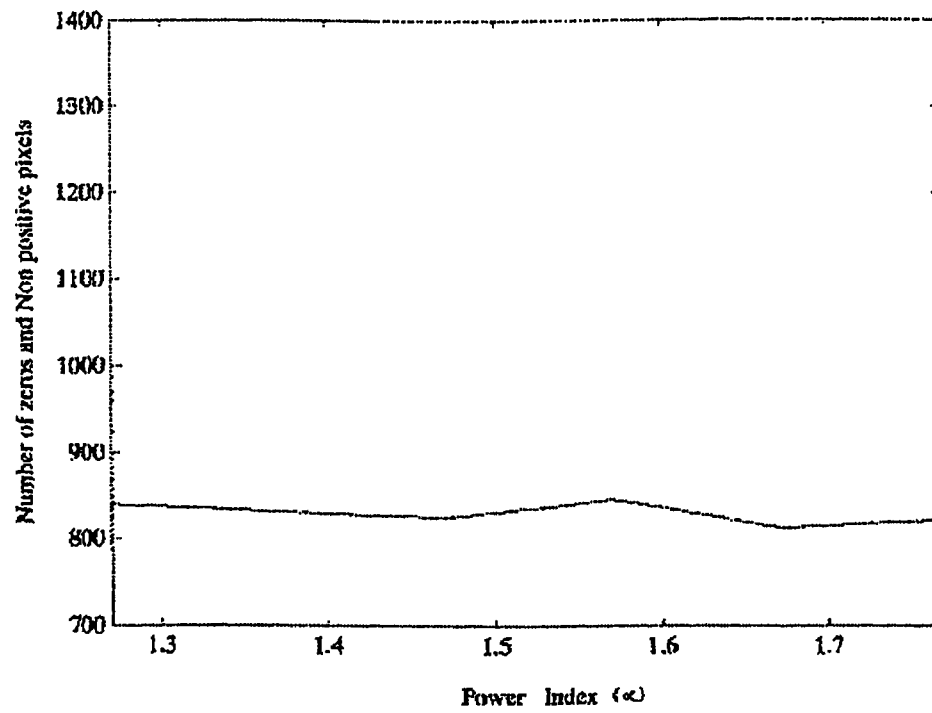


Figure 2.11: Plot of number of non positive pixels N (including zeros in the image plane) for different values of the power index α . The Fried's parameter fixed at 5.0cm which is the true value of r_0 . True $\alpha = 1.67$. Minima in N at $\alpha = 1.67$.

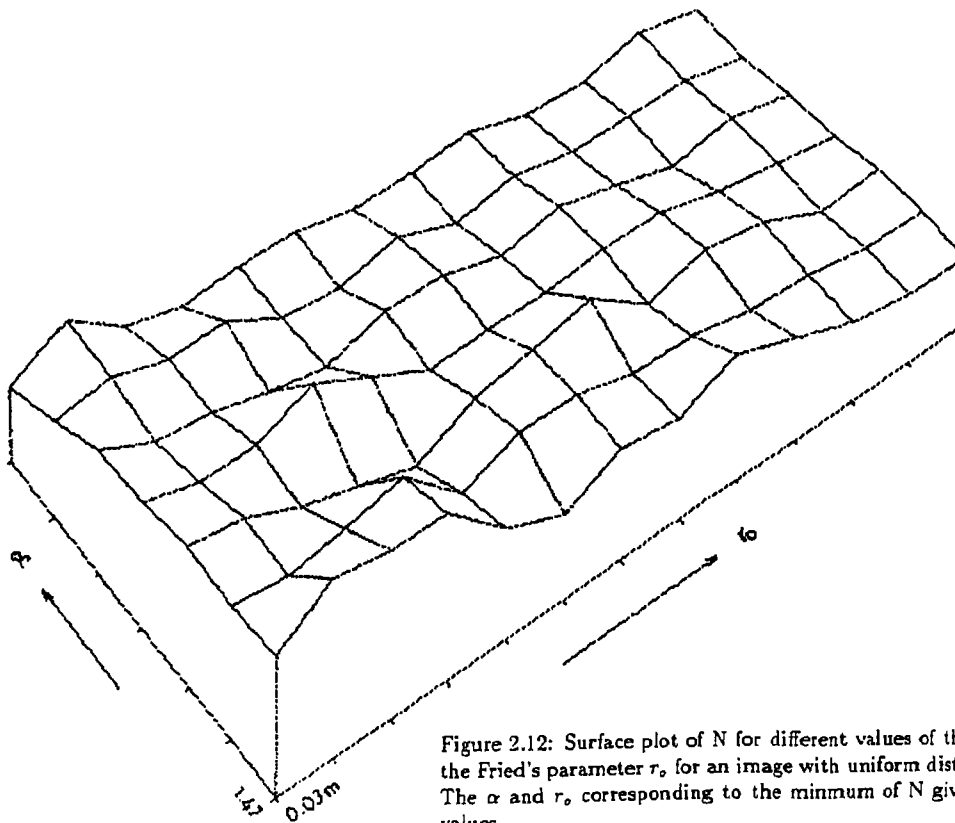


Figure 2.12: Surface plot of N for different values of the power index α and the Fried's parameter r_0 for an image with uniform distribution noise added. The α and r_0 corresponding to the minimum of N gives the true α and r_0 values.

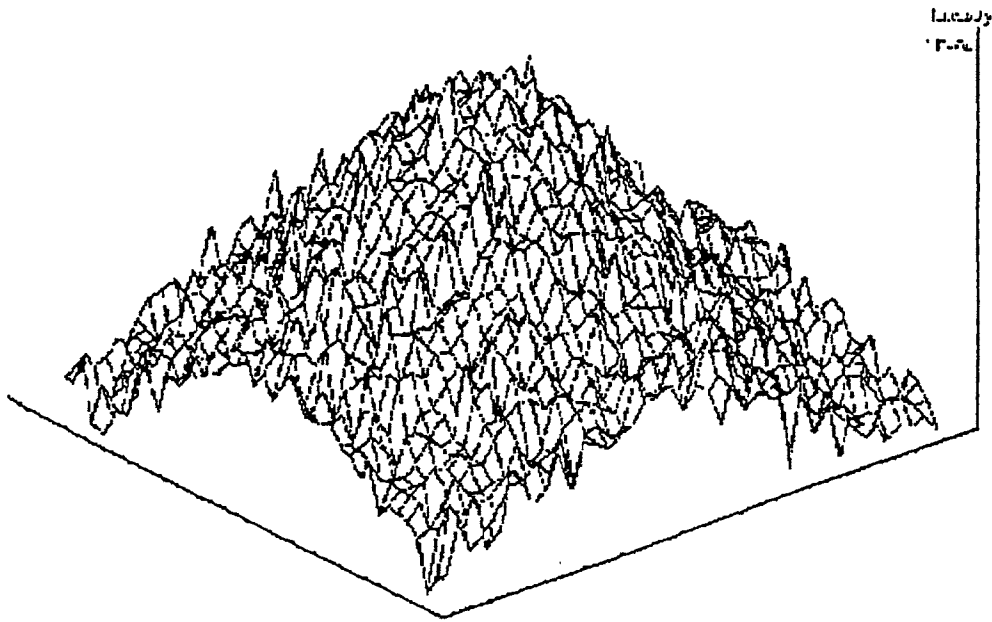


Figure 2.13: Object intensity distribution degraded by the atmospheric psf. Zero mean Gaussian white noise is added to the blurred image. The signal to noise in the image is 5.0.

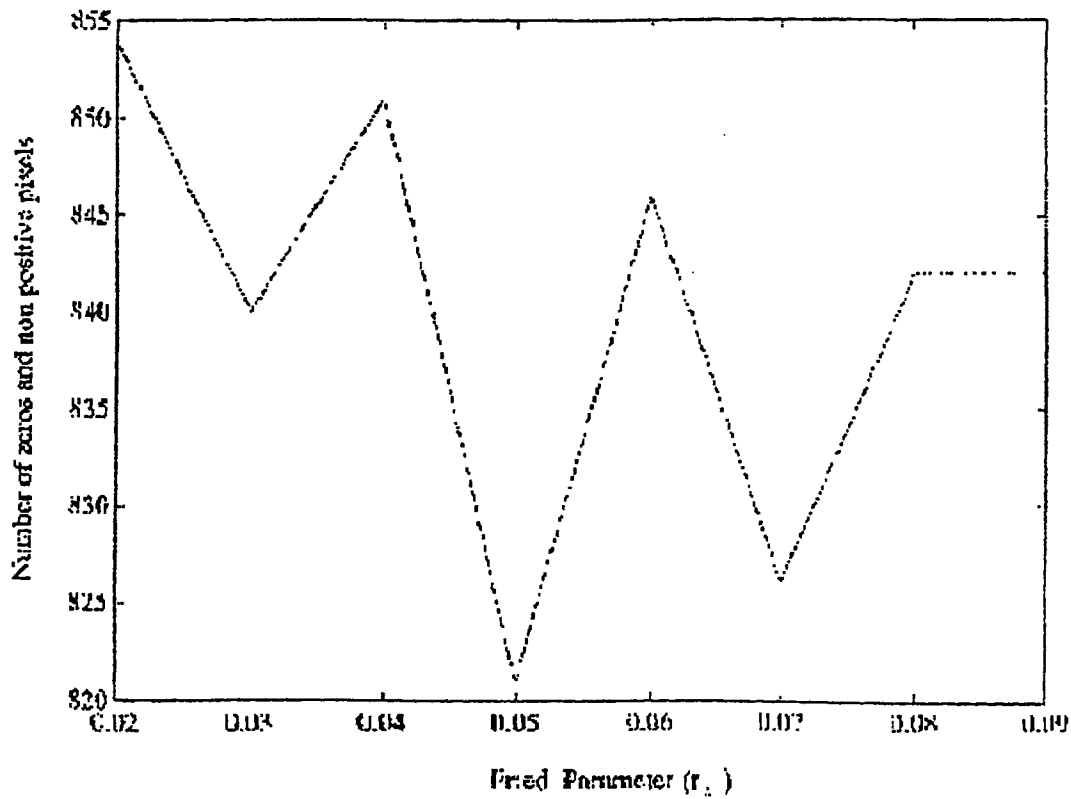


Figure 2.14: Plot of number of non positive pixels N (including zeros in the image plane) in a blurred image with additive Zero mean Gaussian white noise against varying Fried's parameter r_0 . α is fixed at 1.67 which is the true α . The grid size of r_0 is 1.0cm. True $r_0 = 5.0$ cm. Minima in N at $r_0 = 5.0$ cm.

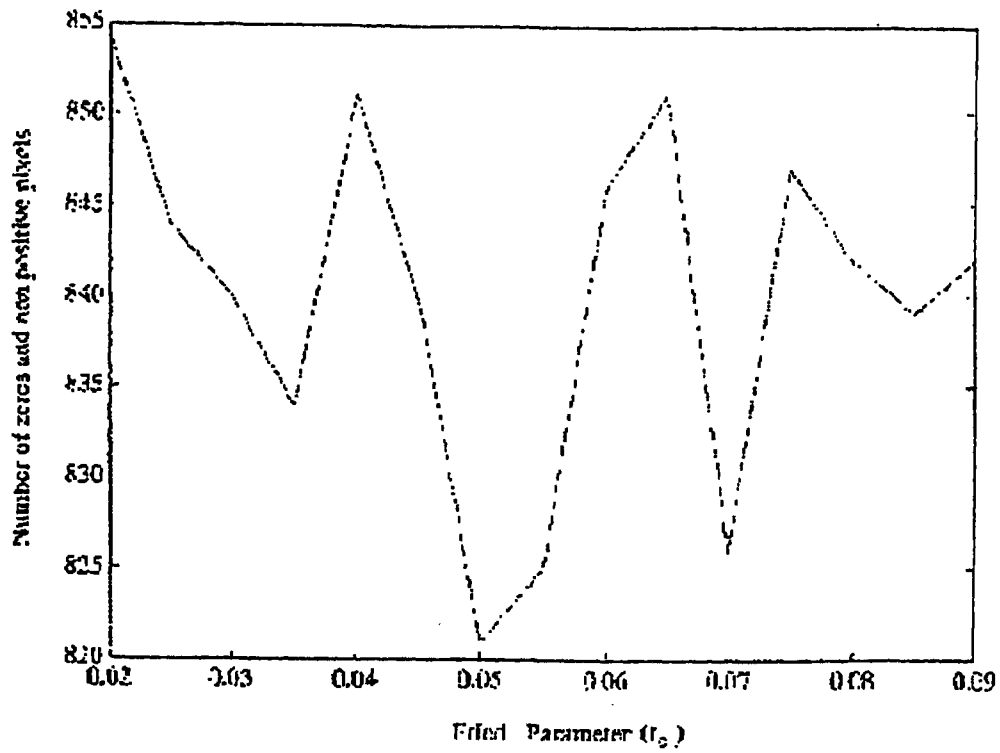


Figure 2.15: Plot of number of non positive pixels N (including zeros in the image plane) in a blurred image with additive Zero mean Gaussian white noise against varying Fried's parameter r_o . α is fixed at 1.67 which is the true α . The grid size of r_o is 0.5cm. True $r_o = 5.0$ cm. Minima in N at $r_o = 5.0$ cm.

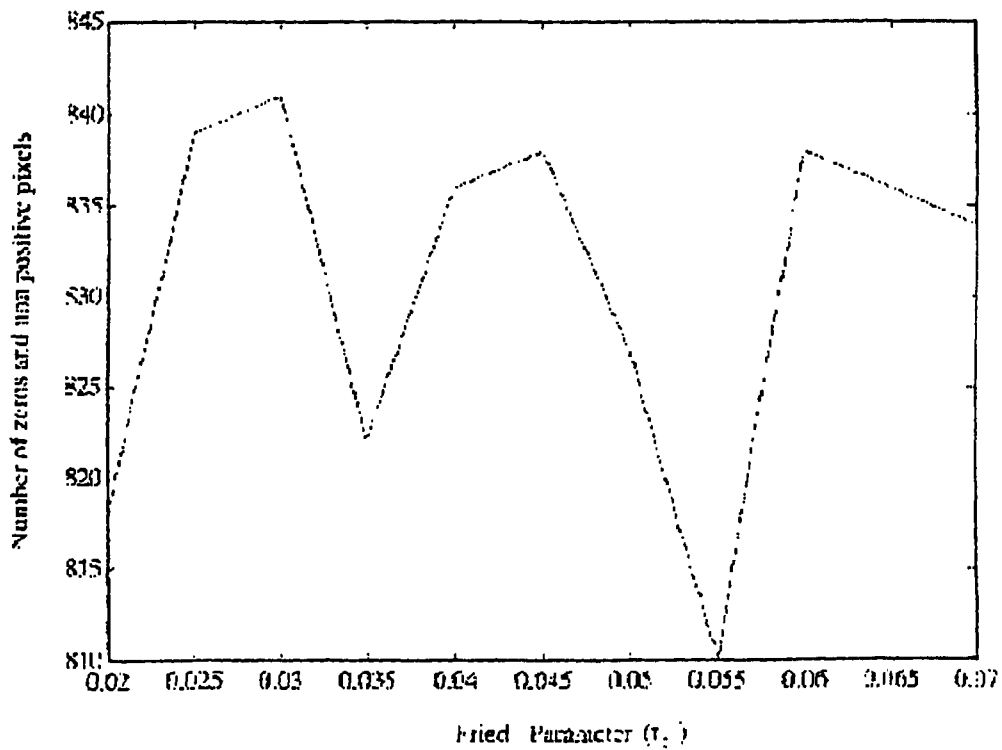


Figure 2.16: Plot of number of non positive pixels N (including zeros in the image plane) in a blurred image with additive Zero mean Gaussian white noise against varying Fried's parameter r_o . α is fixed at 1.67 which is the true α . The grid size of r_o is 0.1cm. True $r_o = 5.0$ cm. Minima in N at $r_o = 5.0$ cm.

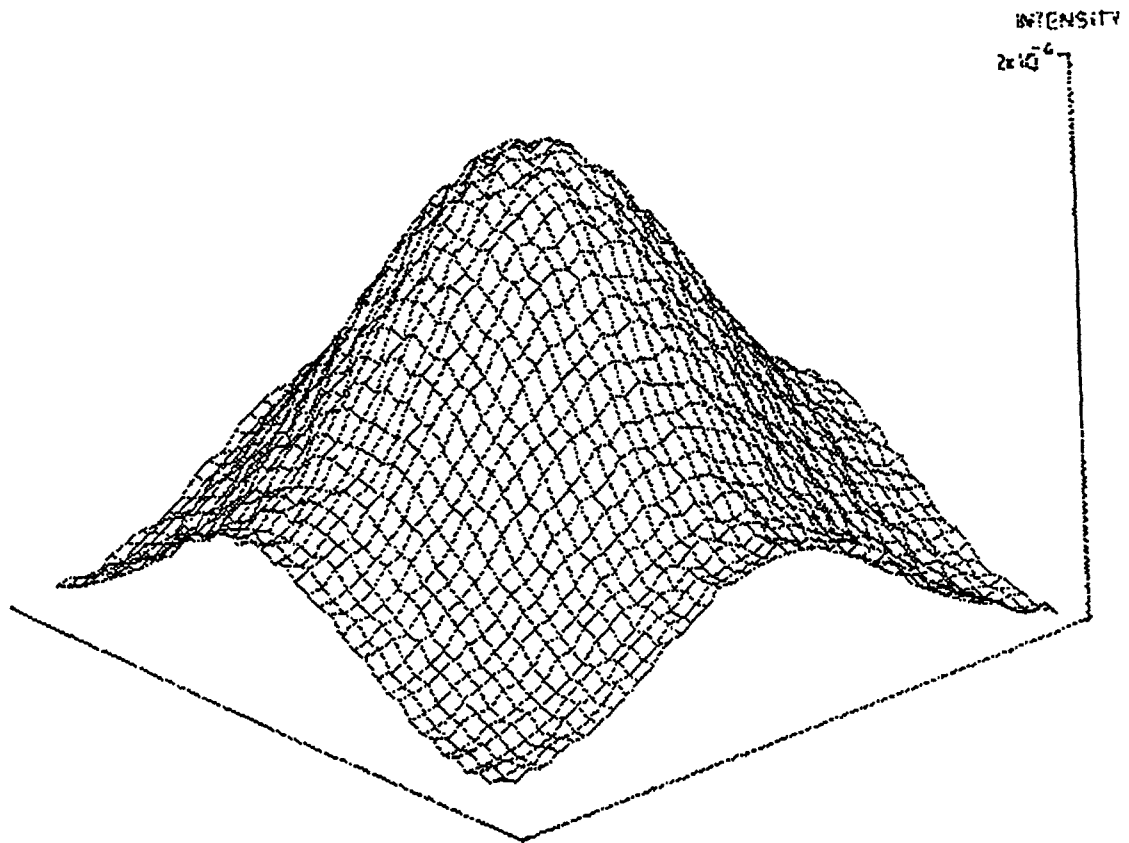


Figure 2.17:
Object intensity distribution degraded by the atmospheric psf. Poisson noise is added to the blurred image. The signal to noise in the image is 5.0.

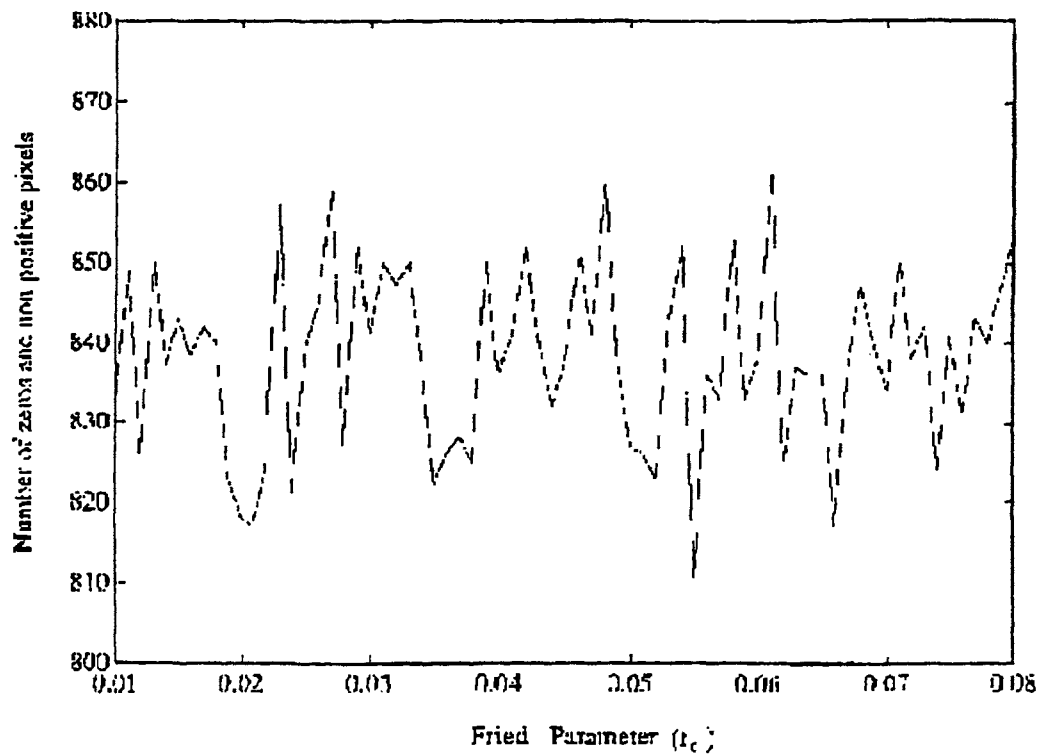


Figure 2.18:
Plot of number of non positive pixels N (including zeros in the image plane) in a blurred image with additive Poisson noise against varying Fried's parameter r_0 . α is fixed at 1.67 which is the true α . The grid size of r_0 is 1.0cm. True $r_0 = 5.0$ cm. Minima in N at $r_0 = 2.0$ cm.

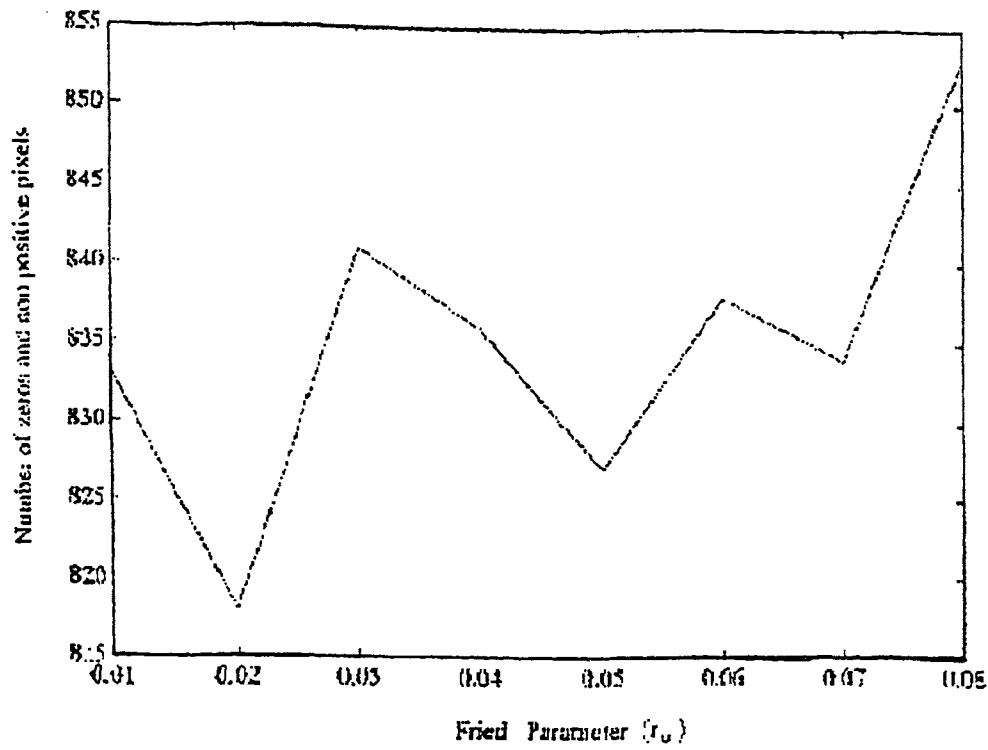


Figure 2.19:
 Plot of number of non positive pixels N (including zeros in the image plane) in a blurred image with additive Poisson noise against varying Fried's parameter r_o . α is fixed at 1.67 which is the true α . The grid size of r_o is 0.5cm. True $r_o = 5.0$ cm. Minima in N at $r_o = 5.5$ cm.

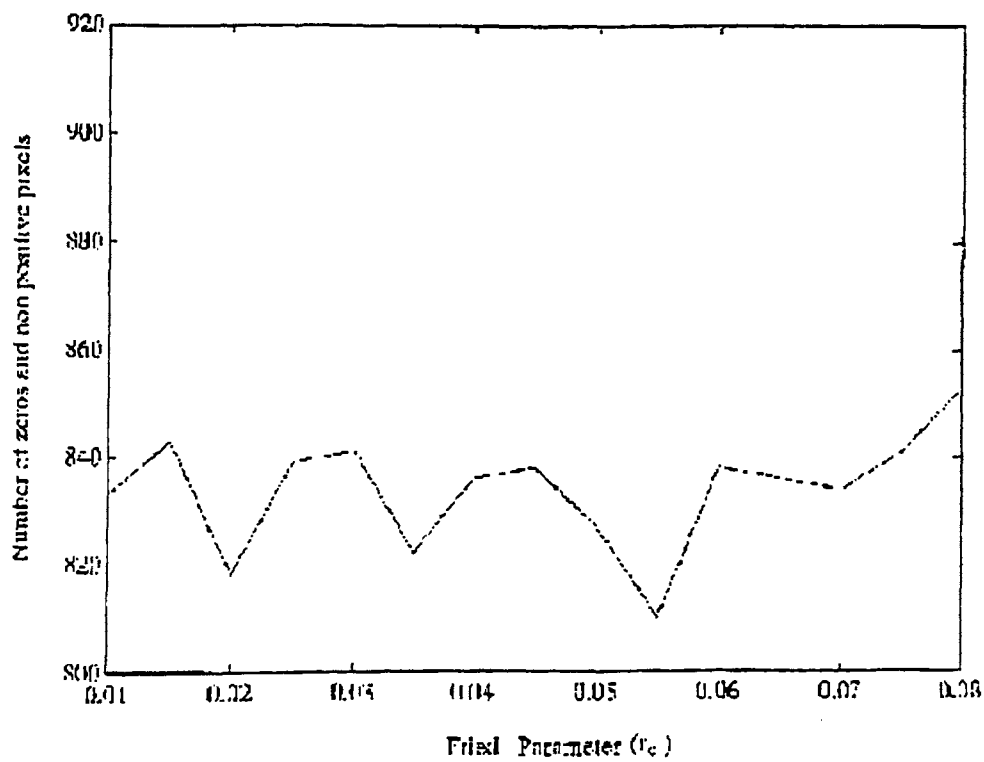


Figure 2.20:
 Plot of number of non positive pixels N (including zeros in the image plane) in a blurred image with additive Poisson noise against varying Fried's parameter r_o . α is fixed at 1.67 which is the true α . The grid size of r_o is 0.1cm. True $r_o = 5.0$ cm. Minima in N at $r_o = 5.5$ cm.

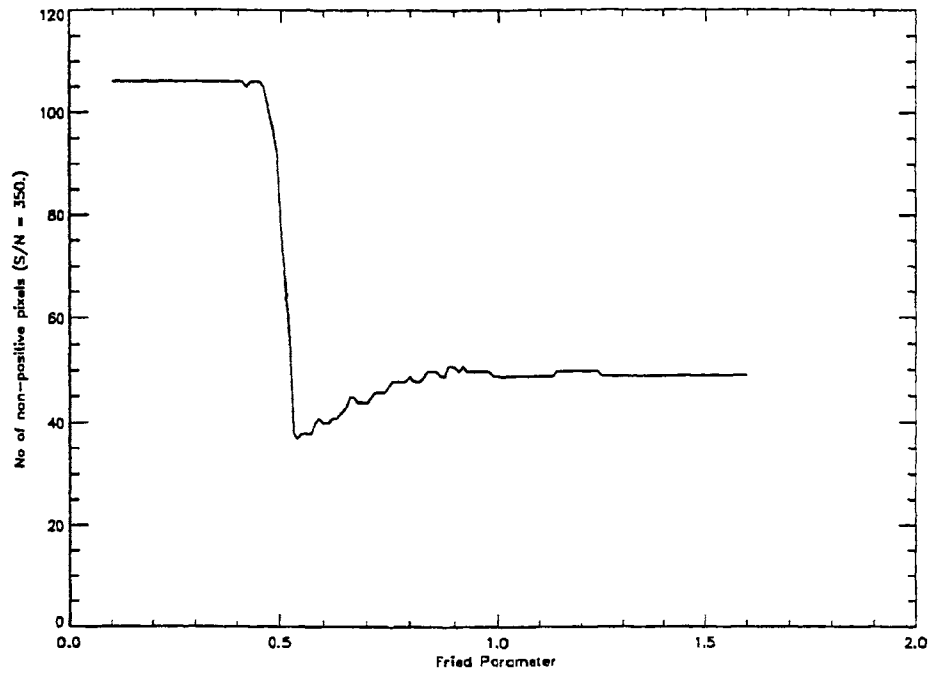


Figure 2.21: Plot of non-positive pixels versus the Fried's parameter. Signal to Noise ratio in the image is 300.0. True $r_0 = 0.5$ (arb.units)

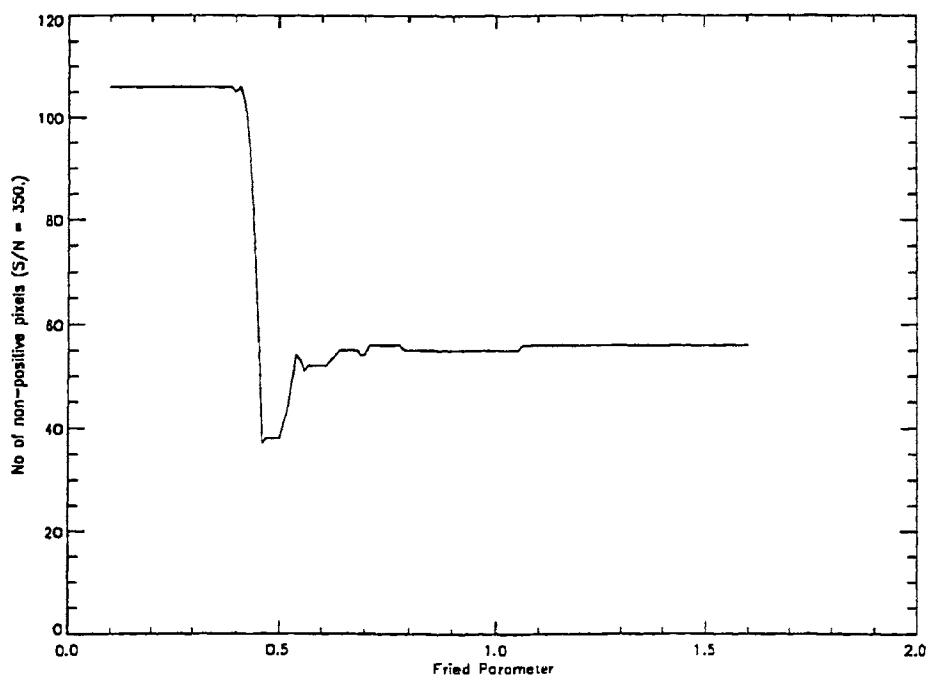


Figure 2.22: Plot of non-positive pixels versus the Fried's parameter. Signal to Noise ratio in the image is 30.0. True $r_0 = 0.5$ (arb.units)

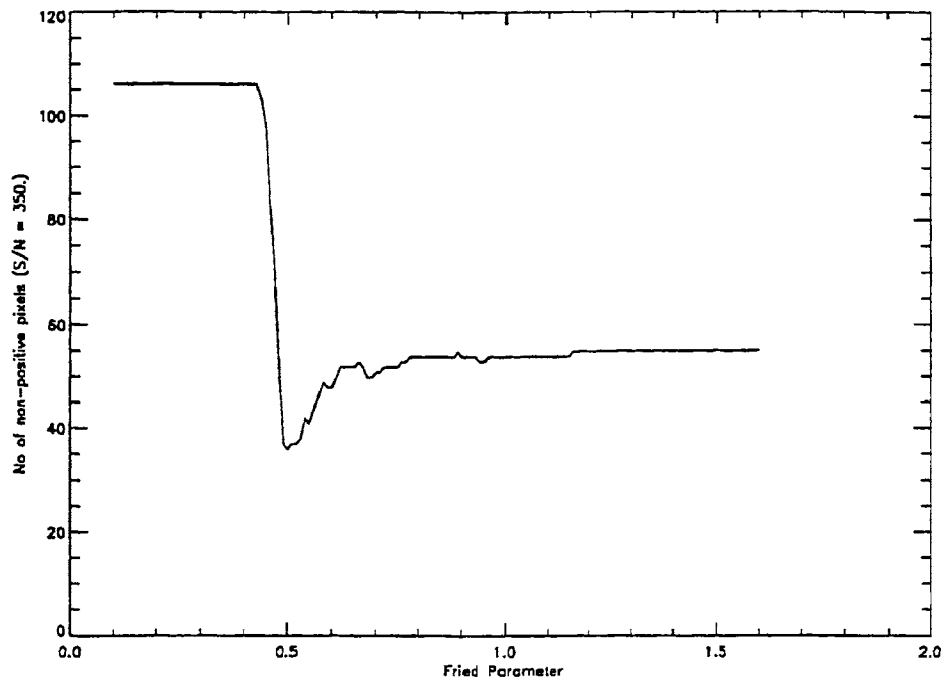


Figure 2.23: Plot of non-positive pixels versus the Fried's parameter. The blurred noisy image is smoothed by a gaussian of width 0.6 (arb. units). Signal to Noise ratio is 30.0. True $r_o = 0.5$ (arb.units)

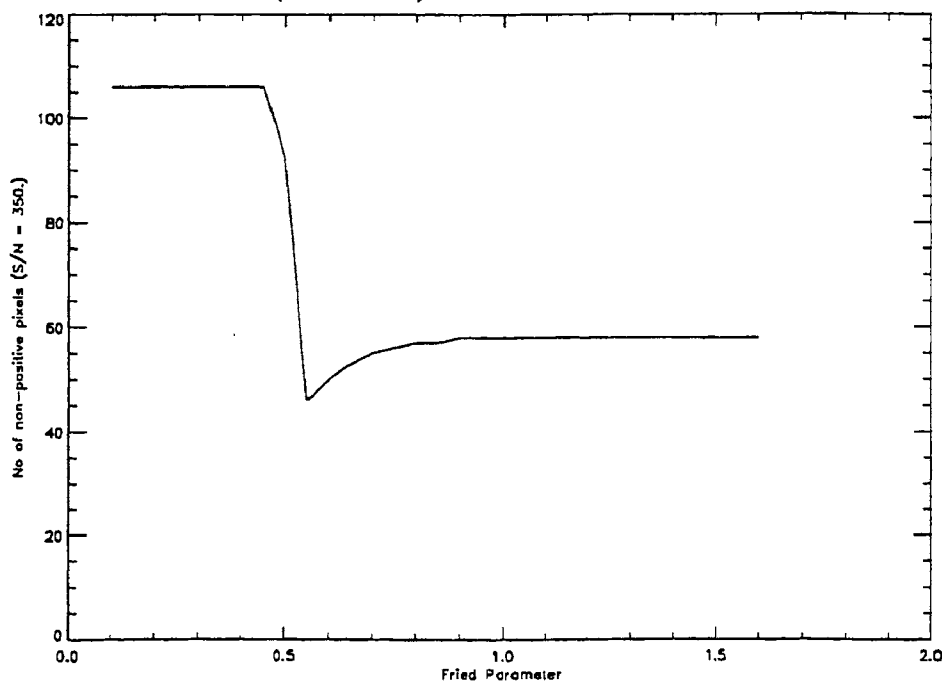


Figure 2.24: Plot of non-positive pixels versus the Fried's parameter. The blurred noisy image is smoothed by a gaussian of width 0.7 (arb. units). Signal to Noise ratio is 30.0. True $r_o = 0.5$ (arb.units)

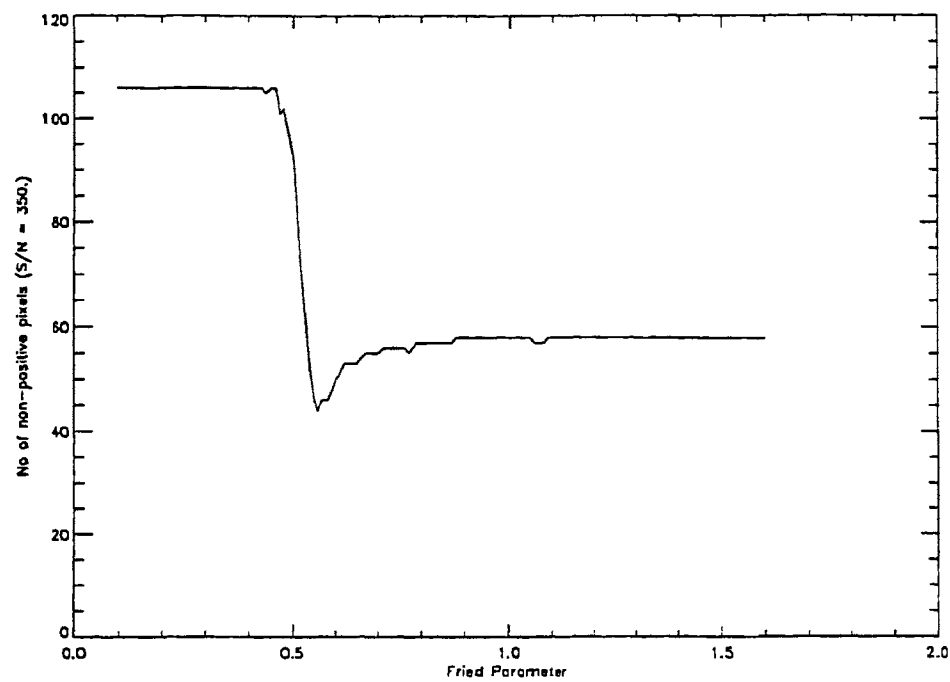


Figure 2.25: Plot of non-positive pixels versus the Fried's parameter. The grid size in $r_0 = 0.01$. The blurred noisy image is smoothed by a gaussian of width 0.7 (arb. units). Signal to Noise ratio is 30.0. True $r_0 = 0.5$ (arb.units)

Generalisation to Images with Background Intensities:

The method discussed in chapter 2 will not be very effective in an image with a high background. However the problem of high background can be overcome to some extent depending on how close our estimate is on the background level. We will address the problem of estimating Fried's parameter in an image with non zero background.

Negatives are clear artifacts in a positive definite image and hence the number of negatives can be used as a measure of the 'distance' between the true image and the restored image. However our aim is not to restore the image but to estimate the psf of the atmosphere using this 'distance' as a parameter for estimating the Fried's parameter.

However in the case of high background or when imaging an object which has only bright feature above a background intensity level the inverse filtering of such an image will either have smaller number of negatives or no negatives. For example in the case of a solar image, there will be both dark as well as bright features about the photospheric intensity level. Hence there will be both positive as well as negative excursions about the photospheric intensity level. The number of negatives will be small and cannot be used for estimating the Fried's parameter. To have a search that is more sensitive to change in parameters, we have to have a different definition for an artifact. We remove a reasonable estimate of the background such that the background subtracted image has no negatives initially. We then perform inverse filtering with a guess psf and count the number of 'negatives' below the assumed zero level. The dependence of the number of 'negatives' on the fractional amount of background is what has been studied.

The number of negatives are estimated by counting the number of negatives in the images after every deconvolution with a guess atmospheric point spread function. The image after deconvolution has negatives in the real domain. Since we are dealing with intensities the negative values are unphysical and we use this to get the Fried's parameter. In the case of image with a background to count the number of 'negatives' we need to remove the background. The removal of background is subjective. In reality even the background will be different in different places on the image. Let us write the object intensity distribution as,

$$o(x, y) = k(x, y) + o_f(x, y) \quad (1)$$

where $k(x, y)$ is the background, $o_f(x, y)$ is the object intensity distribution riding on top of this background. The image we observe after the radiation passes through the atmosphere and recorded in the ground based detector is,

$$i(x, y) = o(x, y) * p(x, y) + n(x, y) = [k(x, y) + o_f(x, y)] * p(x, y) + n(x, y), \quad k(x, y) > 0.0 \quad (2)$$

where '*' denotes convolution, $n(x,y)$ is the noise in the image (primarily due to the detector), $k(x,y)$ is the background which is non-zero and $p(x,y)$ is the atmospheric point spread function. The Fourier transform of this would yield,

$$I(u, v) = [K(u, v) + O_f(u, v)]P(u, v) + N(u, v) \quad (3)$$

where u and v are the spatial frequencies and I, K, O_f, P and N are the Fourier transforms of i, k, o_f, p and n respectively. For the sake of simplicity we will consider the background $k(x,y)$ as a constant. This implies that its Fourier transform will be a delta function and hence removal of it would help us get rid of the background. But this is not the case in reality. In the case of the sun we would have a spatially varying background. But estimating the background pixel by pixel will be a difficult task and we do not address the problem here. By estimating a mean background and subtracting the mean background from the image we can use the parameter search to obtain the Fried's parameter. But the accuracy in determination of the Fried's parameter would depend on the accuracy with which we remove the background. The presence of a DC level will inhibit negative excursions and counting the negatives is not possible.

Therefore the problem is now to find out the the mean background and the dependence of the number of 'negatives' N in the inverse filtered image on the error in our estimation of k .

This empirical method fails when the DC level is present and the features present in the image are not of sharp contrast. In case of features like the sunspot the dark regions of the sunspot has zeros or values close to zero but to estimate Fried's parameter in images where the background is not zero we can use the derivative of the number of 'negatives' in the image to get the true r_o . At r_o lower than the true r_o , even in the presence of a DC level the inverse filtering process removes the higher spatial frequencies abruptly and hence negative excursions are seen. At r_o close to the true r_o the number of 'negatives' in the image falls to a lower value but tends to retain the same number of 'negatives' thereafter. Hence, we find that a derivative of the number of 'negatives' is a good indicator of the true r_o . However the accuracy in estimation of r_o using dN/dr_o also depends on the error in our estimation of the background and its removal.

The simulations were done the following way. We simulate a point source convolved with the atmospheric psf. The atmospheric psf is the long exposure psf and the functional form is,

$$P(f) = \exp[-(\lambda f/r_o)^{5/3}] \quad (4)$$

where λ is the mean wavelength of observation, f is the spatial frequency and r_o is the Fried's parameter. The deconvolution is performed in the Fourier domain using the inverse filtering process for psf's generated for various values of r_o . We inverse Fourier transform

the filtered image and count the number of 'negatives' in the image which is used as an estimator of the Fried's parameter r_o . Here we present the results of two cases. Backgrounds of 0.1 and 1.0 are in arbitrary units of intensity added to the psf. We assume that the object is unresolved and hence what we observe is the atmospheric psf itself. The simulations were done with background levels of 0.1 and 1.0 (in arbitrary units). A normalised atmospheric psf is what we use in the simulations and a background of 1.0 and 0.1 is with respect to this normalised psf.

Fig (1) is the plot of the number of 'negatives' for different values of the Fried's parameter r_o . Here in Fig (1) we assume that the background strength is exactly known and we remove it. We plot the number of 'negatives' N for different values of r_o for various levels of background removed. We can see that the image in which the background is low the tolerance to error in background removal is high. Fig (2) is the plot of N for different values of r_o assuming 99% of the background is removed. For sake of comparison in all the plots we have the plots of N vs r_o at two different background levels. Fig (3) is the plot N vs r_o with 90% of the background removed. We can see that the image in which the background was 1.0 has already lost the presence of minima at the true r_o . Fig (4) is the plot of N for various values of r_o with 75% of the background subtracted from the observed image. The image with a background of 0.1 gives a minimum at the true r_o but we can see the minima losing the identity with error in removal of the background. In Fig (5) we can see that when we remove only 50% of the background, both the images with background 1.0 and 0.1 background levels do not show a minimum at the true r_o , which in our case is equal to 0.6. Fig (6) is the plot of dN/dr_o for different values of r_o without removal of the background. When the background level is 0.1 and 1.0 the maxima in dN/dr_o is at $r_o=0.6$ (true r_o) and $r_o=0.5$ respectively.

In the presence of a background the method of using the number of 'negatives' for estimating the r_o can be done either by the removal of the background or by using the derivative dN/dr_o . Using the derivative is useful when the background level is unknown, but presence of high background level in the image will result in underestimation of r_o .

We also note that although the number of artifacts/negatives is sensitive to the assumed background level, the slope of the variation of the number N with the parameter r_o can be used to detect the actual value of r_o . However we can see that this statement becomes invalid for very high background intensities. In Fig(6) we can see that as the background level goes up, the value dN/dr_o underestimates the value of r_o .

The photon noise which is intrinsic also plays an important role. In the presence of a high background say intensity N per pixel, the photon noise will be \sqrt{N} . The signal to noise

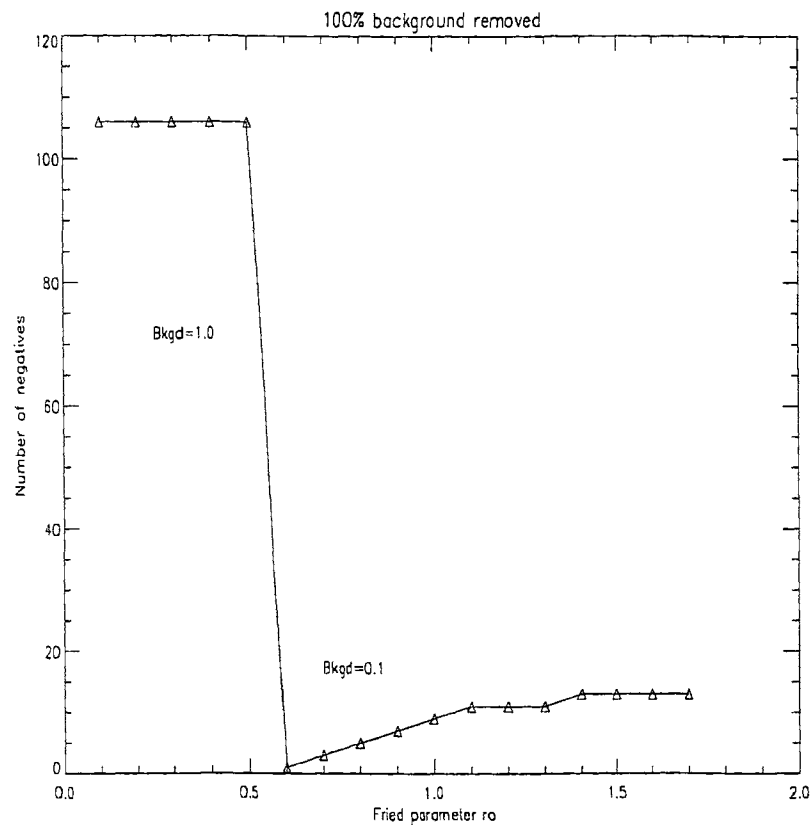


Figure 1: Plot of number of 'negatives' N for various values of r_0 , assuming complete knowledge of background level. (true $r_0 = 0.6$ units)

ratio in the image assuming photon noise as the only source of noise is \sqrt{N} . Therefore the signal to noise per pixel will improve with more photons but estimation of r_0 is accurate when the background is low. When the amplitude of the noise fluctuations becomes larger than the fluctuations in the convolved image, it is not possible to use this method to estimate the Fried's parameter.

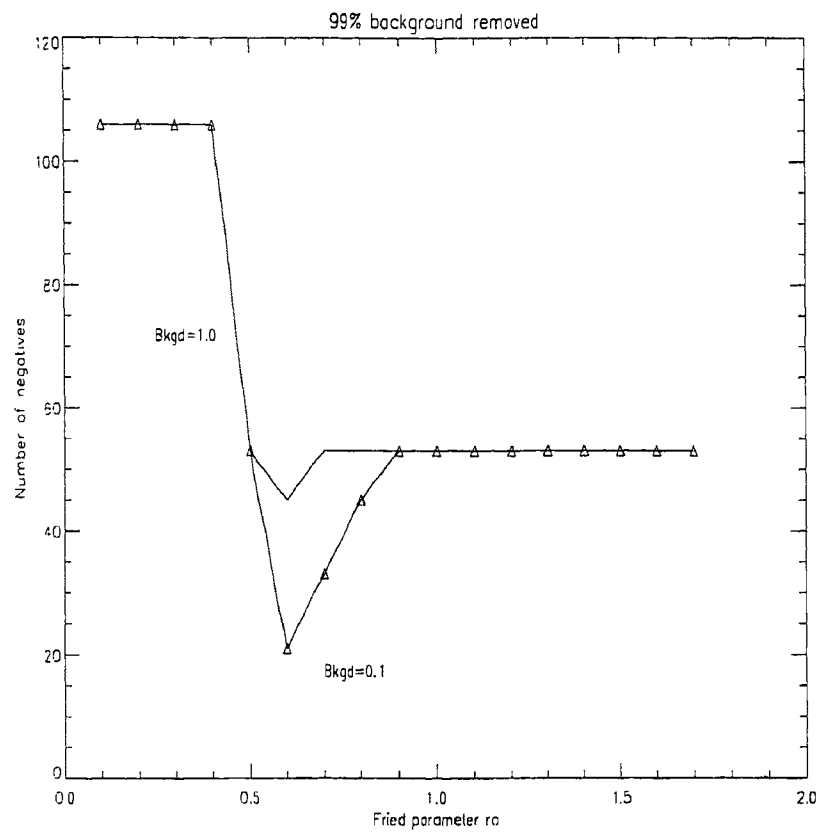


Figure 2: Plot of number of 'negatives' N for various values of r_0 assuming 99% of the background is removed. (true $r_0 = 0.6$ units)

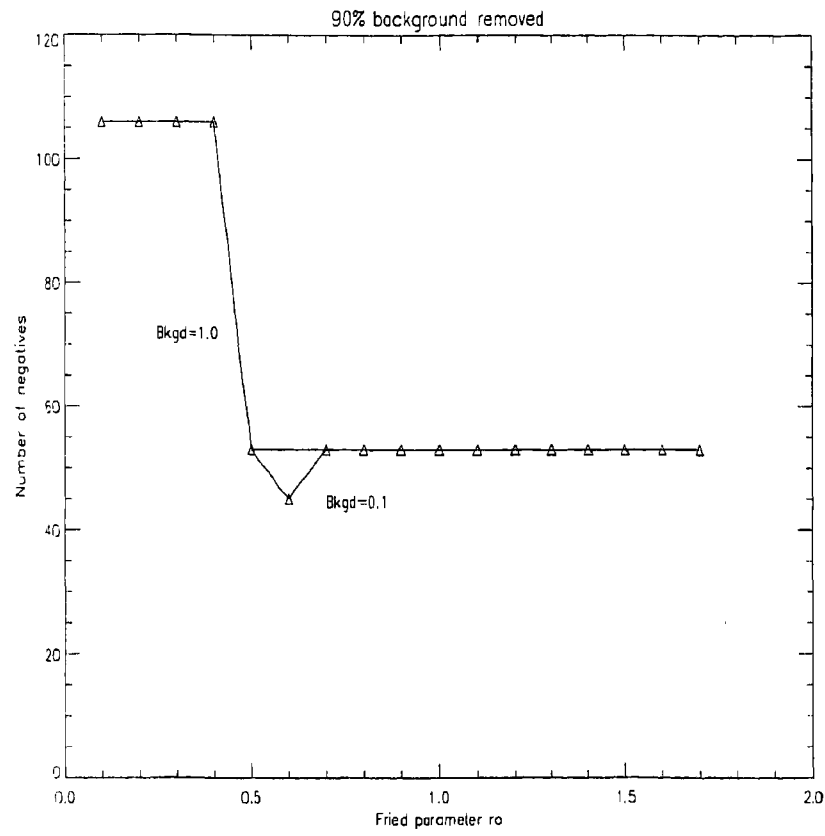


Figure 3: Plot of number of 'negatives' N for various values of r_0 assuming 90% of the background is removed. (true $r_0 = 0.6$ units)

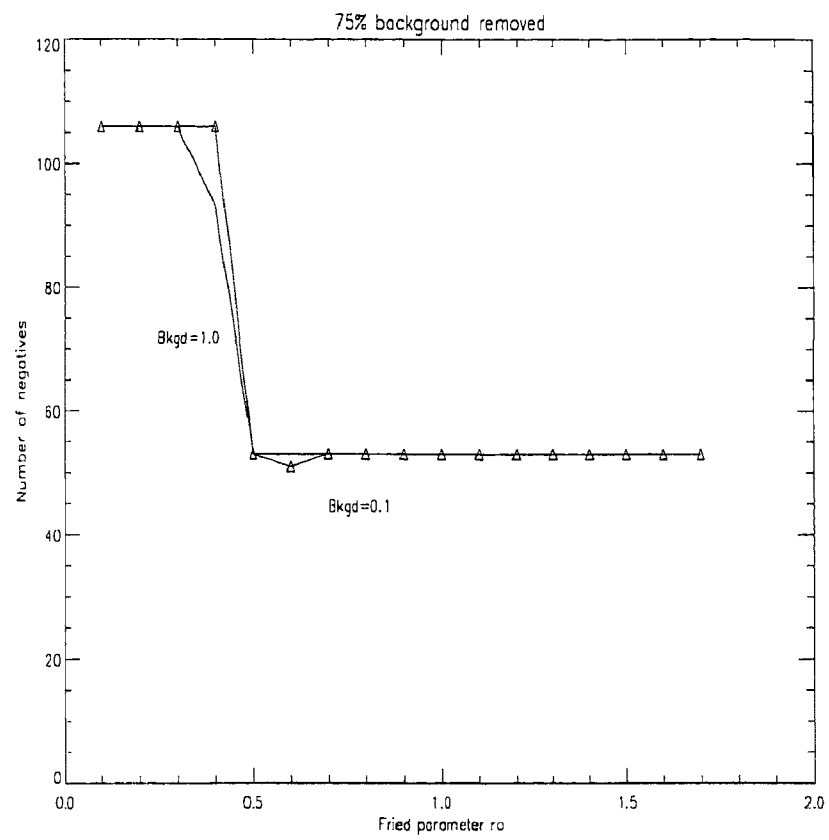


Figure 4: Plot of number of 'negatives' N for various values of r_0 assuming 75% of the background is removed. (true $r_0 = 0.6$ units)

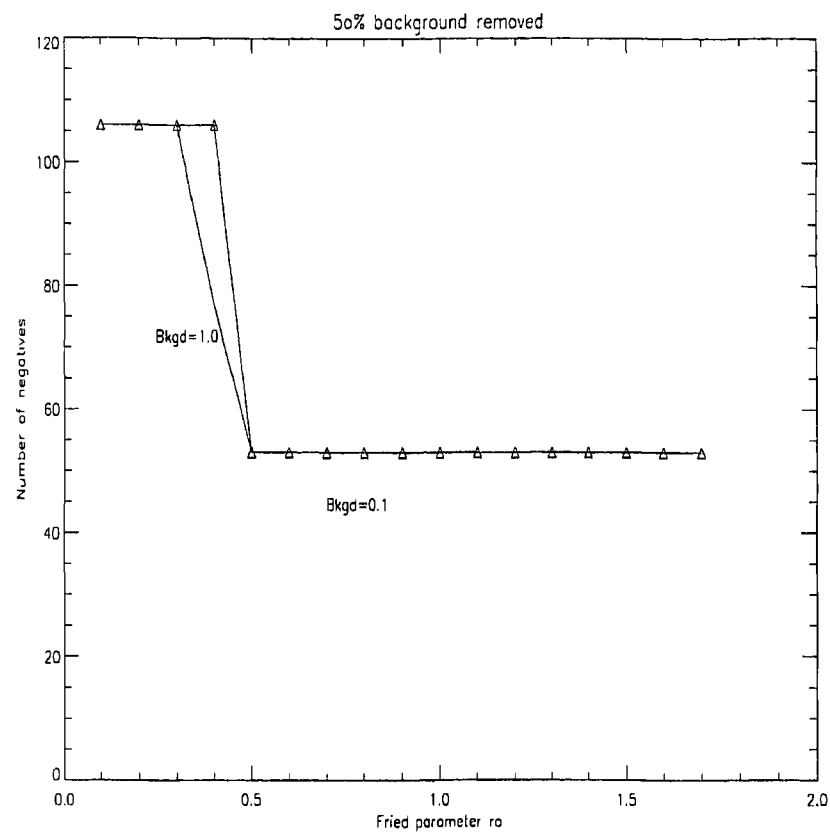


Figure 5: Plot of number of 'negatives' N for various values of r_o assuming 50% of the background is removed. (true $r_o = 0.6$ units)

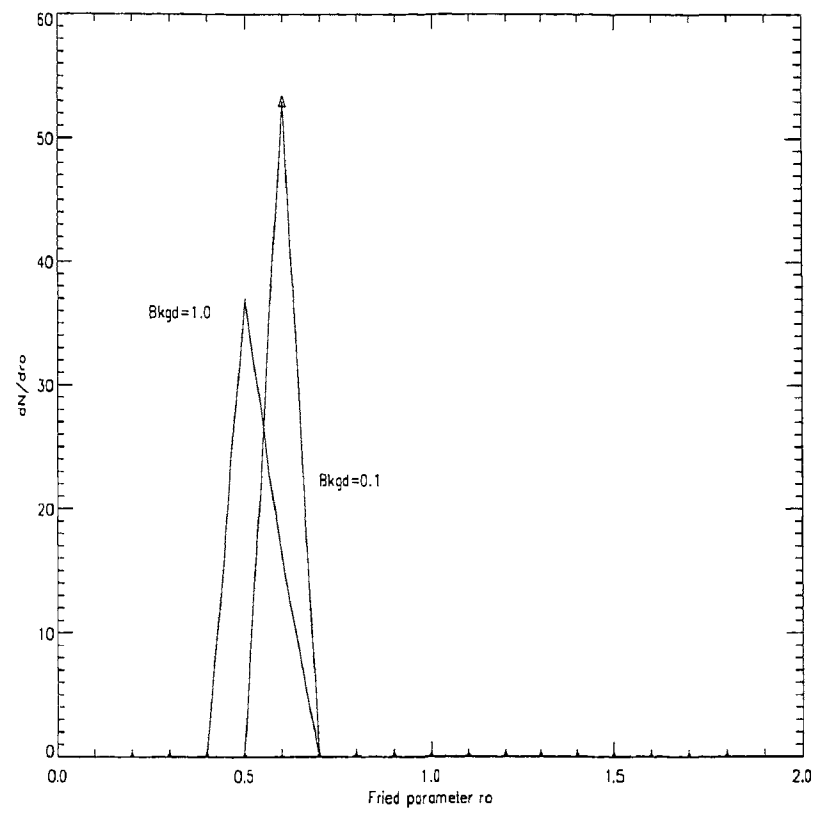


Figure 6: Plot of the derivative of the number of 'negatives' N for various values of r_0 assuming 50% of the background is removed. (true $r_0 = 0.6$ units)

Chapter 3

Search for Fried's Parameter in Globular Cluster image [†]

3.1 Introduction

In the earlier chapter (Krishnakumar & Venkatakrisnan 1997) we used a parameter search method on simulated long exposure images to determine the Fried's parameter r_0 accurately even in the presence of noise. We use this technique on the image of the globular cluster NGC1904 observed using a ground based optical telescope and obtain the Fried's parameter in different parts of the image. We compare these results obtained using parameter search method with the Fried's parameter obtained using a conventional method and show that the results obtained using two different methods are in good agreement.

3.2 Parametric Search Method

We assume a simple image degradation model which is

[†] Krishnakumar V., Venkatakrisnan P., *Astron. Astrophys. Suppl. Ser.* 126, 177-181 (1997)

$$i(x, y) = o(x, y) * h(x, y) + n(x, y)$$

where $i(x,y)$ is the true object intensity distribution, $h(x,y)$ is the atmospheric intensity psf, $n(x,y)$ is the noise, and x and y are the coordinates in the physical space, while $*$ denotes convolution. We assume here that the noise is additive.

The long exposure atmospheric psf in the Fourier domain is

$$H(u, v) = H_o \exp\left[-3.44 \left(\frac{\lambda(u^2 + v^2)^{1/2}}{r_o}\right)^\alpha\right] \quad (3.1)$$

here λ is the mean wavelength of observation, and r_o is the Fried's parameter. The value of α has been theoretically calculated (Fried 1966) and experimentally verified [5] and is equal to 5/3. The spatial frequency coordinates are denoted by u and v .

The observed image $i(x,y)$ is given as the input to the algorithm. The value of λ and a range in r_o is also given as the input. The observed image $i(x,y)$ in which the Fried's parameter has to be found is Fourier transformed. The atmospheric psf is generated in the Fourier domain. The image is inverse filtered and inverse transformed to the physical space. We count the number of negative pixels in the inverse filtered image. Now the original image is again inverse filtered in the Fourier domain and the above process is repeated. Each time the number of negative pixels is counted and stored in an array. The value of r_o for which the number of negative pixels is a minimum is the true r_o .

Even in the presence of noise the minima in N occurs at true r_o . The results of simulations both in the presence and absence of noise has been discussed in the earlier chapter (Krishnakumar & Venkatakrisnan 1997) .

The parametric search method works for point sources as well as for extended sources. The validation of the method was done by estimating the Fried's parameter using the parameter search method and using conventional methods like fitting gaussian profile to the point source and using the full width at half maximum (FWHM) as a measure of seeing. In the following section we describe the method used to validate the method.

3.3 Parametric Search on Globular Cluster NGC1904

We were looking for an image with many point sources in order to estimate the Fried's parameter using conventional methods like fitting a gaussian and using its FWHM as a measure of the Fried's parameter r_o . We chose an image of the globular cluster NGC1904 (observed by Prof. RamSagar and Mr. Alok Gupta at the Vainu Bappu Observatory using the 2.34m Optical telescope) for this purpose.

The image is a 1024×1024 pixel CCD image with a plate scale of $0.6''$. The mean wavelength of observation is 5656\AA . The image of the globular cluster NGC1904 is shown in Fig (3.1). The field is approximately 10 arcminute \times 10 arcminute. The isoplanaticity of the sky is not expected to be of that size. We divide the observed image into smaller sections, each of 50 arcseconds \times 50 arcseconds. The parametric search algorithm is run on each such small sub image and the Fried's parameter is estimated. Since the plate scale and the mean wavelength of observation is known, the Fried's parameter can be now converted to "seeing" in arcseconds in the physical domain.

On each subimage there are several point sources. A best fit gaussian is made for each point source in the sub image and the average FWHM is estimated. This directly gives the seeing in pixel units. The plate scale is known and hence seeing is calculated in terms of arcseconds. A factor of 1.12 needs to be multiplied to these values to take care of the non-gaussian nature of the Fried's coherence function.

Fig (3.2) gives the plot of the seeing estimated both using the parameter search method and also using the average FWHM of the gaussians (corrected for the non-gaussian nature of the atmospheric psf) in each sub image. We see a similar trend in the seeing estimated using the two different methods. The values obtained using the two different methods agree within the error limits.

3.4 Discussions and Conclusions

The main result of this chapter is the practical demonstration of the successful working of the parameter search method. The choice of a star cluster to test the method is very appropriate because the entire object occupies several isoplanatic patches while each stellar member of the cluster provides a point source to provide an unambiguous psf. We see here that the conventional method of fitting a gaussian profile and FWHM of the gaussian fit used as a measure of the Fried's parameter matches well with the Fried's parameter obtained using the parameter search method.

The parameter search method, unlike other techniques, does not look for any specific features in the observed image. This makes it useful in estimating the long exposure atmospheric psf when imaging extended sources like Sun. This is a major step towards recovering information upto the diffraction limit from the atmospherically degraded images imaged using ground based optical telescopes. The presence of optical abberations in the telescope will lead to further degradations. The optical abberations in the telescope do not change over very short time scales and hence it is possible to characterise the abberations in the telescope and remove their contributions in the final image.

Using the parameter search method we have shown that it is possible to obtain the long exposure atmospheric OTF and hence the atmospheric OTF can, in principle, be deconvolved from the observed image. In practice, it is not straightforward to perform this deconvoluiton in the presence of noise. Associated with any imaging instrument and the detector is the noise. This noise gets added to the final image. On the other hand, there are standard techniques to treat noise in deconvolution, and one can use these to extract the maximum possible information about the higher spatial frequencies.

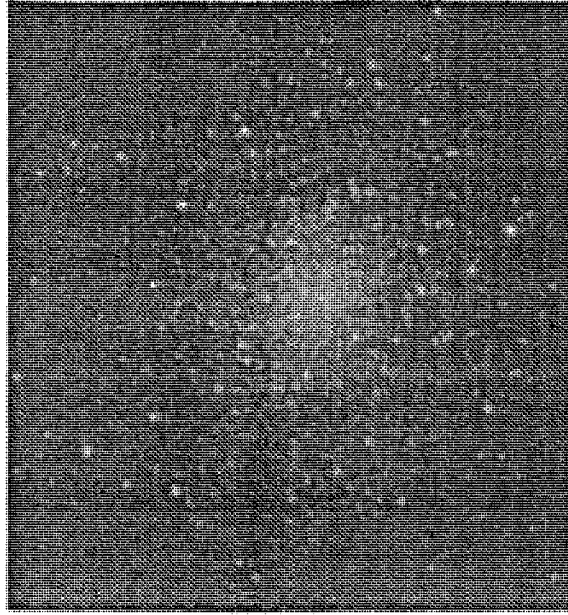


Figure 3.1: Image of globular cluster NGC1904 observed using the 2.34m Optical telescope at Vainu Bappu Observatory, Kavalur. The mean wavelength of observation is 5656\AA .

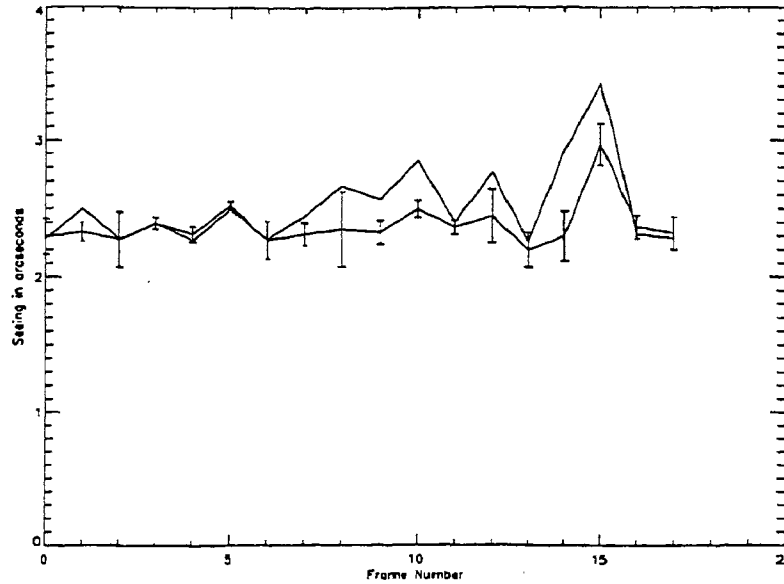


Figure 3.2: Plot of seeing estimate obtained using Parametric search method and seeing estimated using average of $FWHM \times 1.12$ (the factor of 1.12 is multiplied with the FWHM to take care of the non gaussian nature of the Fried's coherence function)

Frame number	Seeing estimated using average FWHM of gaussian fit $\times 1.12$ (in arcseconds)	Seeing estimated using Parametric Search (in arcseconds)
1	2.29 ± 0.22	2.28
2	2.32 ± 0.12	2.50
3	2.27 ± 0.33	2.28
4	2.40 ± 0.07	2.40
5	2.32 ± 0.09	2.27
6	2.53 ± 0.04	2.50
7	2.27 ± 0.23	2.28
8	2.32 ± 0.14	2.45
9	2.35 ± 0.46	2.67
10	2.33 ± 0.14	2.57
11	2.50 ± 0.10	2.85
12	2.36 ± 0.09	2.40
13	2.44 ± 0.33	2.76
14	1.96 ± 0.21	2.26
15	2.05 ± 0.30	2.92
16	2.65 ± 0.26	3.42
17	2.11 ± 0.14	2.31
18	2.50 ± 0.20	2.85

Chapter 4

A Filter for Restoration of Images Degraded by Atmospheric Turbulence

4.1 Introduction

The aim of any restoration procedure is to restore the image without loss of information of the object. In case of astronomical imaging, the limits on resolution is set by the intervening atmosphere.

Even with bigger and bigger telescopes it is not possible to get the object information in entirety. This is because of the gradients in refractive index in the atmosphere. The gradients in refractive index are due to thermal gradients in the atmosphere and these gradients fluctuate in time. Random phase delays introduced in the wavefront degrade the image recorded using ground based telescopes. The statistics of the behavior of these gradients have been studied, both theoretically and experimentally (Bouricius & Clifford 1970; Clifford et al. 1971; Buser 1971).

In any imaging, the information recorded depends on the intervening medium between the object and the imaging instrument, the psf of the imaging instrument, and the inevitable noise associated with any measurement. The psf of the imaging instru-

ment is deterministic. We can determine the instrument psf in the lab by imaging an unresolved source within the spatial extent of the psf of the image forming system. Any restoration procedure tries to restore the blurred noisy image with information as close to the diffraction limit as possible. But, we need efficient filtering techniques to recover object information from images which are degraded by noise apart from blurring.

Filters for noise suppression and high frequency restoration of images degraded by long exposure atmospheric point spread function is presented in this chapter. We also discuss a Wiener filter where the object sharpness is used as a criterion and the filter function is derived by minimising this criterion. We discuss some kinds of noise and try to estimate the filter function to enhance the high frequency information in the object estimate. We discuss the advantages and disadvantages of these filters at different signal to noise ratios. We also show the results obtained after applying these filters on simulations and on real images.

To obtain diffraction limited images we need to know the sources of image degradation. Here, we will deal with the problem of high frequency restoration of information in images in the presence of noise.

4.2 Long exposure and short exposure point spread function

Before we deal with the problem of image restoration we will discuss briefly the long exposure and short exposure atmospheric point spread function. The functional form of long exposure atmospheric psf is symmetric in the physical space, hence its Fourier transform is real in the Fourier space. Short exposure psf is not symmetric in the physical space and hence it is a complex quantity in the Fourier space. Therefore the object's Fourier phase gets corrupted in the case of short exposure imaging. The reason why we go in for short exposure imaging is because the modulation transfer function (MTF) of long exposure atmospheric psf falls off rapidly at higher Fourier

frequencies compared to the short exposure MTF. Hence noise contamination is higher at higher frequencies in the case of long exposure images. The functional form of the long exposure atmospheric psf is such that even though the MTF falls off rapidly it does not go to zero. This property of the long exposure MTF has been exploited to obtain the Fried's parameter r_0 in the earlier chapter.

4.3 Image restoration

Conventional image degradation model is given by,

$$i(x, y) = o(x, y) * h(x, y) + n(x, y) \quad (4.1)$$

in the physical space, and in the Fourier space,

$$I(f) = O(f)H(f) + N(f) \quad (4.2)$$

where f is a function of u and v (spatial frequency variables), $o(x, y)$ is the true object intensity distribution, $h(x, y)$ is the intensity psf, $n(x, y)$ is the noise, and $i(x, y)$ is the degraded image; $*$ denotes convolution; x and y are the coordinates in the physical space; $O(f)$, $H(f)$, $N(f)$ and $I(f)$ are their respective Fourier transforms.

The problem with direct deconvolution procedures like inverse filtering is that the deconvolution becomes ill-conditioned as $H(f) \rightarrow 0$. The general rule is to reduce large inverse values at high spatial frequencies since it is only at these high spatial frequencies the noise is high which leads to severe noise amplification by large inverse values. To counter this one can tune the inverse filter and reduce any large inverse values at high frequencies and hence control the noise amplification. These kinds of filtering does not lead to exact inverse and instead an approximate inverse is performed. In the next section we discuss the different kinds of noise associated with CCD imaging.

4.4 Kinds of noise

The restoration of images in the presence of noise poses a challenge even with advanced techniques available for image restoration in the presence of noise. If the noise frequencies and object frequencies are present at different frequency intervals then one can use a window and retrieve the true object information. The problem of image restoration becomes severe when the noise spectrum occupies the same spectral interval as the object information.

We will discuss few kinds of noise (Newberry, 1994) which is of importance to us and discuss their respective power spectrums.

- 1) Thermal or Johnson Noise
- 2) Shot Noise
- 3) $\frac{1}{f}$ Noise
- 4) Quantizing Noise

Thermal or Johnson noise occurs because of the variations in electron density caused due to the thermal motion of the electron gas. The fluctuation in density of electrons lead to variations in potential difference between the electrical contacts of the recording instrument. The possible frequencies are unlimited and is termed as **White Noise**. The term white noise refers to the spectral shape of the noise power spectrum.

Shot noise is characteristic of any system where the charge collection occurs statistically. For example, in minority carriers flowing across a junction diode, or across the base of a junction transistor to the collector. These fluctuations can also occur at any frequency and hence the noise is termed as **White Noise**.

$\frac{1}{f}$ noise is determined by unknown effects at surfaces, contacts and barriers. It is associated with generation and recombination of minority carriers in semiconductor devices.

Quantizing noise occurs because of the limited capabilities of digital equipments. The digital equipments have a certain number of digits to display. These instruments

can be no more accurate than the number of digits they can handle.

In case of CCD imaging, the kinds of noise introduced in the image are,

- 1) Readout Noise
- 2) Dark Count
- 3) Background Noise
- 4) Processing Noise

Readout Noise: When the signal generated by light falling on a CCD is collected, amplified and converted to a digital value one or more of the above discussed noise degrades the signal. The noise added to each of the pixel by reading the signal is called readout noise.

Dark Counts: Even when light is not falling on the CCD electrons accumulate in the CCD. This adds to the signal generated when light from source falls on it. The rate at which this dark current is produced increases with increasing temperature.

Background Noise: A most commonly overlooked source of noise is this Background noise. Light, from natural skyglow, moonlight, or light pollution contributes to the signal collected by the CCD. This background adds to the photons generated by the true signal. Also any photon measurements have inherent uncertainty which adds to the noise. The presence of this background noise severely degrades the observation.

In general, the image we record can be written as,

$$i(x, y) = i_o(x, y) + i_{bkgd}(x, y) + i_{dark}(x, y) + i_{bias}(x, y) + i_p(x, y) \quad (4.3)$$

where $i_o(x, y)$ is the blurred image intensity distribution, $i_{bkgd}(x, y)$ is the intensity contribution from background radiation, $i_{dark}(x, y)$ is the contribution of thermo electrons, i_{bias} is the contribution from the CCD and $i_p(x, y)$ is the gaussian distributed read out noise.

The noise model can thus be modeled as,

$$n(x, y) = i_{bkgd}(x, y) + i_{dark}(x, y) + i_{bias}(x, y) + i_p(x, y) \quad (4.4)$$

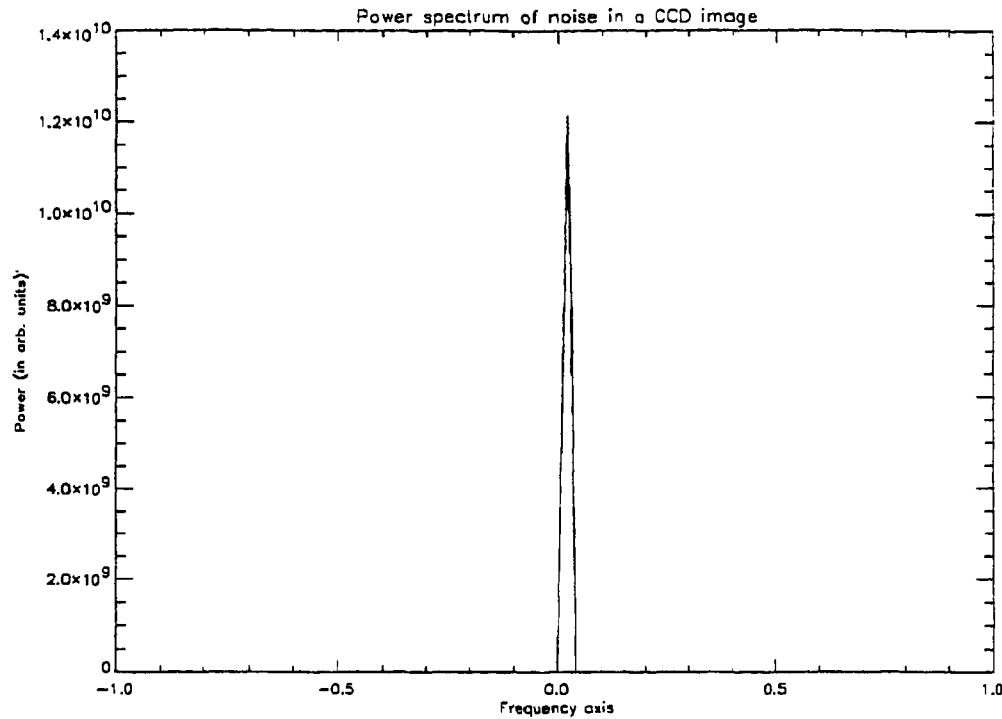


Figure 4.1: Power spectrum of noise obtained from a CCD image. A small area free from object information is selected and used for noise power estimation.

To model $n(x,y)$ in the real image we do the following. In the real image we take a part of the image where object information does not exist. We find the power spectrum of this small portion of the image. The power spectrum has been obtained for a two dimensional image. For the sake of clarity we plot a cut across the power spectrum. Fig (4.1) is an example of the power spectrum obtained from a small area of a CCD image obtained at Vainu Bappu Observatory, Kavalur, India. Bias subtraction and flat fielding has been done on the entire image before the power spectrum is estimated.

The power spectrum of noise in this real image gives us an idea of the noise level in the image. Also we get an idea of the FWHM of the noise power which can be used as an input for constructing the filter.

We see in Fig (4.1) that the low frequency power is higher than the high frequency power. Hence in the Wiener filter we use this information as an input for the Wiener parameter.

4.5 Filter for image restoration

The image we record is blurred by the point spread function of the medium and noise added to this blurred image. The task is to measure the image by removing the blur and the noise. Our aim is to find a filter which when applied to the blurred noisy image will give as output an object estimate which is as close to the true object as possible. We will estimate the true object from the degraded image such that the least square error between the estimated object and the true object is minimised.

If \hat{O} is the object estimate, then

$$\int \int |\hat{O}(f) - O(f)|^2 dudv \quad (4.5)$$

is minimised.

From this we obtain a filter (Goldman 1953),

$$\phi(f) = \frac{\phi_o(f)H^*(f)}{\phi_o(f)H^2(f) + \phi_n(f)} \quad (4.6)$$

We need information on the power spectrum of the true object and the noise to build this filter. The noise power spectrum can be modeled by assuming that beyond a certain cut off frequency the Fourier components of the image does not contribute and hence those Fourier frequencies beyond the cut off frequency are noise contribution. We can then extrapolate the power spectrum of noise into the lower frequency domain and hence model the noise.

In deriving this filter function we try to minimise the least square error in the estimated object to the true object. Additional constraints could be placed on the error estimate and different filter functions can be obtained. (Peter A. Jansson 1997)

4.6 Object sharpness as a criterion for image restoration

Frieden (1975), considers the above problem where he introduces a criterion called the sharpness criterion,

$$\left\langle \int_{-\infty}^{+\infty} \left| \frac{d\hat{o}(x)}{dx} \right|^2 dx \right\rangle = \left\langle \int f^2 |O(f)|^2 df \right\rangle \quad (4.7)$$

where f is a function of u and v . The integration is performed from $-f_c$ to $+f_c$ where f_c is the cut off frequency. Above this cut off frequency the data contain no information about the object $o(x)$. The term $\left| \frac{d\hat{o}(x)}{dx} \right|^2$ is based on the assumption that the object intensity distribution is a smooth function of x and does not have sharp discontinuities. We seek to minimise the equation which includes both the mean square error criterion used earlier in the conventional Wiener filter and the sharpness of the solution such that,

$$\left\langle \int |\phi(f)[O(f) * H(f) + N(f)] - O(f)|^2 df + \beta \left\langle \frac{dO(f)}{df} dz \right\rangle \right\rangle \text{ is minimised.} \quad (4.8)$$

Setting the integrand to 0, we get

$$\phi(f) = \left(\frac{H(f)\phi_o(f)}{H(f)^2\phi_o + \phi_n} \right) \left(\frac{1}{1 + \beta f^2} \right) \quad (4.9)$$

The efficiency of these filters depends on the noise level in the recorded image.

For efficient implementation of the above filters discussed we need the estimate of the ratio of the noise power to the signal power. This ratio is referred to as the Wiener parameter. The noise power spectrum might be flat, smooth or tilted. A reasonable noise model has to be assumed to get an image restored with minimum least square error between the restored and the true object. The image restoration procedure is highly dependent on the noise model we assume. But any reasonable hypothesis of the noise model close to the true noise power spectrum will yield restorations with minimum least square error between the true object and the estimated object.

The power spectrum of noise in CCD images have higher low frequency power than at high frequencies. Hence we will try to model the low frequency power spectrum of

noise. We model the low frequency part of the power spectrum of the noise and the object using a gaussian function with varying width. Let the low frequency Fourier spectrum of the object be,

$$\phi_o^l = e^{-(f/\sigma_o^L)^2} \quad (4.10)$$

and the low frequency spectrum of the noise be,

$$\phi_n^l = e^{-(f/\sigma_n^L)^2} \quad (4.11)$$

where σ_o^L and σ_n^L are the widths of the low frequency part of the power spectrum of the object and the noise respectively.

Hence the ratio of these two will be,

$$\frac{\phi_n}{\phi_o} = e^{-f^2[(\frac{1}{\sigma_n^L})^2 - (\frac{1}{\sigma_o^L})^2]} \quad (4.12)$$

It is reasonable to assume that σ_o^L is always greater than σ_n^L .

Panel 1 in Fig (4.2) is a test object. Panel 2 is the blurred noisy image with a signal to noise ratio equal to 200. The noise added to the image is a gaussian distributed random noise. If we assume the signal to noise ratio a constant at all Fourier frequencies, then the Wiener parameter is a constant at all frequencies. Fig (4.3) is the power spectrum of a gaussian distributed noise. Panel 1 in Fig (4.4) is the plot of the mean square error versus different values of Wiener parameter for an image with signal to noise ratio equal to 200. Panel 2 in Fig (4.4) is the plot of the mean square error versus different values of Wiener parameter for an image with signal to noise ratio equal to 50. Panel 1 in Fig (4.5) is mean square error estimated for an image with signal to noise ratio equal to 200. Panel 2 in (4.5) is an estimation of mean square error for an image with signal to noise ratio equal to 50.

4.7 Deconvolution in the presence of noise

The recovery of signal from blurred noisy image demands a good idea about the blurring function and a good statistical knowledge of the noise in the image.

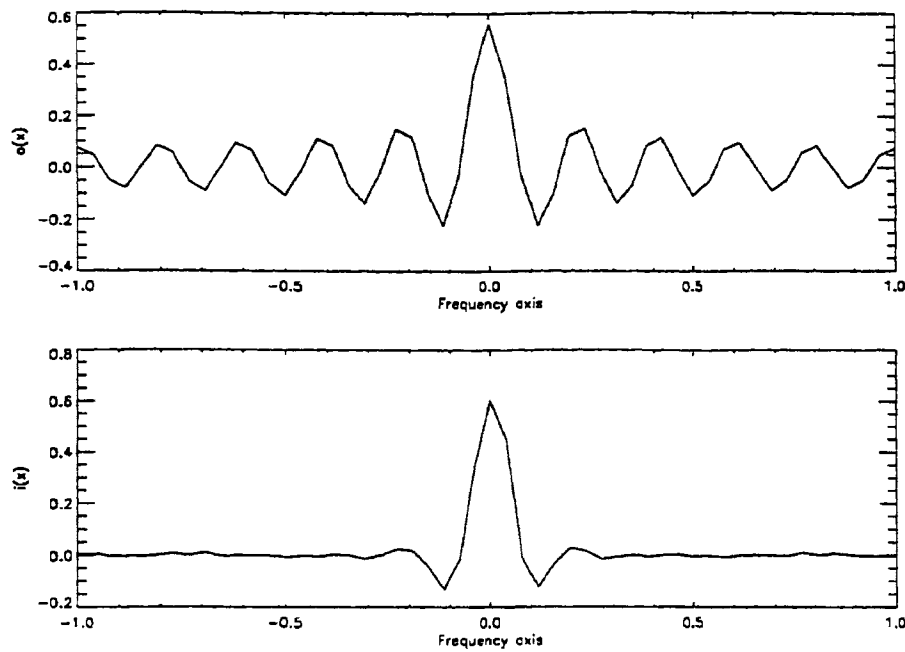


Figure 4.2: Panel 1 is the true object's Fourier spectrum and Panel 2 is the Fourier spectrum of the blurred noisy image of the object in panel 1. The signal to noise ratio is 200.

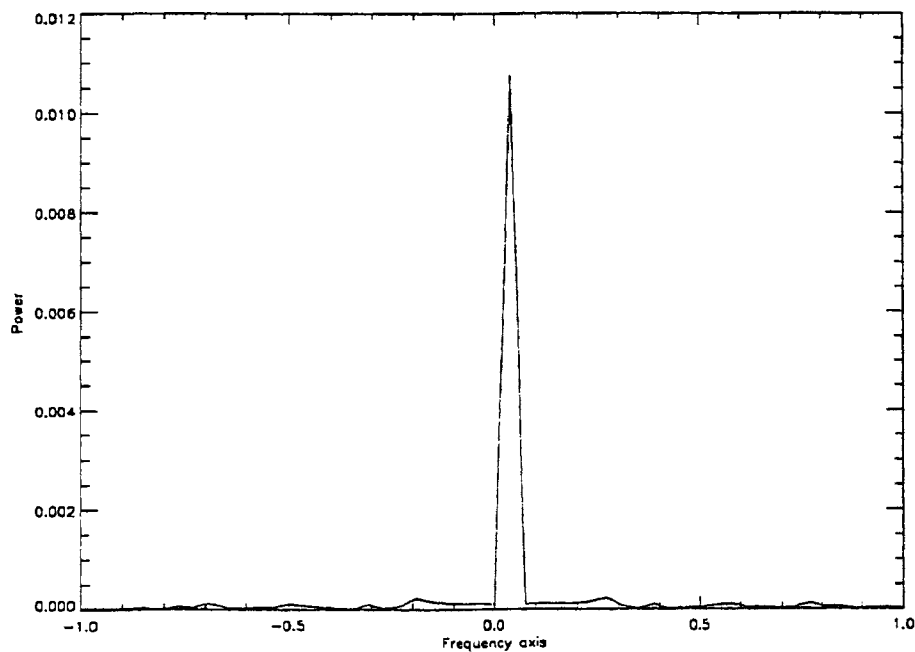


Figure 4.3: Power spectrum of a typical gaussian distributed noise used in the simulations

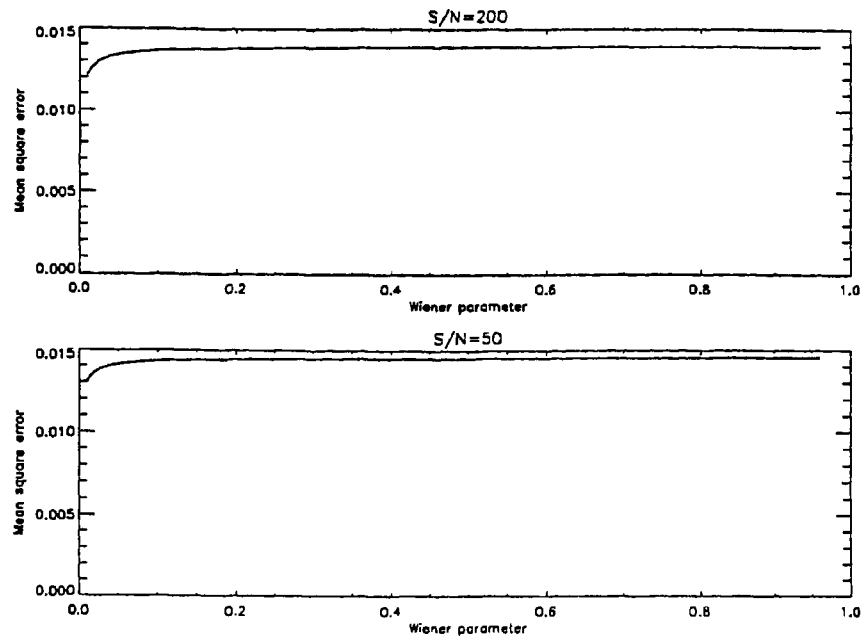


Figure 4.4: Panel 1: Plot of mean square error versus Wiener parameter ($S/N = 200$) Panel 2: Plot of mean square error versus Wiener parameter ($S/N = 50$)

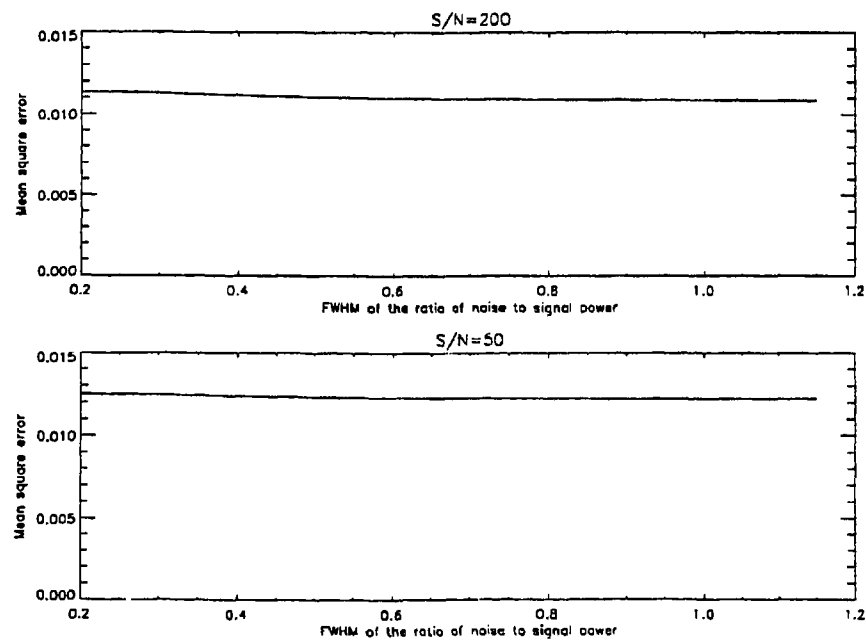


Figure 4.5: Panel 1 : Plot of mean square error for different values of the FWHM of the ratio of the noise to signal power. ($S/N = 200$) Panel 2 : Plot of mean square error for different values of FWHM of the ratio of the noise to signal power. ($S/N = 50$)

In any imaging the signal or the image we record are all corrupted by more than one kind of noise. In case of ground based astronomical imaging the background noise plays an important role in image degradation. This background noise is a combination of the natural skyglow and the inherent noise associated with the photon measurements. Added to this could be the moonlight or light pollution in some cases. The noise which gets added to the image is a combination of different kinds of noise which degrades the original image at every stage. Hence it is appropriate to consider noise as a function of frequency and try to restore images.

Now, the image degradation model in the Fourier space as,

$$I(f) = O(f)H(f) + N(f) \quad (4.13)$$

where $H(f)$ is the point spread function of the medium, in our case it is the atmospheric point spread function and $N(f)$ is the frequency dependent noise.

$$\phi(f) = \frac{H(f)}{H^2(f) + \frac{\phi_n(f)}{\phi_o(f)}} \quad (4.14)$$

here $\frac{\phi_n(f)}{\phi_o(f)}$ is not replaced by a constant as was done in the case of a conventional Wiener filter.

We consider an object which has sharp discontinuities in the physical space so that it has higher Fourier frequencies. In Fig (4.6), the 3 different panels shows the frequency response of the Wiener filter, the frequency response of the filter obtained by including the sharpness in the object in the minimizing criterion and the filter derived by modeling the noise power spectrum and hence the Wiener parameter is not held a constant but rather is modeled from a small area in the observed image itself, as described earlier.

To test the restoration of the filter we construct an object which has high frequency components. Panel 1 in Fig (4.1) is an example of such an object. The blurring function is taken to be a long exposure point spread function. Frequency dependent noise is added to this blurred image. The signal to noise ratio in this example is roughly 200. To check for the dependence of the filter's frequency response

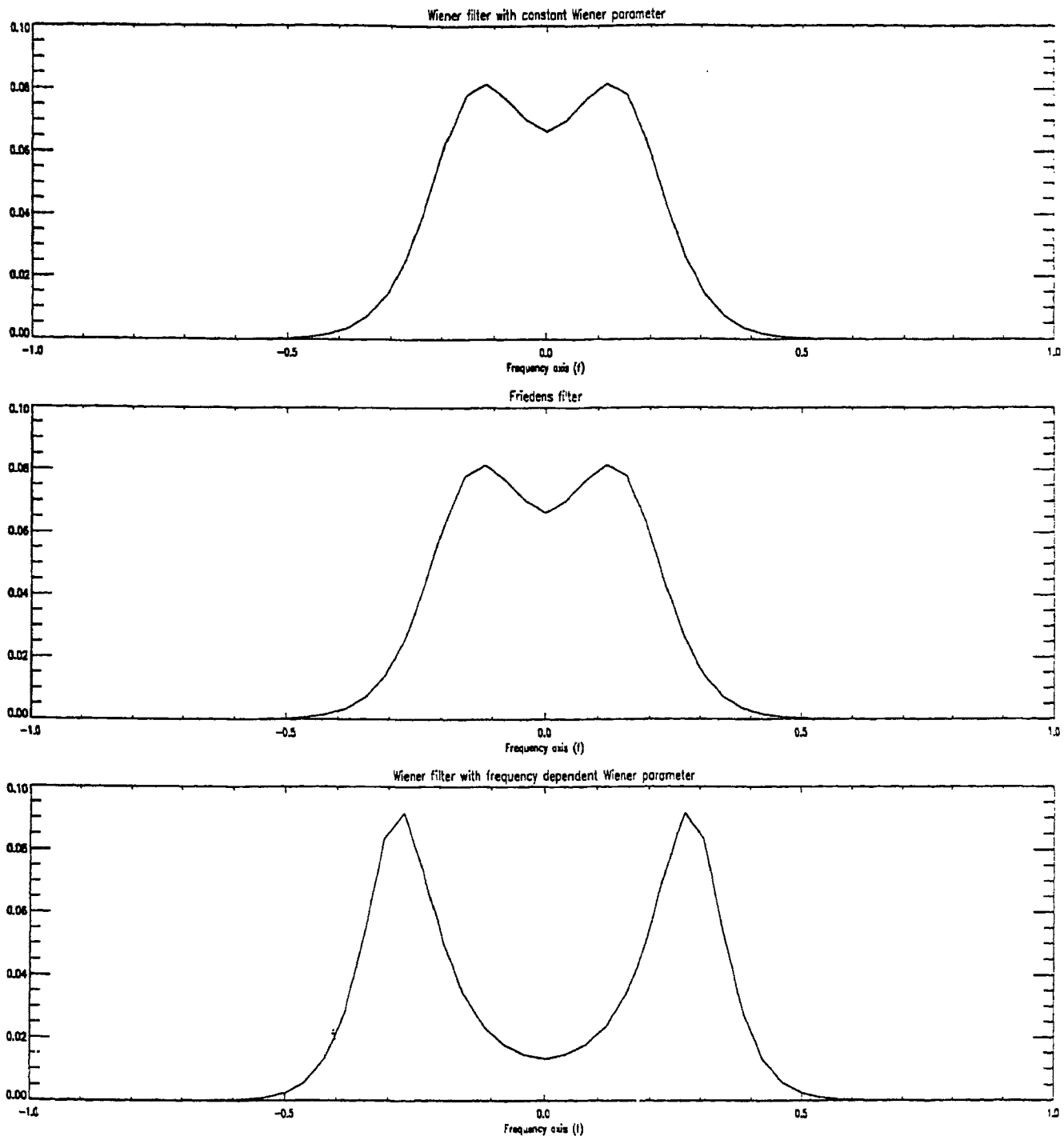


Figure 4.6: Frequency response of the filters.

to the Wiener parameter, the restorations were carried out for various values of the Wiener parameter. We also tested for the dependence of the restoration with error in estimation of the width of the true point spread function. In all these simulations the noise added to the image is gaussian distributed.

In the next section we show with some examples the restoration of images using these filters, their advantages over the others at different signal to noise ratios. The performance of these filters also depend on our a priori knowledge about the psf which has blurred the true object.

4.8 Simulation of objects and restoration using different filters:

We will use the Fourier spectrum of the true object shown in panel 1 in Fig (4.1) in our simulations. We try to recover the true object's Fourier spectrum from the Fourier spectrum of blurred noisy images generated with different signal to noise ratios. We will confine ourselves to restoration of images at signal to noise ratios 50 and 200. To determine the sensitivity of the restoration procedure we plot the mean square error between the restored Fourier spectrum and the Fourier spectrum of the true image as a function of the free parameter in the filters. The free parameter in conventional Wiener filter is the Wiener parameter and the free parameter in the noise modeled Wiener filter is the FWHM of the noise power spectrum. We see that the overall mean square error is less in the case of restoration using noise modeled Wiener filtered Fourier spectra compared to the ones restored using conventional Wiener filtering.

The restorations were tried out for different values of Wiener parameter and different widths for the noise power spectrum. Fig (4.7) is one such of restorations. These restorations were performed on images with signal to noise ratio equal to 200. Panel 1 is the Fourier spectrum obtained using the conventional Wiener filter for filtering the noisy spectrum, panel 2 is the Fourier spectrum of the noisy image obtained

using the Wiener filter with object sharpness criterion and panel 3 is the Fourier spectrum obtained using the Wiener filter where noise is modeled. We see that the recovery of the high frequency information is more pronounced in the case of noise modeled Wiener filter compared to the other two filters. The plots of mean square error versus Wiener parameter in the conventional Wiener filtering and the plot of mean square error versus the FWHM of function describing the noise to signal ratio are given in Fig (4.4) and Fig (4.5) respectively.

For a realistic simulation of images degraded by atmospheric turbulence the following was done.

An object intensity distribution is simulated and is convolved with the short exposure atmospheric psf. The short exposure psf was generated the following way. We assume a power spectral density of the form (Tatarski, 1961),

$$\rho(f) = \frac{L_o^{11/3}}{(1 + f^2 L_o^2)^{11/6}} \quad (4.15)$$

where L_o is the aperture size or the outer scale of turbulence and k the spatial frequency is given as $f = \sqrt{(u^2 + v^2)}$. This is taken to be the power spectral density of the turbulence. This is now multiplied with $\exp(i \phi)$, where ϕ is the random phase generated uniformly between $-\phi$ and $+\phi$. This resulting pattern in u, v space is Fourier transformed to yield one realisation of the wavefront. The object intensity distribution is convolved with the simulated short exposure psf. The result is a short exposure image of the object. A gaussian noise is added to this degraded image. Several such noisy degraded images are realised. These noisy degraded images are used as test images for processing using the Wiener filter with frequency dependent Wiener parameter for image recovery and restoration.

For different values of signal to noise ratio and also for varying values of outer scale of turbulence L_o simulations were done. The results are presented here. Fig (4.8) is the true object intensity distribution used in the simulations. Fig (4.9) is the short exposure image of the object with noise and Fig (4.10) is the restored image. Fig (4.8) was generated by an power spectral density with outer scale of turbulence equal to 250cm. The width of the filter used in the Fourier space is 0.3. The number of

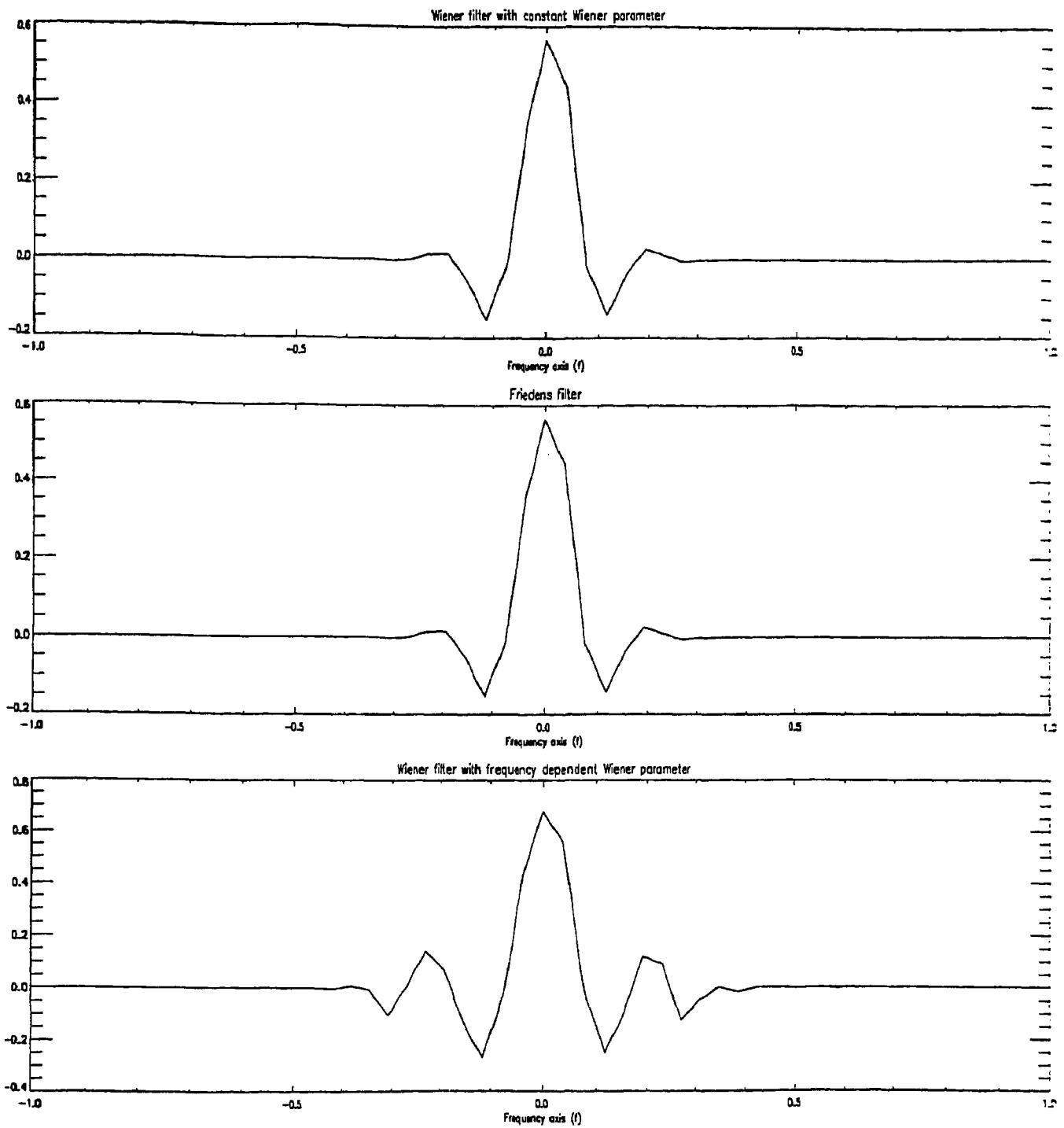


Figure 4.7: Fourier spectrum of the image restored using different filters. In panel 2 $\beta=0.01$ and in Panel 3 the width of the gaussian representing the ratio of noise to signal power is 0.7

short exposures added is 50. The signal to noise ratio in the image is 100.

In the restored image we see that the high frequency information is restored to a great extent. The sharp edges are clearly seen and the four squares are distinctly seen.

4.9 Application of Filters on real images

4.9.1 Images of Globular cluster

We used the image of Globular cluster NGC1904. (observed by Prof. RamSagar and Mr. Alok Gupta using the 2.34m telescope at the Vainu Bappu observatory, Kavalur, India). The mean wavelength of observation is 5656\AA . The image is roughly $60 \text{ arcseconds} \times 60 \text{ arcseconds}$. This image is cut into small portions of $5 \text{ arcsecond} \times 5 \text{ arcseconds}$. Here we show a restoration of one portion of the image. Fig (4.14) is a contour map of a part of the Globular cluster NGC1904. Fig (4.15) is the image restored using the Wiener filter in which the noise to signal ratio is modeled. A Wiener parameter of 0.01 is used in both the filters.

4.9.2 Comet images

To test the filter restoration was performed on images of comets observed at the Vainu Bappu observatory, Kavalur, India. The observations were carried out in 1m and 2m telescopes. The details of observations are,

Telescope	1m
Filter	R
Central Wavelength	6000\AA
Bandwidth	1000
Plate Scale	$16'' / \text{mm}$

Telescope	2m
Filter	R
Central Wavelength	6000Å
Bandwidth	1000
Plate Scale	24" / mm

The details of the CCD camera which was used for imaging are as follows. In 1m telescope the CCD camera used had the following characteristics. It is a Tek1024 CCD camera. The CCD camera used in the 2m telescope had a gain of 5.9e/ADU measured with 16 bits. Noise at 7.2 e^- rms. At 4X setting, the gain is 1.4 e/ADU. In the 1m telescope for a gain of 13 e/ADU the noise is 7 e^- rms. The data we get is 16 bit data. It is a Thomson 512 X 378 pixel chip with a plate scale of 16" per pixel.

4.9.3 Results

The object was observed using a CCD camera. This image is then flat fielded and bias subtracted. This flat fielded and bias subtracted image is then Fourier transformed and multiplied in the Fourier space with the Wiener filter. We can see structures in the restored image all the way upto 40 arcseconds. The central region is blocked so that the other fainter features are seen when the image is displayed.

Fig (4.11), Fig (4.12) and Fig (4.13) are the original images and the restored images of the comet. The image on top is the original image and the images displayed at the bottom are the restored image. The bow like structures far away from the core and finer features near the core are seen in the restored image.

4.10 Discussions and Conclusion

In this chapter we have attempted to highlight the problem of image restoration in the presence of noise. Here we have considered the noise introduced when an image is observed using a CCD camera. Several attempts have been made and are being

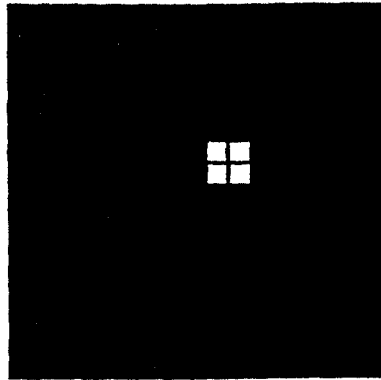


Figure 4.8: *Simulated object intensity distribution*

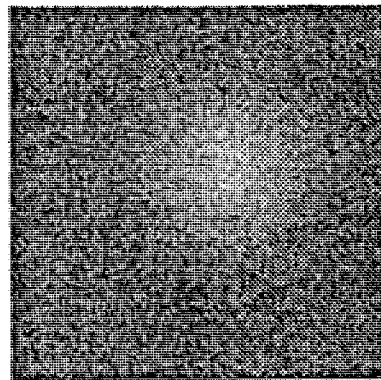


Figure 4.9: *Blurred and Noisy image*

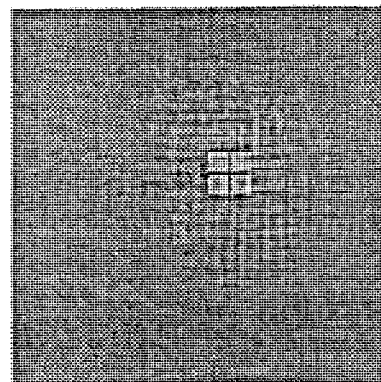


Figure 4.10: *Image obtained by successive addition of short exposure image filtered using noise modeled Wiener filter*

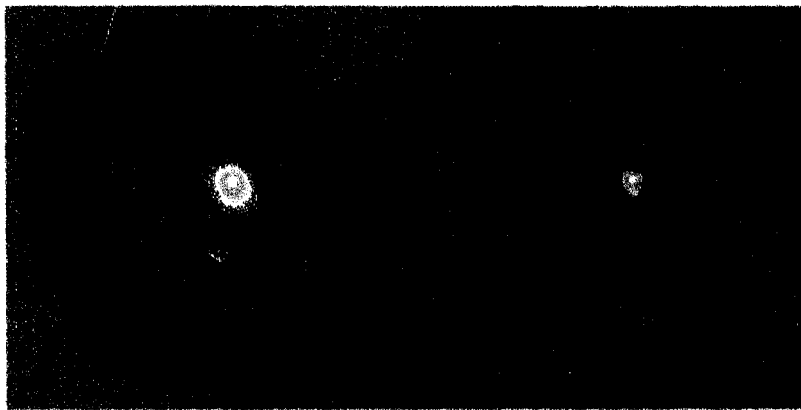


Figure 4.11: *On the left is the image of comet Hale Bopp as observed at the 2.3 m optical telescope at Vainu Bappu Observatory, Kavalur, India. The image on the right is the restored image.*



Figure 4.12: *On the left is the image of comet Hale Bopp as observed at the 2.3 m optical telescope at Vainu Bappu Observatory, Kavalur, India. The image on the right is the restored image.*

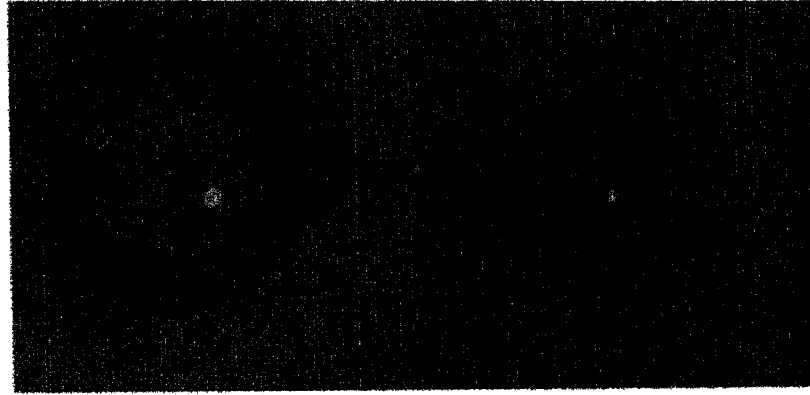


Figure 4.13: On the left is the image of comet Hale Bopp as observed at the 2.3 m optical telescope at Vainu Bappu Observatory, Kavalur, India. The image on the right is the restored image.

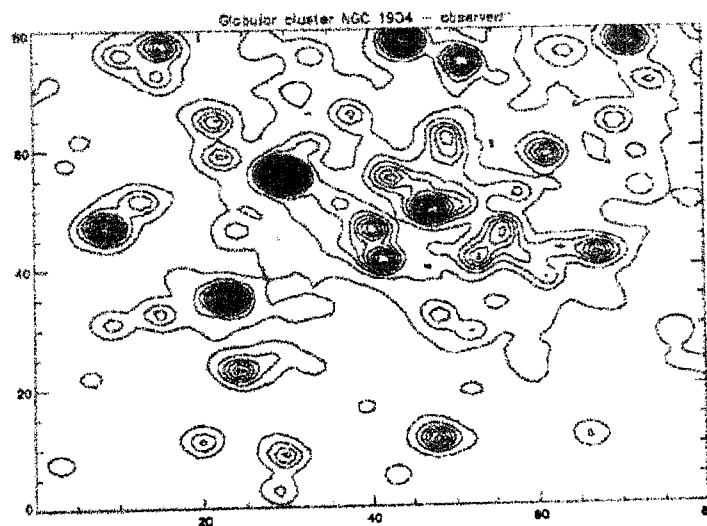


Figure 4.14: Contour map of 5'' X 5'' portion of the original image of the globular cluster NGC1904.

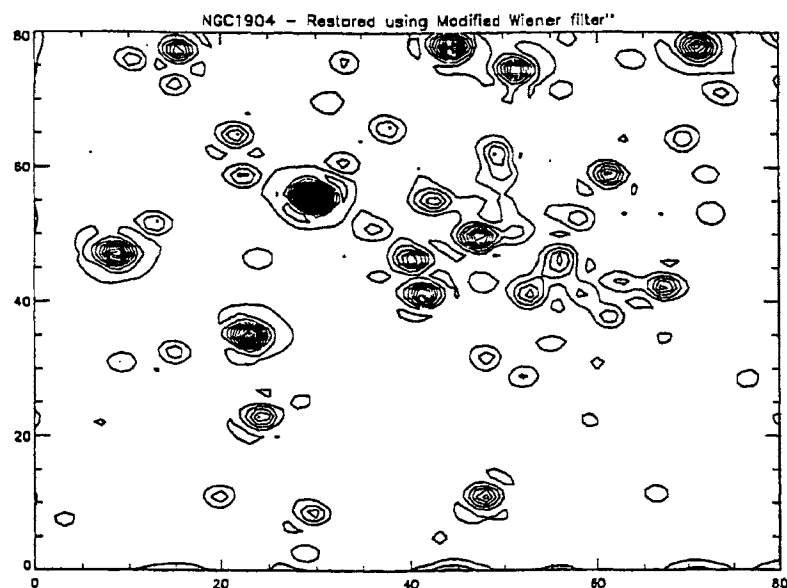


Figure 4.15: Contour map of the image filtered using Wiener filter constructed using noise model. The dotted line corresponds to negative values. Wiener parameter W is 0.01.

made to alleviate the problem of image restoration in the presence of noise. Since noise is not a deterministic process we try to model the ratio of the noise to signal power. We have shown that any reasonable hypothesis for obtaining the Wiener parameter can restore some of the high frequency features. Noise contributes over a wide range of Fourier frequencies hence, any attempt to remove noise removes some of the true object's information.

If the seeing is poor, then the higher frequencies in the Fourier spectrum of the observed object is attenuated more. In this chapter we have shown that even with a signal to noise ratio of 200 it is difficult to recover the higher Fourier frequency information in entirety. Therefore we need especially good sites for astronomical observations.

The technique we have discussed in this chapter is applicable only to long exposure images. If we are looking for changes in the object with time scales of few milliseconds then we necessarily have to go in for short exposure or speckle imaging. There are techniques like blind iterative deconvolution which restores images using a single

frame. In these techniques Fourier modulus error is an important constraint. Since the short atmosphere psf is not symmetric in the physical space the atmospheric phase corrupts the phase of the object. Restoration of these short exposure images introduces spurious phase information in the restored image. Instead of specklegrams if long exposure images are used, phase information is retained to a large extent to constrain the ambiguities of rotation and translation which one encounters with phase retrieval (Jefferies, & Christou 1993)

A stable sky for few seconds is a prerequisite to obtain maximum information from a long exposure image. We have seen that noise plays an important role in image restoration. Any attempt to remove noise tampers with the true object information since there is no specific frequency interval in which noise alone exists. Measurement noise effects on image restoration are quite important under low light level conditions (Roggemann, Welsh & Fugate 1997).

Artifacts get produced in the restored image when the signal to noise ratio is low. Each technique has got its own limitations when it comes to recovery of true object information from the blurred noisy image. The classical inverse filtering and the Wiener filtering are linear filtering methods. There are nonlinear image restoration algorithms 1) Maximum-likelihood estimation is a method where the object and image are treated as probability density functions and we try to estimate the most likely object to have resulted in the measured image. 2) Blind deconvolution algorithm is a constrained iterative method which results in joint estimation of the true object and the psf. 3) CLEAN algorithm - This iterative algorithm which uses successive subtraction of properly weighted and located dirty psf's located at the brightest point in the image. This process is completed until the residual image in the original array reaches the rms noise level of the data, 4) Maximum entropy algorithm - This method is based on maximizing a specialised measure of error based on the concept of entropy used in information theory. 5) Super resolution algorithms - Here the is is to obtain an accurate estimate of the object spectrum within the measured passband and to reconstruct the object's spectrum outside the passband.

Any linear processing method cannot generate nonzero values at unmeasured spatial

frequencies and cannot extrapolate into noise contaminated regions of the Fourier frequency plane. Here we do not attempt for information beyond the resolution limit of the telescope. We are trying to recover the information upto the diffraction limit of the telescope. If D is the diameter of the telescope then the spatial cut off frequency of the telescope is $f_c^{teles} = D/\lambda$. The Fried's parameter r_o characterising the atmospheric psf limits the cut off frequency to $f_c^{atm} = r_o/\lambda$. It is this information lying between the atmospheric cut off spatial frequency f_c^{atm} and the telescope cut off spatial frequency f_c^{teles} which we are trying to recover. We have tried to show that simple linear filtering methods with reasonable estimate of the blurring function and noise can restore images with information about the object lying between f_c^{atm} and f_c^{teles} . The restoration of comet images and the globular cluster images using linear filtering techniques shows the possibility of obtaining information beyond f_c^{atm} .

Fig (4.16) is the plot of amplitude of the Fourier spectrum at a spatial frequency as a function of the Fried's parameter. This is to highlight the problem of contrast reduction in the observed image with changing atmospheric conditions. We can see that as the Fried's parameter changes the strength of the higher spatial frequency falls at a faster rate than the the rate at which the lower frequency strength changes.

The main motivation of this work is towards understanding the linear image restoration methods. Iterative processing methods like maximum entropy method, blind iterative deconvolution etc., are computationally intensive procedures and the processing needs to be done offline. Our future plan is to try and implement the linear filtering method discussed in this chapter on the telescope to produce high resolution images online.

Optical disturbances like the photometric stability of the sky, scattered light from the atmosphere and the telescope, image motion, and size of the isoplanatic patch all play a crucial role in the resolution of the final image.

In Fig (4.16) we see that at smaller values of Fried's parameter the reduction of the value of the amplitude is more pronounced in the case of all the frequencies. As we go to higher values of r_o , we see that the attenuation of high frequency component is high

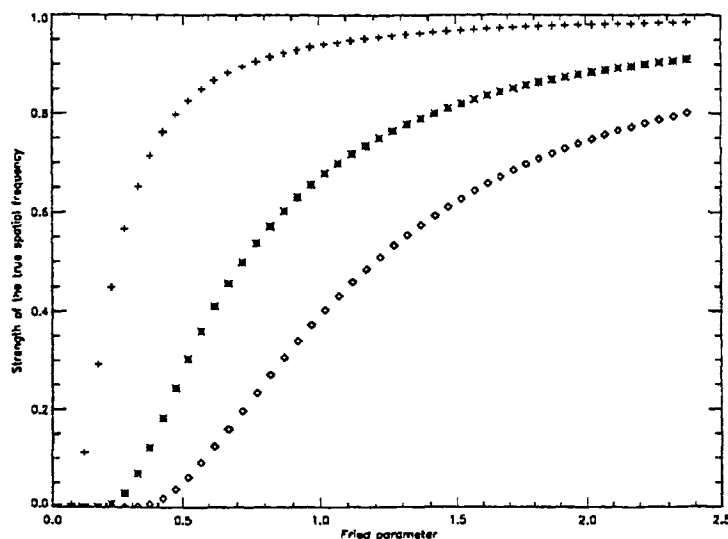


Figure 4.16: Plot of amplitude of the Fourier frequencies with changing Fried's parameter. + - low spatial frequency component, * - intermediate spatial frequency component, - High frequency component

compared to the low frequency component. As the value of the Fried's parameter r_0 becomes smaller then the value of the Fourier amplitude will reach the value of the noise at those frequencies.

CCD system noise level is photon-shot noise limited in the case of high light levels and at low light levels the CCD system is readout noise limited (Mackay 1986). Intrapixel nonuniformity has been largely ignored. Although CCD's are flat some of them are thin membranes suspended by their edges. They show surface nonuniformities of typically 70μ peak to peak. The electronic hardware systems driving the CCD themselves have significant effect on the data taken at a telescope. Ground loop problems between the dewar and the driver electronics, within the driver electronics or between the driver electronics and the computer system can cause interference with the readout electronics, giving rise to patterns that are synchronized with the line frequency. Electrical noise from motors, light dimmers, or computer parts can be picked up by the detector system. Electronic drift can cause background levels to change during the readout of one frame over a longer period. This problem can be overcome by reading more pixels in each row than are physically there. In this

process we get dark pixels at the end of each row of data which can be used to monitor variations of dark level and readout noise. It is very important that the astronomer is on the lookout for these problems since the above discussed problems can significantly contribute to the noise level in the data (Mackay 1986). Hence it is imperative that we model the noise in the data. In this chapter we have shown that a simple hypothesis of the ratio of the noise power spectrum to the signal power spectrum results in superlative results.

Apart from the availability of good observational site and good detector systems we need good computing facilities to support the observations. For implementing image restoration techniques we need fast computing machines. New techniques like phase diverse speckle restoration have been used to produce good quality images. This technique will be discussed in some detail in the next chapter. The requirements to use techniques like phase diverse speckle restoration are several workstations working in parallel over many weeks to produce 178 frames of high quality data (Lofdahl 1997). It is necessary to have image selection algorithms which would select the best images online. If we are looking for features which are undergoing changes every few seconds then the frames have to be acquired at those speeds.

Chapter 5

Application of High Resolution Imaging : Dynamics of G band Bright Points I [†]

5.1 Introduction

The horizontal and vertical motions associated with the supergranulation concentrate the magnetic fields at the cell boundaries. The photospheric magnetic fields extend upto the chromosphere. Together the photospheric and chromospheric magnetic fields are responsible for the excess heating which manifests itself as a brightening in different photospheric lines, center of $H\alpha$ etc., This is seen to happen in super granulation network. Since the network is bright, it is thought that the magnetic field should be responsible for the brightening.

The bright point images imply a close correlation between the bright point and the magnetic field. The observed correlation is so close that the photograph of the bright

[†] Van Ballegoijen, A., Nisenson, P., Noyes, R.W., Stein, R.F., Nordlund, A., Krishnakumar, V., 1998, Ap.J.,(in press)

points maybe essentially regarded as as a map of the magnitude of the magnetic field or more precisely the line of sight component of the magnetic field.

An important and interesting discovery has been the intense nature of the quiet region magnetic fields in the photosphere (Stenflo and Harvey 1985, Mehlretter 1974, Muller 1985, Muller and Keil 1983). It has been found that both in the quiet and active regions, the magnetic field present is not a continuum, but is composed of widely separated, intense magnetic fields. The fields within the individual magnetic elements are 1000 to 2000 G. Their sizes range from 500 km downward. The individual flux tubes are swept into the intergranular regions by the granulation. The other ways in which the magnetic fields could be present is, disordered field carrying no net flux (Stenflo 1982) and present at scales down below the present resolution limit of the existing telescopes.

The most important aspect is the discrete nature of the solar magnetic field. In the photosphere and chromosphere two different regimes coexist. One is the magnetic elements, dominated by their magnetic field and the other is the virtually field free region surrounding these magnetic elements. The ratio of the kinetic pressure to the magnetic field pressure is,

$$\beta = \frac{8\pi P}{B^2} \quad (5.1)$$

where P is the gas pressure and B is the magnetic field. In the magnetic fields $\beta \lesssim 1$ and $\beta \gtrsim 1$ in the field free region.

The gas pressure drops exponentially with height but the magnetic pressure falls off more slowly. Hence β decreases with height. The magnetic fields fan out as we go higher up in the solar atmosphere and the individual tubes merge to form a "canopy" (Giovanelli, 1980). Hence to study the dynamics of these small scale structures we need to observe these structures when they are confined to smaller spatial scales. Subarcsecond features seen in white light as well as in photospheric and chromospheric absorption lines are called bright points. They occur at sites of high magnetic flux concentration in the photosphere. Magnetic flux concentration is necessary but not sufficient to produce these bright points.

High quality images hinted at the existence of small scale brightenings in the interior of the super granular cells (Dunn and Zirker 1972). Recent G band images opened a new window to track the footpoints of small scale chromospheric brightenings. However an unambiguous identification between the G band bright point and the Ca II K bright point is not yet done.

The bright points are associated with regions of strong magnetic field and correspond to magnetic flux tubes that stand vertically in the solar atmosphere (Chapman and Sheeley 1968, Title et.al 1987)

Simultaneous G band and SOUP magnetogram time series analyses have verified the fact that the photospheric bright points occur preferentially on the periphery of strong field concentrations (Yi and Engvold 1993).

The G band images are presumably the foot points of the magnetic flux tubes which extend all the way up into the chromosphere. So we conclude that the G band images are reliable proxies for some fraction of the photospheric magnetic features but the quantitative estimate of this fraction is yet to be determined.

These bright points are seen when imaging through continuum, line center and molecular band. Berger et. al (1995) have demonstrated that magnetic elements are seen with particularly high contrast in filtergrams taken with 4305\AA molecular band-head of CH. The required spatial resolution for successful imaging of the magnetic element bright point is $0.''4$.

It is necessary to observe and understand the features on the sun at all scales in order to understand the basic physical processes of magneto-convection, the dynamo processes and the formation and evolution of magnetic field structure. The spatial and temporal features on the sun extends over huge scales. In case of simulations we need to introduce boundaries and can include only certain scales. To give any sensible input for these simulations and extend our models we need input from observations at different scales. It is the smaller spatial scales which pose a challenge. And, it is the features at small scales which play a very important role in the activity on the sun.

The chromospheric temperatures in excess of the photospheric temperature of roughly 5500K in the chromosphere can be explained only by non radiative heating processes. The study of the dynamics of the magnetic bright points helps us to understand the mechanisms through which energy can be imparted for heating the chromosphere (Van Ballegooijen 1998). From the high resolution images of the magnetic bright points we try to infer their velocities, their intensities and dependence of these physical quantities on their life times.

5.2 Observation of Photospheric Bright Points

Chapman and Sheeley in 1968 and Sheeley in 1969 established that are strong magnetic field concentrations in the form of a bright network in the photosphere apart from the strong magnetic fields in the sunspot. These bright points were seen when observed in weak line cores and the CN bandhead at 3883\AA . These features were seen to coincide but had finer spatial scale when compared with the Ca II K line network in the chromosphere. These were spectroheliographic measurements. It needs scanning periods of the order of few seconds to build up these images. The atmospheric seeing changes occur typically on timescales of 10 to 100 ms. This causes varying distortions across a single image.

To improve on this, Dunn and Zirker in 1973 developed single exposure filtergrams taken in the wings of the $H\alpha$ line.

In 1974 Mehlretter observed bright points in the far wings of the Ca II K line. Their size was estimated to be around 200 km.

Simon and Zirker in 1974 found good spatial correlation between the photospheric bright points and the magnetic field structures observed simultaneously using magnetograms.

Berger et al. 1995, studied the bright points in the plage magnetic fields and showed that the size range of the bright points in plage is larger than those formed in the network. But the majority of the flux elements were found to be circular and around

200 km in diameter. It was also shown that the "*filigree*" seen at high resolution were actually made up of strings of smaller bright points.

Novel spectroscopic techniques were developed to measure the magnetic field strength outside the sunspot. In 1972, Howard and Stenflo and later Frazier and Stenflo in 1972 and Stenflo in 1973 measured the field strength using the magnetic line ratio technique. Also measurement of magnetic fields using the fully Zeeman split infrared lines was used by Harvey and Hall in 1975 and Zayer, Solanki, and Stenflo in 1989. In 1977, Title and Tarbell used Fourier transform technique to estimate the average magnetic field strength.

In 1992, Keller used high resolution filtergrams to compute magnetic line ratios and estimated field strengths of the order of 1000 G at the formation level of Fe I 5250Å°. Rabin in 1992, used a near infrared imaging magnetograph for direct measurement of field strength in the Zeeman dominated Fe I 15650Å° line. Rabin measures field strengths varying from 1000 to 1700G.

Solanki in 1993 review on the small scale features on the sun reviews the attempts to measure field strengths of these small scale features and concludes that the field strengths must be around 1500G to 1700G.

5.3 Theoretical Modelling of Flux Tubes : A Brief Summary

Spectroscopic observations indicated the presence of gaps in the spectral lines of Zeeman sensitive transitions. These observations were quantified by using Unno-Rachovsky line profile synthesis. The gaps were line splittings of the Zeeman sensitive transitions and implied a field strength of around 1000 G.

Using the observational data theoretical models were developed to explain the solar magnetic elements. Spruit in 1974 suggested a thin flux tube model, later refined by Spruit and Zweibel in 1979. This is referred to as the standard theoretical model of

small scale magnetic flux in the solar photosphere.

This model for field intensification suggest that these magnetic structures are held together by a balance of inward force caused due to excessive gas pressure outside the structure and the outward pressure of the field within the flux tube.

The model is characterised by this balance between magnetic pressure and static gas pressure across a well defined boundary region of the flux tube. This static balance results in significant radial expansion of the tube with increasing height in a hydrostatic atmosphere.

Simulations of the magnetic flux elements in the presence of granular convective flows have predicted to induce oscillations of the flux tube. Characteristic time scales of these periods have been found to be of about 5 minutes. Ryutova, Kaisig and Tajima modeled the interaction of a wavetrain with a flux tube and showed that it could lead to fragmentation of the tube.

Periodic shaking or buffeting of these flux tubes could generate magneto hydrodynamic waves which propagate along the flux tubes and dissipate energy in the chromosphere and/or corona. If we make an assumption that the G band bright points represent flux tubes then there should exist a relationship between the transverse motions of and the brightening of these bright points.

Our main motivation is to see whether there exists any relationship between the rms fluctuations in velocity and the mean brightness of the magnetic bright points and also to look for possible dependence of other physical parameters like the average velocity, average intensity and rms intensity on one another.

5.4 Observational details

The data used is a part of the 70 min time series of cospatial G band 4305\AA . and 4686\AA filtergrams obtained with the 50 cm Swedish Vacuum Solar Telescope on the island of LaPalma in Spain (Berger et.al 1997). The field of view is $29'' \times 70''$ near disk center. This consists of both an enhanced network region and an non-magnetic

quiet region of granulation. The mean time between the frames is 23.5s. The images have been processed using partitioned Phase-Diverse Speckle restoration. Each image is obtained by using 3 realizations of the atmospheric turbulence obtained in sequence. The final spatial resolution obtained is 0.2" (Lofdahl et.al 1997). This high spatial resolution helps us to monitor the individual bright point evolution and the high temporal resolution helps us to track the bright point and estimate their life times. Fig (5.1) shows an image of the sun observed in G band.

5.5 Phase Diverse Speckle Observations

The performance of any optical instrument is characterised by its transfer function. The observable is the function called the point spread function which is the modulus squared of the coherent transfer function. Let $c(r)$ be the coherent transfer function.

$$p(r) = |c(r)|^2 \quad (5.2)$$

where r represents the two dimensional coordinates x and y .

Transfer function in the Fourier domain is,

$$C(f) = A(f)e^{i\theta(f)} \quad (5.3)$$

where $\theta(f)$ is the aberrated wavefront across the aperture. The problem of phase retrieval is to estimate $\theta(f)$ using the observed $P(f)$. A suitable set of polynomial expansion is used for $\theta(f)$.

$$\theta(f) = \sum m_k \phi_k(f) \quad (5.4)$$

The mean square error estimate is written in metric form and we search for the coefficients m_k of this polynomial which minimises the metric.

Detected Image is,

$$z_1(r) = [o(r) * p_1(r)] + n(r) \quad (5.5)$$

where,

$$p_1(r) = |c_1(r)|^2 \quad (5.6)$$

Another image is recorded with a known amount of phase added to the original image,

$$p_2(r) = |c_2(r)|^2 \quad (5.7)$$

$$C_2(f) = A(f)e^{i\theta(f)+i\phi(f)} \quad (5.8)$$

$\phi(f)$ is called Phase Diversity.

$$z_2(r) = [o(r) * p_2(r)] + n(r) \quad (5.9)$$

The error metric can now be written as,

$$E = \int |z_1 - o(r) * p_1(r)|^2 dr + \int |z_2 - o(r) * p_2(r)|^2 dr \quad (5.10)$$

We need to minimise this integral. We get the following result for the object estimate,

$$O(f) = \frac{z_1 P_1^* + z_2 P_2^*}{P_1^2 + P_2^2} \quad (5.11)$$

For more details on the observations and processing of these images refer Lofdahl et al.(1997). The data used here has been obtained on 1995 October 5 between 10:57 and 12:08 UT. Observations has been carried out at two wavelengths. The imaging has been done using a $12A^\circ$ bandpass interference filter with a central wavelength of $4305A_\circ$, this is the G band image. The other image has been obtained using a $54A^\circ$ bandpass filter with a central wavelength of $4686A^\circ$. Frame selection has been done and only the best out of every 3 frames have been chosen. The frame selection has been done once in every 20 seconds. Both the CCD cameras recorded two images, one in focus and the other with a known amount of defocus. The images are then corrected for atmospheric seeing using the Partitioned Phase Diverse Speckle Restoration technique. The images have been coaligned using a technique called destretching. In a set of frames the best frame is chosen. The rest of the frames are coaligned with respect to this frames so as to maximise the cross correlation between them and the reference frame. This technique is called as Destretching.

The total data set consists of a time series of 180 images with very high spatial resolution covering a period of about 70 minutes. The mean time between the frames is around 23.5 seconds and the plate scale in the image is 0.083 arcsec/pixel.

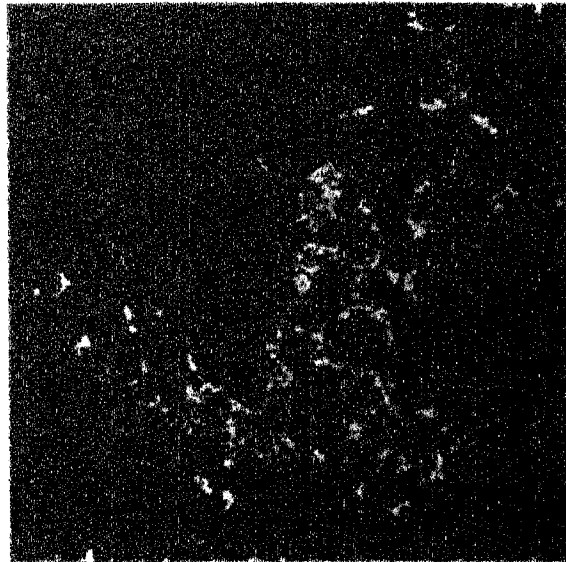


Figure 5.1 *High resolution image showing G band bright points. The continuum image is subtracted from the narrow band image to enhance the contrast of the bright points*

The bright points are seen at high contrast when imaged in G band. They are seen at reduced contrast at 4686.4\AA because continuum and some absorption lines are contained in this wavelength range. Simultaneous imaging at these two prescribed wavelengths gives information about the location of the bright points because the granulation shows up with almost equal contrast in both these images.

Subtraction of images observed at these two wavelengths produces a difference image in which the bright points are seen at even higher contrast. This image is now used to study the dynamics of the bright points.

5.6 Tracking of Bright Points

Berger et al. identified the bright points using a thresholding on these difference images. They define the magnetic region in the field of view as that region in the image which is covered by bright points at any point of time during the entire observational sequence. The image is subdivided into smaller sub fields and velocities of bright

points measured using an object tracking technique. The histogram of the velocities of the bright points have a broad velocity distribution and peaks at around 0.1 km/s. The mean velocity is around 0.815 km/s. It was also observed that the bright points continually split up and merge. Few bright points could be followed through the entire sequence.

The difference image is constructed the following way,

$$I_{magn}(x, y) = I_{4305}(x, y) - I_{4686}(x, y) \quad (5.12)$$

x and y are the horizontal coordinates on the sun. The images are normalized with respect to the mean intensities in the non-magnetic region in the frame.

The difficulty faced in tracking these bright points is because of the packing of these bright points close to each other forming complex shapes and hence their positions are not well defined. The G band bright points continually split and merge and hence causes sudden changes in their position. If high resolution is not there, then the splitting/merging would not have been observed and the sudden shift of the photocenter of the complexes of bright points would have been then interpreted as real motions of the complexes.

To overcome this problem we use an object tracking method where finite sized corks are used as tracers of these bright points. The corks are circular finite sized disks which move around in the photospheric plane but do not overlap each other. These corks are allowed to flow with the advected flow produced by an artificial flow field which drives the corks to the brightest points on the image. The artificial flow is created by using the gradient of the difference image.

In this present study 1400 corks have been used. The radii of the cork $r_o=60$ km. This is equal to the pixel size in the data set. The positions of the corks are advanced with a time step equal to one half of the average time between the frames in the movie. The correction for the cork overlap is done iteratively. We first check for pairs of corks whose separation is less than $2r_o$. If we find the separation between the corks less than $2r_o$, then those corks are moved apart in opposite directions along their line of separation until the corks just touch each other. This procedure is repeated until

there are no overlapping corks.

The frames used are averaged over 3 frames. A mask image is produced. These mask images are produced by smoothing the I_{magn} images in space and time by a running average over 5 frames and applying a 2σ threshold. These masks gives a overall idea where the bright points are located. The initial positions of the corks are chosen at random within the first mask image. The intensity of the bright points varies with time. Apart from the splitting and merging of the bright points some of the bright points fade away. The corks associated with these have nowhere to go and hence after every fifth frame we remove those corks which fall out of the magnetic mask and replace them at random positions within the mask. We find that typically 5% of the 1400 corks are replaced every fifth frame and the total number of corks present over the entire time interval is 3827. Hence the corks will have lifetimes which are in multiple of 5 frames. In this way we measure the position and velocity of the bright point through representative corks as a function of time.

5.7 Average Velocity of the Bright Points

The random motions of the photospheric flux tubes could produce magneto hydrodynamic waves and other disturbances into the solar atmosphere and heat the upper atmospheres. Models of wave generation by Choudhri, Dikpati and Banerjee 1993, predict that short period motions are much more effective in generating waves than long period motions. We determine the autocorrelation function which describes how the velocity of the bright points varies with time.

The autocorrelation of velocity $v_{x,k,n}$ over a time delay $t_m = m\delta t$ is given by,

$$C_{x,k,n} = \frac{1}{N_k - m} \sum v_{x,k,n} v_{x,k,n+m} \quad (5.13)$$

and similarly in the y direction,

$$C_{y,k,n} = \frac{1}{N_k - m} \sum v_{y,k,n} v_{y,k,n+m} \quad (5.14)$$

where k is the cork index and n is the time index. By averaging these functions for all corks with lifetimes $N_k > m$, we obtain the mean autocorrelations $C_{x,m}$ and $C_{y,m}$.

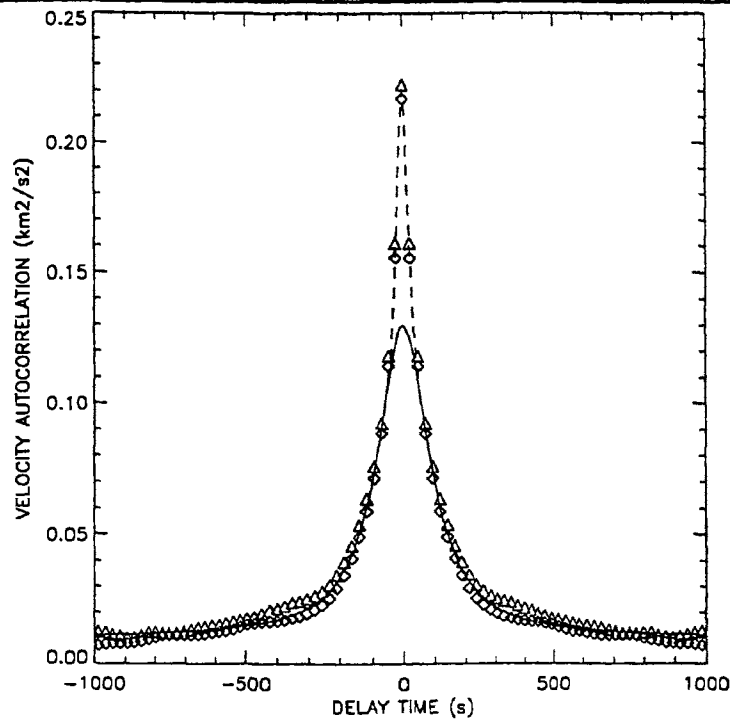


Figure 5.2: *Plot of autocorrelation of the velocity of bright points.*

Fig (5.2) is the mean autocorrelation as a function of delay time t_m for $t_m \leq 1000s$. The autocorrelation function is seen to decrease monotonically with time. There seems to be no evidence for any specific periodicities in the bright point motion. Initial fall in the autocorrelation could be because of the corks taken a couple of frames before they can organise themselves and follow the advected flow calculated using the gradient in intensity of the difference image. The autocorrelation decreases rather slowly thereafter. This describes random motions with correlation time $\tau_c=100$ seconds.

5.8 Motion of Bright Points and Heating of the Solar Atmosphere

Ballegooijen et al, 1998 have shown that from the computed autocorrelation function one show that the estimated acoustic cut off frequency from the power spectrum is less than the photospheric acoustic cutoff frequency. Therefore it is doubtful

whether the observed motions are very effective in generating waves to heat the solar atmosphere.

Absence of periodicities in cork motions does not directly imply absence of periodicities in actual motion of bright points. Further, as shown by Auffret, Priest et al. a few bright points seem to move exceptionally fast and are capable of generating sufficient mechanical energy to heat the upper atmosphere. So, it is necessary to study the individual bright points. Here we did not distinguish between the fast moving bright points and the slow moving bright points. Visual inspection of these images show that the bright points in the magnetic region seem to be more constrained in their motion because of the clustering of bright points. Since models predict a direct relationship between the velocity of transverse motion of the bright point and its brightness, in the next chapter we study the dynamics of isolated bright points and try to look for a possible relationship between their velocities and their intrinsic brightness variations.

Chapter 6

Application of High Resolution Imaging : Dynamics of G band Bright Points - II †

6.1 Introduction

In the previous chapter, it was seen that a statistical treatment of all the bright points yielded no special periodicities, but showed evidence for random motions of 100 seconds timescales. In this chapter our main motivation is to see whether there exists any relationship between the rms fluctuations in velocity and the mean brightness of the magnetic bright points and also to look for possible dependence of other physical parameters like the average velocity, average intensity and rms intensity on one another. A study of the dynamics of the magnetic bright points will help us to identify the mechanisms through which energy is imparted for heating the chromosphere. From the high resolution images of the magnetic bright points we try to infer their velocities, their intensities and dependence of these physical quantities

† Krishnakumar V., Venkatakrishnan P., 1998, Sol. Phys (submitted)

on their life times.

In section 2 we discuss the methodology followed by us in tracking the bright points. In section 3 we discuss the distribution in the lifetimes of the bright points which we have chosen for study. In section 4 we look at the velocity and brightness distributions. In section 5 we examine the relationship between motions and brightness variations, while in section 6 we discuss the implications of such relationships, if any, for wave heating of the atmosphere within the flux-tubes.

We see in the images that several bright points are clustered together while others are isolated away from this magnetically enhanced network region. In the magnetically enhanced region, it is difficult to isolate a single bright point and track it since it undergoes merging with the neighboring bright points and loses its identity. At the resolution limit of the frames, it becomes difficult to identify the bright points once they merge with the neighboring bright points.

6.2 Methodology

The frames were run in sequence and the isolated bright points were selected visually. Centered on the isolated bright point, the image was cut into a smaller array. The same region was cut from the entire sequence. The bright point was tracked manually in the sequence of frames. The positions of the bright points were stored. The rate of change in their positions gives us the velocity.

When the lifetime of the bright point is measured, the measured lifetime might be different from the true lifetime of these magnetic element bright points due to the following reasons. The cluster of these bright points might live longer than the individual bright point or the individual bright points may just drift away from the cluster and dissolve the cluster. Another possibility is that the individual elements may break up and form new ones continuously without producing any noticeable changes in the overlaying magnetic pattern. Hence we identify and track those bright points which are away from the magnetically enhanced region. The lifetime in our

case is the time for which the bright point can be tracked without any ambiguity. We do not consider those bright points which show up right from the first frame, since their past history is not known. The bright points are tracked through the sequence and when a bright point disappears we switch over to another isolated bright point. In event of switching over to another bright point which has just started to brighten and show up in the frames we would not have tracked the bright point in its earlier phase since we were tracking another bright point. This could lead to an underestimation of the lifetime. Since we are interested, not in their absolute lifetimes, but seek a relationship between the lifetime and average velocity and distribution of lifetime, we define a cutoff in the intensity of the bright point and estimate the time for which the bright point had an intensity above the cutoff value. By defining a cutoff and looking for lifetime distribution, we underestimate the lifetime but the shape of the distribution will not change.

Totally we identified 56 bright points and estimated their average intensity, rms intensity, average velocity, rms velocity and lifetime. From this we estimate the power spectrum of velocity and intensity and look for dependence of intensity changes with changes in velocity.

6.3 Lifetime of the bright points

In a recent paper, Berger *et al.* (1997) estimate the lifetime based on the same data. They define the lifetime as the time span over which a coherent group of magnetic flux elements can be tracked before they disappear or merge with existing flux. They measure a lifetime ranging from 2 min to some bright points living through the entire sequence. The average lifetime is 9.33 min. The average lifetime estimated by Berger *et al.* is higher than the lifetime estimated by us since they consider the bright points in the magnetically enhanced region. We are interested in the isolated bright points since they are more dynamic in nature than the one in clusters.

We classify the bright points based on their lifetimes. The classification is done

based on the number of bright points available for good statistics. The bright points are classified into those which lived for less than or equal to 200 s, those which have lifetimes between 200 s and 400 s and those bright points which lived for 400 s and more. Defining the lifetime as the time span over which the brightness of the point exceeds a threshold value, we see that the histogram of the lifetime of the bright point peaks at around 50 s to 100 s. There are also bright points whose lifetime spans the entire sequence of frames we have used.

To look for relationships between the various estimated physical parameters we plot the scatter plots between various physical quantities estimated from the data. We also plot the power spectrum of intensity and velocity.

6.4 The Velocity and Intensity Distributions

In this section we look at the velocities and intensities of the bright points. To normalize the velocity and intensity we do the following. A single bright point is tracked say for n frames. We now have their displacements. It is straightforward to estimate their velocity once the displacement with time is known. Let $s(t)$ be the displacement as a function of time. Now velocity $v(t)$ is $\frac{ds(t)}{dt}$. We are interested only in the fluctuating part of the power spectrum, hence we do the following. Let the mean of velocity of a bright point tracked for n frames be $\langle v(t) \rangle$. The mean is subtracted from the velocity $v(t)$. We find the standard deviation of $v_i(t) = v(t) - \langle v(t) \rangle$. This is given as,

$$\sigma = \left(\sum \frac{[v_i(t)]^2}{n} \right)^{1/2} \quad (6.1)$$

where n_1 and n_2 are the first and last frames in the sequence of frames through which the event of brightening was seen. The normalized velocity profile $v_n(t)$ is now given as,

$$v_n(t) = \frac{v_i(t)}{\sigma} \quad (6.2)$$

This $v_n(t)$ is the velocity profile of the magnetic element bright point which is used in further analysis.

To remove atmospheric and instrumental effects and to improve the contrast of the bright points the following was done. We have images obtained in both narrow band I_{nb} and broad band I_{bb} . The broad band image is first subtracted from the narrow band image. This helps in the removal of the continuum in the narrow band image. The frame is then divided by the continuum image to remove atmospheric and instrument effects.

$$I_{rel} = \frac{I_{nn} - I_{bb}}{I_{bb}} \quad (6.3)$$

These frames are now used to track the bright points and their intensities are estimated.

The bright points whose velocities were measured are again tracked and their intensities $I_i(t)$ are determined as a function of time, where i is the index for the frames. $I_i(t)$ is normalized using the same procedure using which we normalized the velocity.

$$I_n(t) = \frac{I_i(t)}{\sigma} \quad (6.4)$$

σ is the standard deviation in the measurement of intensity of the bright point.

This $I_n(t)$ is the relative intensity profile of the magnetic element bright point which is used in further analysis.

We tracked these bright points and found that some of the bright points were more dynamic and some were stationary. Fig (6.1) is the track of some of the bright points. This is to illustrate the motion of these bright points. Tracking was carried out repeatedly to minimise errors inherent in manual tracking.

Fig (6.2a) is the histogram of average intensity. The average relative intensity has a peak in the histogram at around 0.21 to 0.25. Fig (6.2d) is the histogram of the rms of relative intensity. The rms of the relative intensity histogram has a peak at around 0.1. The width in the distribution of rms intensity is smaller than the width in the distribution of average intensity.

Fig (6.2b) is the histogram of average velocity. The peak of this histogram is at around 1.0 km/s. Fig (6.2c) is the histogram of the rms velocity. This has a peak at around 1.1 to 1.2 km/s. The width in the distribution of average velocity is higher

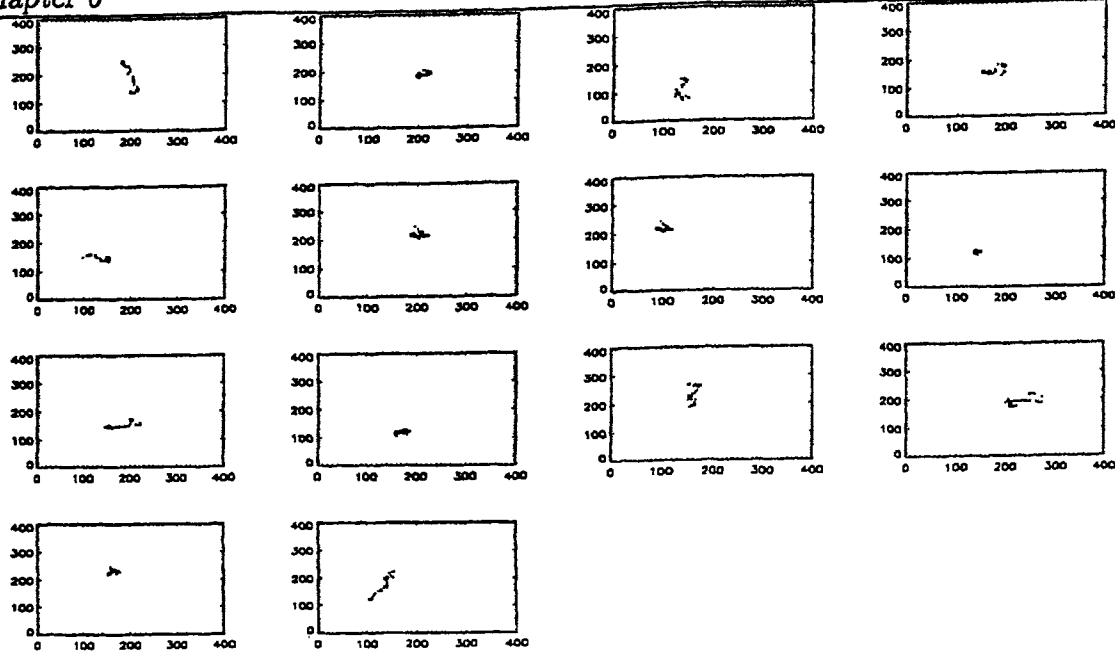


Figure 6.1: Tracks of a few bright points. This is to illustrate the dynamics of these bright points. Some of the bright points show a larger displacement than others. Every tick on both the directions corresponds to 17.5 km on the sun. Each frame is 7000 km X 7000 km on the sun.

than the width in the distribution of rms velocity. There are also few bright points which have velocities as large as 4.0 km/s and few bright points which have a rms velocity higher than 3.0 km/s.

The bright points which have rms velocities equal to 0.0 km/s have rms intensities and average intensities comparable to the intensities of the bright points which have rms velocities and average velocities close to the peak velocity value in the average velocity and rms velocity histograms.

6.5 Transverse Motions and Bright Point Intensities

We assume that the magnetic flux tubes are anchored at the base of the convection zone. When a force is imparted at the base of this magnetic flux tube the disturbance

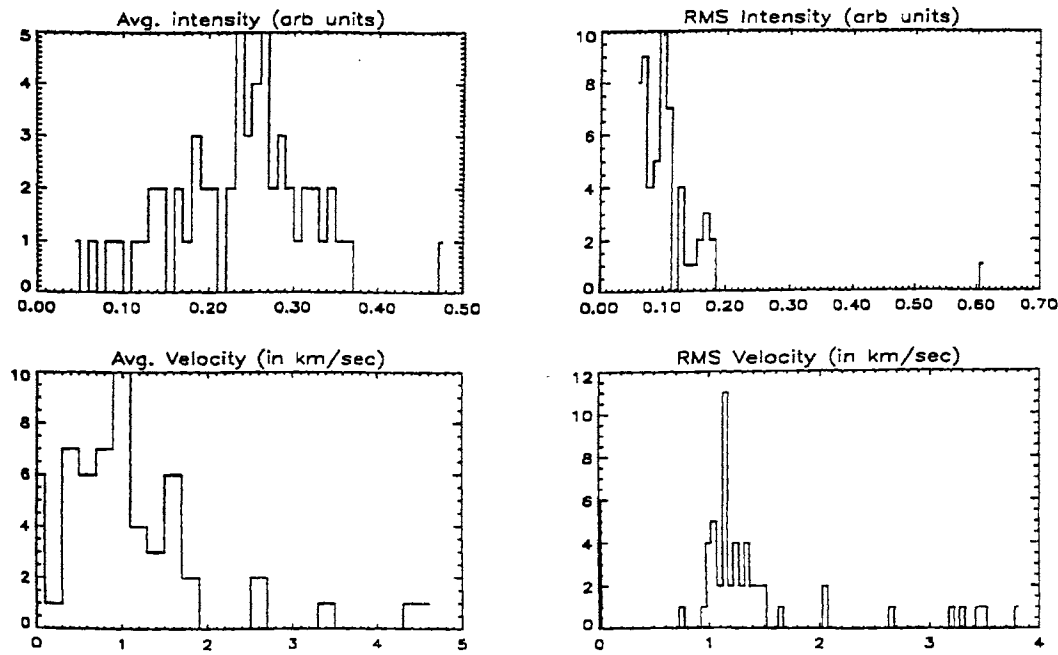


Figure 6.2: 6.2a is the histogram of the average intensity. 6.2b is the histogram of average velocity. 6.2c is the histogram of rms intensity. 6.2d is the histogram of rms velocity.

propagates to the top with the amplitude of motion increasing with height. This causes the observed transverse motion of the magnetic element. The brightening seen in the magnetic elements could be due to the gas dynamics within the flux tube, heating of which could be caused by a different mechanism altogether. This suspicion is further strengthened by the fact we do observe a couple of bright points which are found to have velocities equal to 0.0 km/s but show relative brightening equal to or even higher than those moving with higher average and rms velocity.

We will discuss the scatter plots between different physical quantities of the magnetic element bright points. The magnetic elements bright point is classified based on the timescale for which the magnetic element is visible in the frame.

Let us first consider those bright points which lived for 200 seconds or less. The scatter plot of average velocity versus the rms intensity shows a clustering of the data points close to an average velocity of 0.0. Also the scatter plot of velocity and rms intensity shows a clustering of data points. The scatter plots of average velocity

with average intensity, between rms velocity and average intensity all show clustering of data points. Fig (6.3) is the scatter plot between the various estimated physical quantities. But we do not have enough data points to comment on this clustering of data points.

The lifetimes of these bright points have a spread ranging from 115 s to 188 s. But the lifetimes do not seem to have any dependence on the physical parameters of the bright point. For those bright points whose lifetime varies between 200 s to 400 s, the statistics are better since we have 18 bright points in this category. The scatter plot between average velocity and rms intensity shows a downward trend. ie., for higher average velocity the rms intensity is less.

We look at the power spectrum of the velocities and intensities to verify whether there exists any relationship between the transverse velocity and the intensity of these bright points. We classify the 56 bright points under study based on their lifetimes. The average power spectrum of the bright points is obtained. For the sake of clarity we will use the following notation for the bright points which have now been grouped based on their lifetimes. The bright points with lifetime less than 200 s, between 200 s and 400 s and more than 400 s will be denoted as b_{200} , $b_{200,400}$ and b_{400} respectively.

The average intensity, rms intensity, average velocity and rms velocity of the bright points are tabulated. For b_{200} bright points the estimated values of the various physical quantities are tabulated in Table 6.1. We can see that there are quite a few bright points which have zero average velocity zero rms velocity but show intensity fluctuations. Similarly in Table 6.2 is tabulated the rms intensity, rms velocity, average intensity, and average velocity for the $b_{200,400}$ bright points. We have another bright point in this category which has a zero average and rms velocity but has a non zero average intensity and rms intensity. In the case of b_{400} bright points we do not find any such examples. But we do find in this category of bright points a bright point which has the highest rms intensity value for which the corresponding rms and average velocity is the lowest. For b_{400} bright points the various estimated quantities are tabulated in Table 6.3. In these set of bright points we do not find

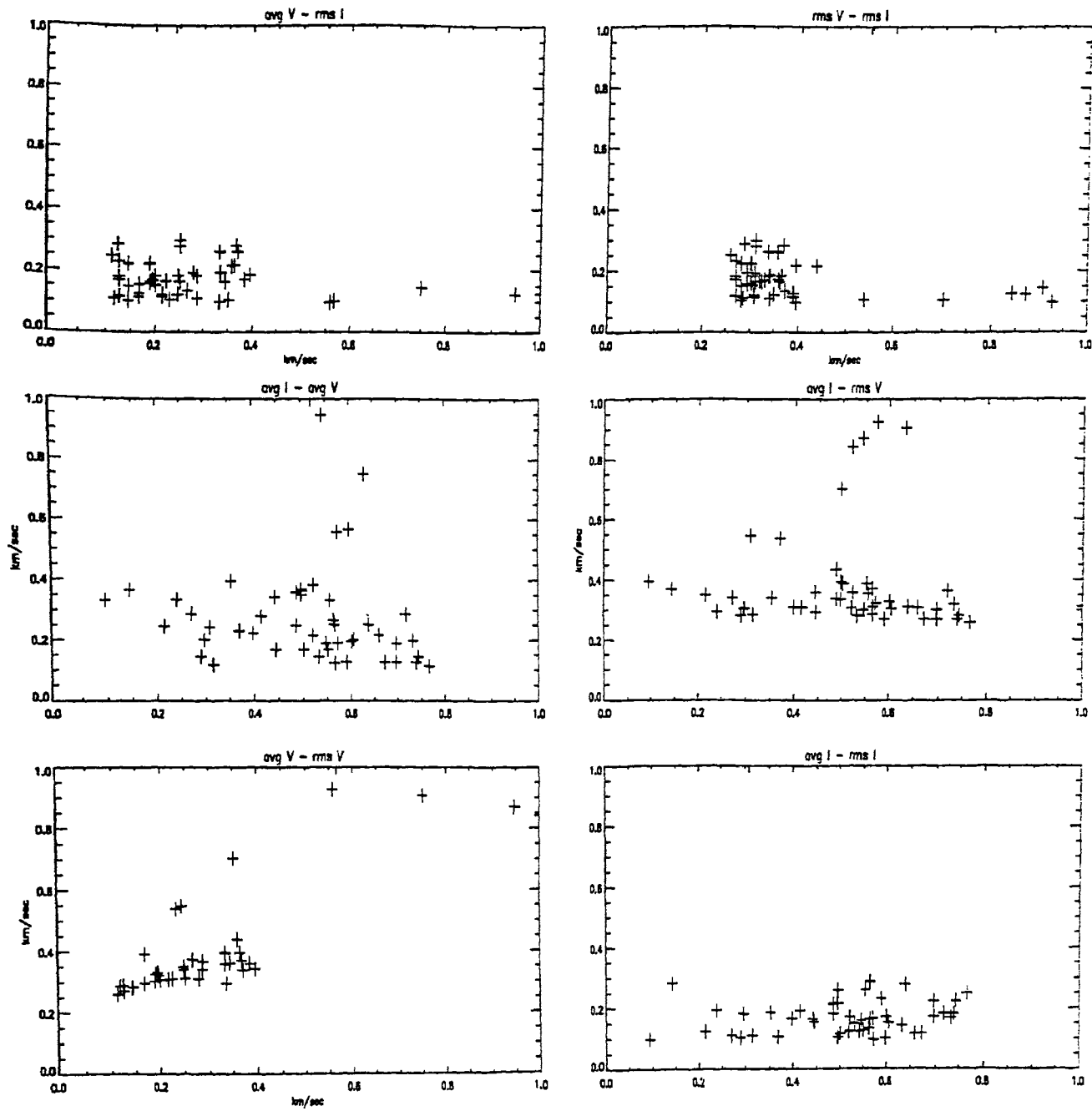


Figure 6.3: In the title A-B, 'A' refers to abscissae and 'B' refers to the ordinate. The rms intensities and average intensities are relative intensities and hence no units are assigned to them. Units for relative and rms velocities are in km/sec.

any stationary bright points.

Let us now consider the average power spectrum of both intensity and velocity of the bright points b_{200} . Fig (6.4) is the average velocity power spectrum and Fig (6.5) is the average intensity power spectrum. To bring out the high frequency features in the power spectrum we remove the zero frequency component of the power spectrum by subtracting the mean from the power spectrum.

In Fig (6.4), the first panel is the velocity power spectrum of bright points b_{200} , second panel for $b_{200,400}$ and third panel for the bright points b_{400} . b_{200} bright points can be tracked for a maximum of 7 frames. We see that the power spectrum of these b_{200} bright points does not decrease as we go to higher frequencies. In the case of these bright points which are bright for a short period of time we do not have enough time resolution in their measurements. b_{200} 's power spectrum is seen to be a constant at higher frequencies. If these magnetic elements undergo brightness variations within the timescale of each observation then we have undersampled data. Undersampling of data is analogous to time averaging. The peaks if any at higher frequencies are smoothed and show a constant power spectrum.

In the case of $b_{200,400}$ bright points the time resolution of the data is better than that of b_{200} bright points. We see some indications for the existence of peaks in their power spectrum. At higher frequencies we see smoothing of the power spectrum. In the third panel in Fig (6.4) is the power spectrum of the b_{400} bright points. Here peaks are seen clearly.

For the $b_{200,400}$ bright points the periods corresponding to the peaks seen in panel 2 of Fig (6.4) and panel 2 in Fig (6.5) are tabulated in Table (6.4). In Table (6.5) is tabulated the estimated periods corresponding to the peaks in the velocity and intensity power spectrum in panel 2 in Fig (6.4) and Fig (6.5). In case of bright points $b_{200,400}$ the velocity power spectrum has two peaks which corresponds to time periods of 143 s and 56 s. The corresponding intensity power spectrum has a single peak at a time period which corresponds to 286 s. The bright point b_{400} has a velocity power spectrum with peaks corresponding to time periods of 500 s, 200 s,

118 s and 83 s.

In Fig (6.5), first, second and third panel are the intensity power spectrum of b_{200} , $b_{200,400}$ and b_{400} respectively. Here again the b_{200} bright points are short lived and with the available data we do not have enough time resolution to pick up periods if any. Similar to the velocity power spectrum we find the intensity power spectrum at higher frequencies a constant. The $b_{200,400}$ bright point's intensity power spectrum indicates the presence of few peaks at the low frequency end of the power spectrum. Peaks are seen in the case of b_{400} bright points.

For the sake of comparison we plot the intensity power spectrum and the velocity power spectrum in same scale. Even though we see indications of peaks in the velocity power spectrum the power is less. The velocity power spectrum also suggests the existence of a band of periods whereas the intensity power spectrum has periods confined to a smaller band.

6.6 Discussion and Conclusion

As mentioned in the introduction, a possible scenario for heating the chromosphere is to generate kink waves at the photosphere (by the transverse shaking of magnetic flux tubes), convert these waves into longitudinal waves by non-linear effects (Venkatakrisnan, 1984; Ulmschneider, Zahringer, and Musielak, 1991) and finally dissipate these waves into shocks at chromospheric heights. The G-band bright points provide the means of observing the transverse motions of flux-tubes and it is of great interest to see whether the onset of wave heating occurs right at the level of formation of the G-band. To this end, a search for correlations between the average brightness of the bright points with their rms transverse velocity (a measure of amplitude of transverse waves) showed no obvious trend in the scatter plots of average intensity versus rms velocity (Fig (6.3)). The absence of any relation is reinforced in histograms of Fig (6.2), which show a much lower peak for the brightness distribution, thereby indicating a broader distribution. In other words, the flux-tube brightness seems to be independent of the transverse velocity amplitude. Berger

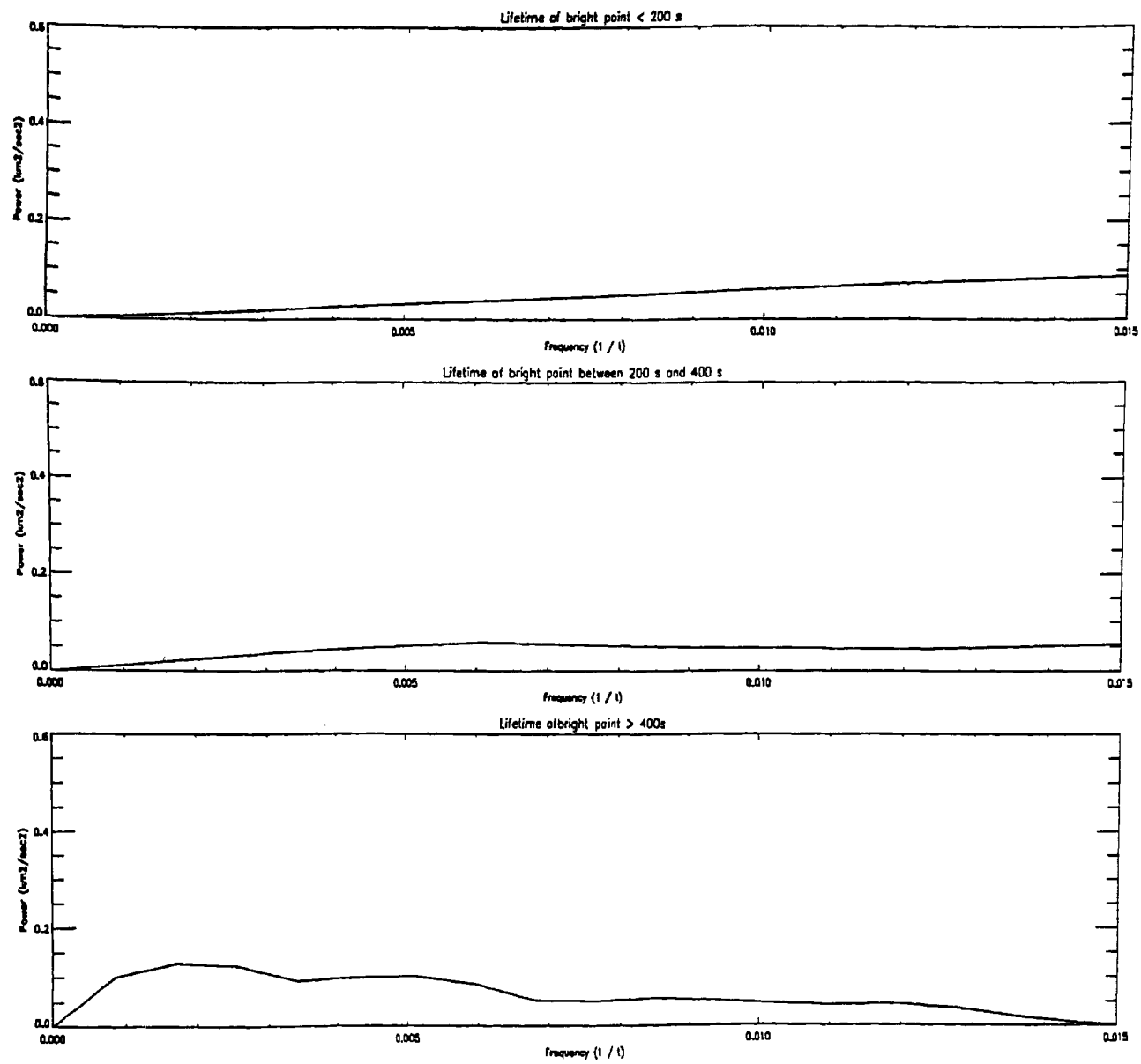


Figure 6.4: Power spectrum of the velocity of the bright points.

(personal communication) reports a similar negative result of no correlation between the brightness and average speed of a larger number of bright points from the same data set which included both dynamic as well as static points. Thus, the scenario for heating the flux tubes by transverse shaking of the flux-tubes does not seem to be operating at the height where G-band is formed. This leaves the question of what brightens the bright points, for which we might have to fall back on the earlier ideas of wave heating by short period longitudinal waves, generated and launched in the deeper portions of the tubes situated in the convection zone.

Other results that are obtained from this data include the existence of several periods of velocity and brightness fluctuation. Although we have already established the lack of correlation between velocity amplitude and average brightness, we do see the existence of similar periods in the power spectra of brightness and velocity fluctuations. What could be interesting is the presence of a ~ 200 s period that is slightly longer than the 180 s fluctuations of the CaII K bright points in the cell interior. We also see longer periods that are not seen generally in the CaII K cell interior bright points. Another interesting result is a fairly good correlation between the average speed and rms speed seen in Fig (6.3). A distribution of magnetic fields of the flux-tubes, with weaker tubes being more mobile and more susceptible to buffeting, could be a simple explanation for this result. This can be confirmed only with simultaneous magnetic field measurements.

In conclusion, although we find no direct evidence to link the transverse shaking of the flux-tubes to the onset of wave heating of the atmosphere confined by the tube, we do see indications of oscillatory behavior that are possibly related to the dynamical evolution of the chromospheric CaII K bright points.

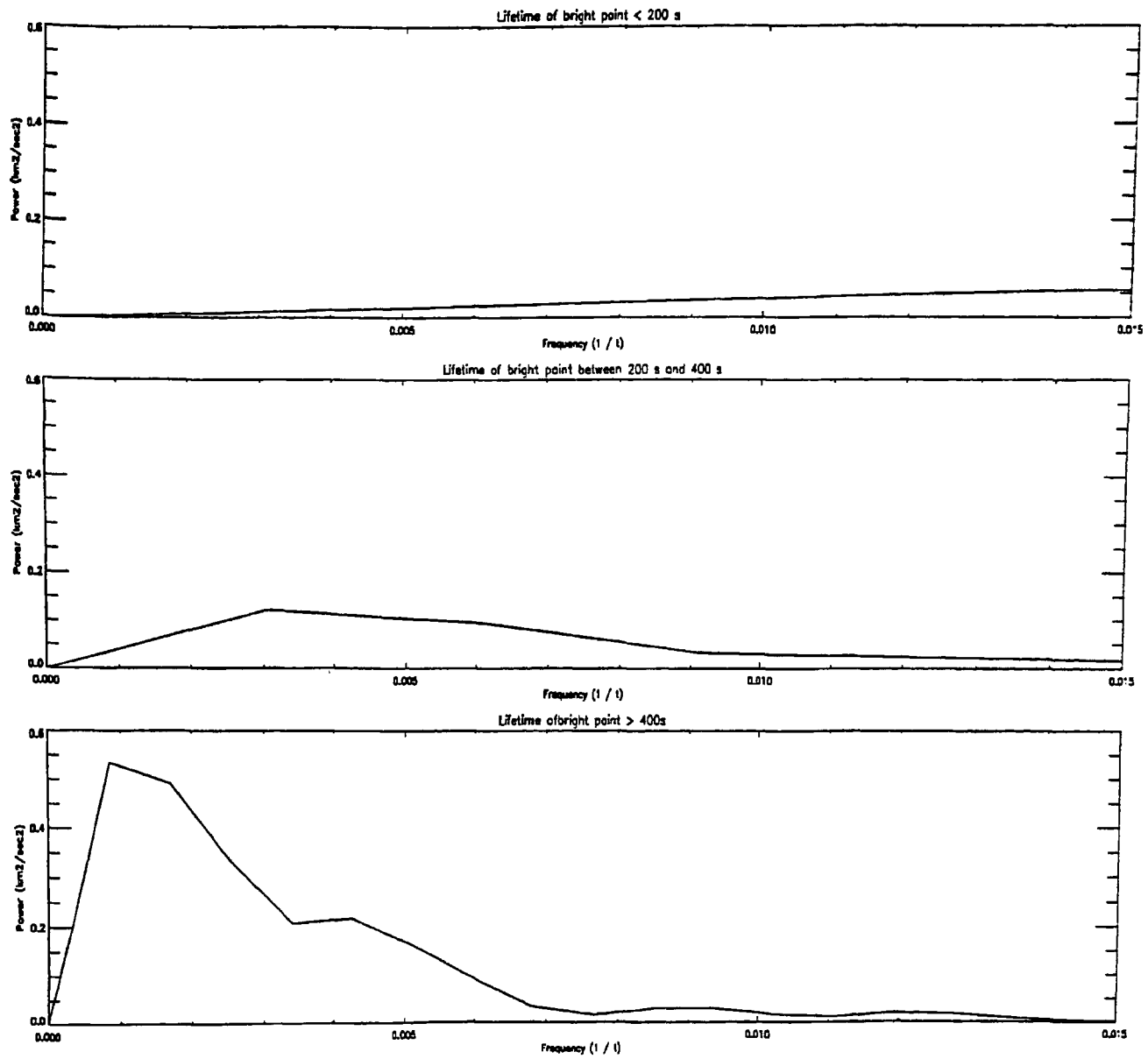


Figure 6.5: Power spectrum of the relative intensity of the bright points.

Table 6.1: Bright points with lifetimes less than 200 s

avg. intensity	rms. intensity	avg. velocity (km/sec)	rms. velocity (km/sec)
0.213	0.095	0.794	1.123
0.271	0.101	1.191	1.191
0.306	0.170	1.191	1.191
0.255	0.091	0.681	1.077
0.275	0.059	2.644	3.532
0.185	0.086	0.000	0.000
0.296	0.101	0.000	0.000
0.195	0.098	0.000	0.000
0.165	0.179	0.000	0.000

Table 6.2: Bright points with lifetimes between 200 s and 400 s

avg. intensity	rms. intensity	avg. velocity (km/sec)	rms. velocity (km/sec)
0.115	0.119	1.589	1.123
0.334	0.138	0.894	1.154
0.233	0.131	1.698	1.672
0.200	0.107	0.000	0.000
0.270	0.082	1.262	1.421
0.394	0.111	1.356	1.395
0.249	0.075	4.745	3.209
0.265	0.077	3.558	3.456
0.260	0.076	4.495	3.321
0.233	0.111	1.176	1.294
0.316	0.071	1.021	1.179
0.238	0.064	1.165	2.677
0.265	0.071	0.794	1.486
0.367	0.152	0.530	0.991
0.249	0.075	1.021	1.179
0.334	0.104	0.596	1.032
0.288	0.104	0.922	1.259

Table 6.3: Bright points with lifetimes greater than 400 s

avg. intensity	rms.intensity	avg. velocity (km/sec)	rms. velocity (km/sec)
0.109	0.113	1.875	1.304
0.250	0.104	1.820	1.371
0.177	0.067	1.096	2.087
0.130	0.067	1.359	2.051
0.266	0.160	1.576	1.363
0.351	0.102	0.935	1.222
0.271	0.175	0.586	1.098
0.103	0.075	1.170	1.332
0.045	0.060	1.579	1.504

Table 6.4: Estimated time periods from Intensity power spectrum

Bright points $b_{200,400}$

Intensity power spectrum (period in seconds)	Velocity power spectrum (period in seconds)
286.0	143.0
—	56.0

Table 6.5: Estimated time periods from Velocity power spectrum

Bright points b_{400}

Intensity power spectrum (period in seconds)	Velocity power spectrum (period in seconds)
1000.0	500.0
222.0	200.0
111.0	118.0
83.0	83.0

Chapter 7

Summary & Conclusions

The following points have emerged as a result of the work done in this thesis:

1) We developed a technique for estimating r_o in images of extended sources. The number of non positive pixels are used as an estimator of the true r_o . We have shown that it is possible to estimate the true r_o even if the signal to noise ratio in the image is as low as 5. The superiority of this technique lies in the fact that unlike other techniques this parameter search method does not need a point sources for the r_o estimation. This technique was extensively tested on simulations and finally on real images. The estimation of r_o is a step towards image restoration.

2) We modeled the noise power spectrum to estimate the Wiener parameter and used this Wiener parameter as an input for the Wiener filter. We applied this filter on real images and recovered high spatial frequency information. It is possible to recover those high frequencies which are recorded at a signal to noise ratio of 30.

3) Using a time sequence a high resolution images of sun, we study the dynamics of the magnetic bright points on the sun. From these power spectrum we find no direct evidence for any relationship to link the transverse shaking of the flux tubes to the onset of wave heating. In other words, the flux brightness seems to be independent of the transverse velocity amplitude. For example, there are bright points which show large variations in their relative velocities but are stationary within the observed spatial scales. However, we do see indications of oscillatory behaviour. Such insights

into the possible connections between fluctuations in the intensity of the bright points and their transverse motions would not have been obtained with inferior seeing.

Small scale magnetic fields of spatial scales less than an arcsecond or less seem to be the main constituent of the solar surface magnetic field. When the fields are measured at low resolution, the integrated field is less. When observed at high resolution, the magnetic fields are seen to be localized and is of the order of few thousand gauss. They are suspected to act as conduits for transport of energy and material from the lower to upper atmosphere. High resolution imaging has opened this new window for looking at these small scale features.

To study the dynamics of these features we need sub-arcsecond resolution. The data we used in this thesis to study the bright points have been obtained at the Swedish Vacuum Solar Telescope, LaPalma in Spain. The resolution in these images is 0."2 arcsecond. It is not practically possible to find observational sites at all longitudes with such good meteorological conditions like on the Canary islands.

Let us assume for a moment that the SVST images presented in this thesis were to be observed at Kodaikanal solar observatory. The average Fried's parameter at this site is 10.0 cm. Let us assume we record the image using a CCD camera which is a 16 bit CCD camera with a full well capacity equal to 64000 counts. Even if we assume that the entire counts contribute for the high frequency component, the photon noise contribution will be roughly 252. Assuming that photon noise is the only source of noise contribution, the signal to noise ratio will be 252. The seeing in Kodaikanal Solar Observatory is on an average 2 arcsecond. From Fig (4.16) in chapter 4 we know that at 2 arcsecond seeing the high frequency component (at ≈ 6 times the seeing limit) will be attenuated by a factor of 1000. This implies that the counts recorded for the high spatial frequency we are interested in will be 64, and the signal to noise ratio will be only 8. We have shown in this thesis that, using a noise modeled Wiener parameter as an input for the Wiener filter we can recover high spatial frequency information upto a signal to noise ratio of 30 at that frequency. If we need a signal to noise ratio of 30 we need atleast 900 counts recorded to recover the high spatial frequency component. The hypothetical observations with

recorded 2 arcsecond seeing would therefore seem grossly inadequate to recover the high spatial frequency information using both linear and non-linear image restoration techniques. However, there are host of other features which have higher flux levels and can be observed and studied at these sites even though the average seeing is one or two arcsecond. Careful restoration of such seeing degraded images allow us to push the angular resolution beyond the seeing limit. In the previous example, a S/N of 30 requires 900 counts for the contrast. Comparing this with a low frequency background of 64000 counts, we can tolerate an attenuation of $64000/900 \approx 70$. Referring to Fig (4.16), this implies successful restoration upto $2.4 f_s$, where f_s is the seeing limit. Such restorations will be extremely useful, if these can be achieved in a routine manner. There exists a hierarchy of magnetic structures like sunspots, pores, filigree and magnetic knots. Study of the time evolution of these features continue to provide useful data on solar activity and related phenomena. Techniques such as image selection will also be useful to capture the images during times of best seeing. Alan Title said (IAU Symposium 138), *'The Sun is a very complicated structure - it has turbulent convection, a whole family of wave motions, magnetic structures etc. It is very easy to fall into the trap looking only at those aspects that you can model simplifiedly'* and this is a point to be taken seriously both by theoreticians and observers alike. We need high resolution data to have better modeling of the solar structures and we need new ways of analysing the data.

References

- Berger, T.E., Schrijver, C.J., Shine, R.S., Tarbell, T.D., Title, A.M., and Schrammer, G. 1995a, *ApJ*, 454,531
- Berger, T.E., Lofdahl, M.G., Shine, R.A., and Title, A.M., 1997, *ApJ*, submitted
- Berger, T.E., and Title, A.M. 1996, *ApJ*, 463,365
- Bouricius, G.M.B., Clifford, S.F., 1970, *J. Opt. Soc. Am.* 60, 1484
- Bray, R.J., and Loughhead, R.E., 1974, *Solar Chromosphere*, Chapman and Hall. London.
- Buser, R.G., 1971, *J. Opt. Soc. Am.* 61, 488
- Chapman, G.A and Sheeley, N.R., Jr. 1968, *Sol.Phys.*,5,443
- Clifford, S.F., Bouricius, G.M.B., Ochs, G.R., Ackley, M.H., 1971, *J. Opt. Soc. Am.* 61, 1279
- Clifford, S.F., Ochs, G.R., Lawrence, R.S., 1974, *J. Opt. Soc. Am.* 64, 148.
- Craig D. Mackay., 1986, *Ann. Rev. Astron. Astrophys.* 24, 255-283
- Collados, M., Vasquez, M., 1987, *Astron. Astrophys.* 180, 223-228.
- Dunn, R.B., and Zirker, J.B., 1973, *Sol.Phys.*, 33,281.
- Frazier, E.N., & Stenflo, J. O. 1972, *Sol.Phys.*, 27, 330
- Fried, D.L., 1966, *J. Opt. Soc. Am.* 56, 1372.
- Giovanelli, R. G., 1980, *Sol.Phys.*, 68, 49.
- Goldman, S. 1953, *Information Theory*. (Dover, New York).
- Gonsalves, R.A. and Chidlaw, R., 1979, in *Applications of Digital Image Processing III*, ed. A.G.Tescher, 32, *Proceedings of the SPIE*
- Goodman, J.W., 1985, *Statistical Optics*. (McGraw Hill, New York).
- Harvey, J. W., & Hall. D. N. B. 1975, *BAAS*, 7, 459

- Howard, R., & Stenflo, J. O. 1972, *Sol.Phys.*, 22, 402
- Hunt, B.R., 1973, *IEEE Trans. Comput C-22*, 805-812
- Keller, C. 1992, *Nature*, 359, 307 Krishnakumar, V., Venkatakrisnan, P., 1997, *Astron. Astrophys*,126,177-181.
- Krishnakumar, V., Venkatakrisnan, P., 1998, *Sol. Phys* (accepted)
- Krishnakumar, V., Venkatakrisnan, P., *ASP. Conf. Ser. Ed. Donahue & Bookbinder, (SanFrancisco) 1998.*
- Krishnakumar, V., Venkatakrisnan, P., *ASP. Conf. Ser. Ed. Jay A.Bookbinder, Edward F. DeLuca & Leon Golub, (SanFrancisco) 1998.*
- Lofdahl, M.G.,Berger, T.E.,Shine, R.A., and Title, A.M. 1997, *ApJ*,submitted
- Lofdahl, M.G.,Berger, T.E.,Shine, R.A.,Title, A.M.,1997, *ApJ*,submitted
- Mehltretter, J.P. 1974, *Sol. Phys.*, 38, 43
- Michael C. Roggemann, Byron M. Welsh & Robert Q. Fugate. 1997, *Rev. of Mod. phys.*. 69,437
- Muller, R., 1985, *Sol. Phys.*, 100, 237
- Muller, R., and Keil, B. 1983, *Sol. Phys.*, 87, 243
- Muller, R. 1975, *Sol.Phys.*, 45, 105
- Muller, R., & Roddier, T. 1984, *Sol.Phys.*, 94, 33
- Michael. V. Newberry. Summer 1994, *CCD Astronomy.*, 34
- Michael. V. Newberry. Fall 1994, *CCD Astronomy.*, 12
- Peter. Foukal. 1989, *Solar Astrophysics*, John Wiley & Sons Inc.
- Peter A. Jansson., *Traditional Linear Deconvolution Methods* . In: Peter A.Jansson. (ed) *Deconvolution of Images and Spectra*, 1997, p. 77
- Peter B. Stetson., 1987, *PASP*, 99, 191.
- Rabin, D. 1992, *ApJ* , 390, L103
- Ryotova, M. P., Kaisig, M., Tajima, T. 1996, *ApJ*, 459, 744
- Roddier., *The Effects of Atmospheric Turbulence in Optical Astronomy*. In: Wolf E.(ed) *Progress in Optics*, p.281
- Tatarski, V.I., 1961, *Wave Propogation in Turbulent Medium*. (McGraw Hill Book Co.. New York).

- Sheeley, N.R. 1969, Sol.Phys., 9, 347
- Simon, G.W., & Zirker, J.B. 1974, Sol.Phys., 35, 331
- Solanki, S. K. 1993, Space Sci Rev., 63, 1
- Spruit, H. C. 1976, Sol.Phys., 50, 269
- Spruit, H. C., & Zweibel, E. G. 1979, Sol.Phys., 62, 15
- Stenflo, J.O., and Harvey, J.W. 1985, Sol. Phys., 95,99
- Stenflo, J.O. 1982, Sol. Phys., 80, 209
- Stenflo, J. O. 1973, Sol.Phys., 32, 41
- Stuart. M. Jefferies, & Julian C .Christou. 1993, Bull. American. Astron. Soc., 181. 1308
- Title, A.M., Tarbell, T.D., and Topka, K.P. 1987, ApJ,317,892
- Tarbell, T. D., & Title, A. M. 1977, Sol.Phys., 52, 13
- Ulmschneider, P.,Zahringer, K., & Musielak, Z.E., 1991, A&A 241, 625
- Van Ballegooijen, A.,Nisenson, P.,Noyes, R.W., Stein, R.F., Nordlund, A., Krishnakumar, V. 1998 (submitted ApJ)
- Venkatakrishnan P., 1984, Kodaikanal Obs. Bulletin 4, 19-24
- Weiss, 1984, Theoretical Interpretation of Small Scale Features, Proceedings of High Resolution in Solar Physics, Toulouse, France., ed.,Muller, Springer Verlag
- Yi, Z., and Engvold, O., 1993,Sol.Phys., 144,1
- Zayer, I., Solanki, S. K., & Stenflo,J.O. 1989, A&A, 211, 463
- Zwaan. 1965 Ph.D., Thesis